

# Study of the orbital exciton in $\text{LaMnO}_3$

Dissertation  
zur Erlangung des Doktorgrades  
des Department Physik  
der Universität Hamburg

vorgelegt von  
Rilana Maeser  
(geb. Krüger)  
aus Bremen

Hamburg 2018

|   |   |
|---|---|
| Gutachter der Dissertation:   | Prof. Dr. Michael A. Rübhausen<br>Prof. Dr. Arwen Pearson |
| Gutachter der Disputation:  | Prof. Dr. Michael A. Rübhausen<br>Prof. Dr. Nils Huse     |
| Datum der Disputation:  | 23.11.2018  |
| Vorsitzende des<br>Prüfungsausschusses:                                   | Prof. Dr. Daniela Pfannkuche                              |
| Vorsitzender des Promotionsausschusses:                                   | Prof. Dr. Michael Potthoff                                |
| Dekan der Fakultät für Mathematik,<br>Informatik und Naturwissenschaften: | Prof. Dr. Heinrich Graener                                |

## Inhaltsangabe

In dieser Arbeit werden die optischen Eigenschaften von  $\text{LaMnO}_3$  untersucht.  $\text{LaMnO}_3$  gehört zur Klasse der stark korrelierten Übergangsmetall-oxide - berühmt für ihre reichen Phasendiagramme und das noch nicht komplett verstandene Zusammenspiel zwischen ihren elektronischen, magnetischen und strukturellen Freiheitsgraden.  $\text{LaMnO}_3$  ist eine Ausgangsverbindung, die über Dotierung Effekte wie den kolossalen Magnetowiderstand (CMR) aufweisen kann. Das Verständnis von Mechanismen im undotierten Material beeinflusst ebenfalls das Verständnis der Mechanismen, die in den interessanten Phasen zum Tragen kommen. Der Einfluss der Elektron-Phonon-Kopplung auf den CMR-Effekt ist erwiesen und ebenso Gegenstand dieser Studie. Die Elektron-Phonon-Kopplung steht zur Diskussion als ein Mechanismus, der zur orbitalen Ordnung in  $\text{LaMnO}_3$  führen kann. Im Rahmen dieser Arbeit wurde eine Resonanz-Raman-Streuungsuntersuchung an einem orbital geordneten  $\text{LaMnO}_3$  Einkristall bei Raumtemperatur und mit 12 Anregungsenergien zwischen 1.8 eV (nahes IR) und 5.0 eV (tiefes UV) durchgeführt. Komplementiert wurde diese Untersuchung mit Messungen der spektroskopischen Ellipsometrie. Ein neues Raman-Spektrometer (McPherson), ausgestattet mit einem UV-sensitiven CCD-Chip und reflektierenden Objektiven (Cassegrain design), wurde zur Durchführung der Studie mittels inelastischer Lichtstreuung eingesetzt. Dieses gab uns die Möglichkeit, die Anregungsenergien sowie den untersuchten Bereich der Raman-Streuung in den UV-Bereich auszudehnen - im Gegensatz zu den herkömmlicherweise im sichtbaren Spektralbereich durchgeführten Messungen. Die Resonanzprofile geben Aufschluss über die im Raman-Prozess wichtigsten exzitonischen Zustände in  $\text{LaMnO}_3$ . Erhöhte Multiphonon-Streuung bekräftigt die Theorie, dass die orbitale Ordnung hauptsächlich durch den Jahn-Teller-Effekt beeinflusst wird. Unterstützt wird diese Einschätzung durch theoretische Berechnungen innerhalb des Franck-Condon-Mechanismus von Vasili Perebeinos und Philip Allen [47], die bemerkenswert gut mit unseren experimentellen Ergebnissen übereinstimmen. Die Orbiton-Energie quantifizieren wir deshalb bei  $\sim 2$  eV. Zusammenfassend konnten wir zeigen, dass die inelastische Lichtstreuung eine effiziente Methode ist, um das Zusammenspiel von elektronischen und strukturellen Freiheitsgraden in  $\text{LaMnO}_3$  zu untersuchen und dadurch auch, um Informationen über die orbitale Ordnung zu erhalten.

## Abstract

Within this thesis the optical properties of  $\text{LaMnO}_3$  are examined.  $\text{LaMnO}_3$  orders into the class of strongly correlated transition metal oxides - famous for their rich phase diagrams and not completely understood interplay of their electronical, magnetical and structural degrees of freedom.  $\text{LaMnO}_3$  is a parent compound that can by doping show effects like the colossal magnetoresistance (CMR). Understanding mechanisms in the undoped material influences the understanding of these interesting phases likewise. The importance of the electron-phonon coupling is evident for the CMR effect and also object of this work as it is in discussion as one leading mechanism via the Jahn-Teller effect that can drive the orbital ordering found in  $\text{LaMnO}_3$ . A resonance Raman scattering study at an orbitally ordered  $\text{LaMnO}_3$  single crystal has been performed with 12 excitation energies between 1.8 eV (near IR) and 5.0 eV (deep UV) at room temperature and complemented by spectroscopic ellipsometry measurements. The inelastic light scattering experiments have been operated on a novel Raman spectrometer (McPherson) equipped with a UV-sensitive charge-coupled device and with a reflecting objective in a Cassegrain design allowing to extend excitation energies and the Raman scattering range into the UV in contrast to the usually performed measurements with visible excitation energies. From the comparison of the resonance profiles we derive the most important excitonic states for the Raman process in  $\text{LaMnO}_3$ . Enhanced multiphonon scattering affirms the assignment of an orbitally ordered state mainly driven by the Jahn-Teller effect, which is complemented by theoretical calculations within the Franck-Condon mechanism by Vasili Perebeinos and Philip Allen [47] that match remarkably well to our experimental results and lead to an orbiton energy assignment of 2 eV. In summary, we have shown the efficiency of inelastic light scattering to study the interplay between electronical and structural degrees of freedom in  $\text{LaMnO}_3$  and this way likewise to receive information about the orbital ordering.

# Contents

|          |   |            |
|----------|---|------------|
| <b>1</b> | <b>An introduction to optical properties of solids</b>  | <b>15</b>  |
| <b>2</b> | <b>Manganites</b>   | <b>21</b>  |
| 2.1      | Strongly correlated electron systems and manganites . . . . .   | 21         |
| 2.2      | Mixed valence manganese oxides and $\text{LaMnO}_3$ . . . . .   | 23         |
| 2.3      | Franck-Condon mechanism . . . . .   | 40         |
| <b>3</b> | <b>Experimental techniques: theory and setup</b>  | <b>45</b>  |
| 3.1      | Theory of ellipsometry . . . . .  | 45         |
| 3.2      | Setup of ellipsometry . . . . .   | 49         |
| 3.3      | Theory of Raman scattering . . . . .  | 49         |
| 3.4      | Theory of resonance Raman scattering . . . . .  | 54         |
| 3.5      | Effective sample volume . . . . .   | 61         |
| 3.6      | Resonance Raman setup (UT-3) . . . . .  | 66         |
| 3.7      | Setup: Orbital-ordered $\text{LaMnO}_3$ . . . . .   | 71         |
|          | <b>Paper I</b> Fully reflective deep ultraviolet to near infrared spectrometer and entrance optics for resonance Raman spectroscopy . . . . . | 74         |
| <b>4</b> | <b>Experimental results and discussion on <math>\text{LaMnO}_3</math></b>   | <b>87</b>  |
| 4.1      | Dielectric function of $\text{LaMnO}_3$ . . . . .   | 87         |
| 4.2      | Raman spectra of $\text{LaMnO}_3$ and phonon mode assignment . . .  | 88         |
| 4.3      | Resonances of $\text{LaMnO}_3$ . . . . .  | 91         |
| 4.4      | Franck-Condon mechanism in $\text{LaMnO}_3$ . . . . .   | 96         |
| 4.5      | Franck-Condon mechanism in $\text{LaMnO}_3$ - model calculations .  | 99         |
|          | <b>Paper II</b> Orbital ordering in $\text{LaMnO}_3$ Investigated by Resonance Raman Spectroscopy . . . . .                                   | 105        |
| <b>5</b> | <b>Summary and outlook</b>  | <b>109</b> |
| <b>6</b> | <b>Acknowledgments</b>  | <b>111</b> |

|   |            |
|---|------------|
| <b>A Error estimation of the solid angle correction</b> | <b>115</b> |
| <b>Bibliography</b>                                     | <b>119</b> |

# List of Figures

|     |   |    |
|-----|---|----|
| 1.1 | A sketch of the frequency dependencies of the real and imaginary part of the complex dielectric function ( $\epsilon_1$ and $\epsilon_2$ ) according to the dipole oscillator model in the vicinity of a sharp atomic absorption line ( $\omega_0$ ) and the calculated functions of the refractive index $n$ and the extinction coefficient $\kappa$ by using $\epsilon_1$ and $\epsilon_2$ and applying equations 1.9 and 1.10 (adapted from [31]) are depicted exemplarily. While $n$ is mainly influenced by $\epsilon_1$ , $\kappa$ essentially follows $\epsilon_2$ , which can be deduced from equations 1.11 and 1.12. Although the assumption of small absorption there is not exact near $\omega_0$ , the typical characteristics can be figured out. The frequency ranges, in which the characteristics shown in the figure can be found, are affected by $\gamma$ and are more extensive for $n$ than for $\kappa$ . The outcome of this is that dispersion in the refractive index as a consequence of the resonance is observed also in frequency ranges with no absorption. Passing through more resonances, the background $n$ (dielectric function respectively) outside the resonances increases each time with decreasing frequency as it is influenced by the wings of the oscillators at higher frequencies. . . . . | 19 |
| 2.1 | Undistorted perovskite unit cell of $\text{LaMnO}_3$ . . . . .  | 24 |
| 2.2 | Mn 3d orbitals in different environments and the corresponding lattice distortion and energetical splitting . . . . .   | 25 |
| 2.3 | Top view of the Mn 3d $e_g$ orbital ordering within the $ab$ plane. JT distortions are indicated by black arrows, while tilting and rotation distortions are omitted in this scheme. . . . .  | 26 |
| 2.4 | Examples of JT distortions of $e_g$ symmetry (purely $Q_2$ or $Q_3$ respectively). The corresponding displacements of the regular oxygen octahedra are illustrated by arrows (adapted from: [24, 49]). . . . .  | 27 |

- 2.5 (Adapted from [24].) Inner circle: different possible orbital states of a Mn 3d  $e_g$  electron and outer circle: corresponding combinations of the JT lattice distortions within the  $Q_2/Q_3$  plane. Both are described by the mixing angle  $\theta$  (see text). . . . . 28
- 2.6 Examples of the superexchange mechanism in general on the basis of two  $\text{Mn}^{3+}$   $d_{3z^2-r^2}$  typ orbitals pointing towards each other and bridged by an O  $2p_z$  orbital (in different surrounding conditions): a) 2 half-filled  $d_{3z^2-r^2}$  typ orbitals antiferromagnetically connected - through a covalent bonding with the oxygen - as the by horizontal arrows indicated virtual electron transfer can take place only in this configuration due to the Pauli exclusion principle. b) Antiferromagnetic order between two empty  $d_{3z^2-r^2}$  typ orbitals c) Half-filled  $d_{3z^2-r^2}$  typ orbital ferromagnetically connected to a manganese ion with an empty  $d_{3z^2-r^2}$  typ orbital. Due to a non-zero probability density function of the spin-up O  $2p_z$  electron at the empty  $d_{3z^2-r^2}$  orbital on the right hand side, it polarizes the  $t_{2g}$  core electrons ferromagnetically because of Hund's rule (adapted from:[43]). . . . . 30
- 2.7 Three-dimensional orbital and spin ordering (black arrows) of the Mn 3d  $e_g$  orbitals (see text). . . . . 31
- 2.8 Tilting and rotation of the oxygen octahedra in  $\text{LaMnO}_3$ . JT distortions are omitted in this scheme (adapted from: [59]). . . . . 32
- 2.9 Top view of the JT distortions and orbital ordering in the  $ab$  plane. The rotations of the oxygen octahedra are indicated as well as the Mn-O-Mn bond angle  $\varphi$  (see text)(adapted from [57]). . . . . 33
- 2.10 (a) Phase diagram of the doped manganite  $\text{La}_{1-x}\text{Ca}_x\text{MnO}_3$  (adapted from: [35]) with  $\text{LaMnO}_3$  position investigated within this thesis emphasized by the light green cross. Depicted are the following phases at lower temperatures: CAF (Canted Antiferromagnetic Insulator), FI (Ferromagnetic Insulator), CO (Charge Ordered Insulator), FM (Ferromagnetic Metal) and AF (Antiferromagnetic Insulator). Not shown is the PI (Paramagnetic Insulator) phase at higher temperatures separated to the FM phase by the CMR region (light gray striped area). The CMR effect (strong change of resistivity around  $T_c$  by applying a magnetic field) at a sample with doping  $x=0.25$  is demonstrated in (b)(adapted from: [54]). . . . . 34

- 2.11 Depicted is the electron hopping process within the double exchange mechanism. Electrical conductivity accounts for a ferromagnetic ordering between the Mn-ions and vice versa within this mechanism as no energy due to Hund's rule coupling has to be invested during the hopping process this way. Mixed valencies (half-filled  $\text{Mn}^{3+}$   $d_{3z^2-r^2}$  orbital connected to an empty  $\text{Mn}^{4+}$   $d_{3z^2-r^2}$  orbital) also promote this mechanism saving coulomb repulsion energy  $U$  (adapted from: [43]). a) Initial state b) After the electron hopping process. . . . . 36
- 2.12 Schematic illustration of a possible orbital wave [52]. Electron orbitals in the undisturbed ordered ground state (upper row). Orbital wave in form of a modulation in the relative shape of the ordered orbitals propagating through the crystal (lower row). . . . . 38
- 2.13 Raman spectra measured by Saitoh and coworkers (black and red) as well as the estimated two-phonon region (blue). Controversially discussed is the origin of the peaks between about  $1000 \text{ cm}^{-1}$  and  $1400 \text{ cm}^{-1}$  (see text) (adapted from: [52]). . . . 39
- 2.14 Schematic of the Franck-Condon mechanism in a diatomic molecule in four steps: a.) Oscillator potentials of the ground and excited state. Depicted are the energy levels of the vibronic states in dependence of the generalized coordinate  $Q$  - in this case the nuclear separation  $r$ . b.) 'Dumb-bell' diagrams of the molecule with its two different equilibrium separations  $Q_0$  and  $Q'_0$  during the Franck-Condon process. The radius of one atom is increased in the excited state (adapted from: [31]). 40

- 3.1 (a) Depicted is a simplified spectroscopic ellipsometry setup consisting of a light source, a polarizer producing linearly polarized light before the sample is irradiated under an angle  $\phi_0$  with the surface normal ( $\mathbf{n}$ ), an analyzer and a detector measuring the intensity of the directly reflected light in dependence of the analyzer angle. Spectroscopic ellipsometry determines the parameters  $\Psi$  and  $\Delta$  in a specific spectral range in dependence of the wavelength of the incident light. For simplification the polarization states of the electrical field  $\mathbf{E}$  are decomposed into 'p-polarized' (parallel to the plane of incidence (POI), which is defined by the directions of the incident and reflected light) and 's-polarized' (perpendicular to the POI). The indices  $i$  and  $r$  refer to the incoming and reflected light. (b) and (c) depict an example (identical absolute value of the electrical field components) of the polarization states of the incoming (linearly polarized) and reflected (elliptically polarized) light, with  $\Delta = \delta_p - \delta_s$ , being the phase shift difference of the s and p component of the electrical field,  $\tan \Psi = \frac{|r_p|}{|r_s|}$ , which refers to the relative change of amplitude of the two components upon reflection, and  $P$  indicating the resulting polarization direction (adapted from [64]). . . . . 46
- 3.2 To illustrate the mutual exclusion of Raman and infrared active modes in a molecule with inversion center a symmetrical stretching mode (upper row) and an asymmetrical stretching mode (lower row) together with their corresponding developments of the polarizability  $\alpha$  and the dipole moment  $p$  with the normal coordinate  $Q$  are shown exemplarily. . . . . 51
- 3.3 First-order Raman scattering is classified into a simple phonon dispersion curve near the Brillouin zone center ( $\Gamma$ -point) (red cross). This excited optical phonon can decay into two acoustic phonons (blue arrows). Green circles illustrate a favored combination for a two-phonon Raman scattering process. . . . 53

- 3.4 Raman scattering process based on a four-photon Green's function as derived by Kawabata [21, 22], visualized with the help of Feynman diagrams. A more detailed description of the one-phonon Raman process (upper diagram) and the two-phonon Raman process (lower diagram) is found in the text below. Additionally, in the upper Feynman diagram symbolic anti-Stokes (blue shifted) and symbolic Stokes (red shifted) processes are shown by the dashed blue and red lines respectively. The photon-electron interaction vertices (blue squares) indicate the  $I \propto \omega^4$  proportionality of the Raman scattering intensity resulting from the dipole approximation. . . . . 56
- 3.5 a.) Second-order phonon spectra of silicon measured by Manuel Cardona and his group [48] in dependence of the excitation laser wavelengths. b.) and c.) show the resonance profiles of the first- and second-order phonon modes of silicon respectively. The Raman cross section is depicted in dependence of the laser excitation energy in electron volts (eV). . . . . 60
- 3.6 Possible paths of the incident and detectable Raman scattered light lying within the cones depicted with solid lines. The cone inside the sample is defined by the limiting collecting angle  $\theta_{obj}$  of the mirror M1 and the complex refractive index  $\tilde{n}'$  of the sample. The interruptions of the solid lines outside the sample by dotted lines indicate a break in the order of magnitude of this depiction in respective area. . . . . 62
- 3.7 Depicted is the transmitted complex wavevector  $\vec{k}'$  from a non absorbing medium with refractive index  $n$  to a medium with a complex refractive index  $\tilde{n}'$ . The boundary surface is the  $xy$  plane and  $\theta$  the angle of incidence (not depicted here). . . . 63
- 3.8 Scheme of the resonance Raman setup: An argon and a krypton laser produce monochromatic light, which is guided through a premonochromator (to exclude plasma lines of the laser), a scrambler and polarizer (to select a polarization direction of the light) and a spatial filter (to eliminate inhomogeneities of the laser beam) into the fully achromatic entrance optics. A parabolic mirror focuses the light onto the sample. The Raman scattered light is collected by the entrance optics and directed through an analyzer (to select a specific polarization direction of the Raman signal) into the Raman spectrometer (monochromators No. 1, No. 2, No. 3 and a relay stage) and finally onto a nitrogen cooled CCD camera. . . . . 66

- 3.9 (a) Top view of a scheme of the achromatic entrance optics consisting of four on-axis parabolic mirrors (M1, M2, M3, M4). The beam path is shown in 7 steps. Step 1: Enlarged laser light is guided onto M1 (dotted lines). Step 2: M1 focuses the laser light onto the sample. Step 3 and 4: The scattered Raman signal is collected and collimated onto M2 by M1. Step 5: The light is focused into a hole of an inserted analyzer - not influenced by the analyzer so far - and collected by M3. Step 6: M3 collimates the light, which is afterwards directed through the analyzer. Not depicted is the conically drilled hole of the analyzer ensuring that almost all light is polarized. Step 7: M4 focuses the light into the UT-3 Raman spectrometer. (b) Top view of the entrance optics. M2 and M1 (each with a diameter of 250 mm) are visible. (c) Image of the Raman setup. 69
- 3.10 Ray tracings of the UT-3 Raman spectrometer (premonochromator and monochromator No. 3) and the entrance optics. The UT-3 is an all reflecting and this way achromatic Raman spectrometer with three high dispersive gratings. Off-axis parabolic mirrors in the premonochromator, consisting of subtractively coupled monochromator No. 1 and monochromator No. 2 and a relay stage, minimize image aberrations. Slit 1 and slit 2 form the band pass. Within the premonochromator an excellent stray light rejection can be realized and in combination with monochromator No. 3, the spectrograph stage, which spectrally resolves the light and focuses the Raman signal onto a nitrogen cooled CCD camera, high resolution is achieved. This allows for Raman measurements over a broad wavelength range (165 nm - 1000 nm). . . . . 70
- 3.11 (a)  $\text{LaMnO}_3$  mounted on sand blasted silicon onto the sample holder and (b)  $\text{LaMnO}_3$  zoomed up. (c) Image of the sample surface in the plane of the entrance slits of the UT-3 (slit dimensions: 2 mm (width)/ 1.7 mm (height)) visualized by a periscope. The laser spot (marked) was placed onto the same position of the sample for all excitation wavelengths. . . . . 71
- 4.1 Dielectric function of  $\text{LaMnO}_3$  measured with spectral ellipsometry. Colored vertical lines indicate the Raman excitation wavelengths we have applied for the resonance Raman scattering study. . . . . 88

|     |  |     |
|-----|--|-----|
| 4.2 | LaMnO <sub>3</sub> Raman spectrum measured at 302 nm excitation wavelength and room temperature. Second- and third-order Raman modes are zoomed up for clarity and different mixing combinations of the one-phonon modes are indicated by red (associated with the 76 meV mode), blue (associated with the 62 meV mode) and green (associated with the 81 meV mode) arrows. . . . .  | 89  |
| 4.3 | Phonons of different symmetry found in LaMnO <sub>3</sub> : A <sub>g</sub> (1) in-phase stretching phonon mode (adapted from: [15]) associated with the Q <sub>2</sub> -distortion and B <sub>2g</sub> (1) in-phase stretching phonon mode (adapted from: [15]) associated with the Q <sub>3</sub> -distortion. Arrows indicate the oscillations of the oxygen atoms of the octahedra. . . . .   | 90  |
| 4.4 | LaMnO <sub>3</sub> Raman spectra in dependence of the incident photon energy (depicted by different colors): (a) First-order phonon modes. (b) Second-order phonon modes (zoomed up 10 times). . . . .   | 91  |
| 4.5 | One- and two-phonon excitation profiles (integrated intensities over the laser excitation energy) of the combined 611 cm <sup>-1</sup> and 655 cm <sup>-1</sup> first-order phonon modes (green squares) and the peak at 1300 cm <sup>-1</sup> in the two-phonon region (red circles). The black curve depicts the excitation profile of the two-phonon region multiplied by a factor of 4.166. The nearly constant relation between the two- and one-phonon intensities in dependence of the excitation energy is shown in the inset. . . . . | 92  |
| 4.6 | One-phonon excitation profiles displaying the magnitude of coupling of the 496 cm <sup>-1</sup> , 611 cm <sup>-1</sup> and the 655 cm <sup>-1</sup> mode to the specific excitonic states of LaMnO <sub>3</sub> (2.05 eV and ~ 4 eV). . . . .  | 95  |
| 4.7 | Flip of the LaMnO <sub>3</sub> 3d orbital from the orbitally ordered and JT distorted ground state, excited with the orbiton energy of 2Δ. This process is followed by a lattice relaxation later. . . . .   | 96  |
| 4.8 | Shifted oscillator potentials allow for enhanced one- and multiphonon excitations within the Franck-Condon mechanism with an excitation energy of 2Δ. An orbital flip (orbiton excitation) is depicted in the lower row (adapted from [47]). . . . .   | 97  |
| 4.9 | Comparison of the within the FC mechanism calculated (black curves) and experimentally (squares (611 cm <sup>-1</sup> ) and circles (1300 cm <sup>-1</sup> )) obtained one-phonon and two-phonon resonances (resonance profiles). . . . .  | 101 |

- A.1 a) shows a spherical cap with  $a$  the radius of its base and  $h$  the height of the cap and  $r$  the radius of the sphere. A cross section of a spherical cap is depicted in b). In case of no absorption and  $n = n' = 1$  (same refractive index inside and outside of the sample), the cone in b) represents the solid angle (depicted in cross section) inside and outside the sample similarly (though  $\theta$  is named  $\theta_{sam}$  inside the sample). In opposition to this representation, the corresponding mirror M1 in the UT-3 experiment is parabolic. As it does not influence the calculations above, it is not graphically shown here. . . . 116

# Chapter 1

## An introduction to optical properties of solids

Optical research techniques can not only in a literal sense shed light on a material. Within this thesis two of them have been used: Raman scattering supplemented with spectroscopic ellipsometry. Therefore, in this section a short introduction of the optical properties of solids shall be given [31]. Light can interact with matter in various ways: it can be reflected at the interface of materials with different refractive indices (cf. section 3.1), transmitted through and absorbed inside a material. Which fractions of an incident light beam underlie these processes is depending on the optical properties of the involved materials. Absorption can result in luminescence or be followed by radiationless transitions channeling the excitation energy into heat. In both ways the intensity of the original beam is diminished. A further process - the scattering - also attenuates the beam as it alters its direction in case of elastic scattering and in addition to this the frequency in case of inelastic scattering (cf. section 3.3). Light that enters a solid with different optical properties than its surrounding and that is not absorbed will be refracted during its transmission. The refraction ( $n$ ) is determined by the velocity of light in a solid ( $v$ ). If the frequency of the entering light ( $\omega$ ) differs from a resonant frequency ( $\omega_0$ ) of an oscillator within the solid, forced oscillations at  $\omega$  are excited. Forced oscillations imply a phase lag caused by damping. The phase lag accumulates through the solid (with each elastic and coherent scattering process) resulting in a retardation of the propagation of the wave front. The ratio of the velocity of light in free space ( $c$ ) to the reduced velocity in the solid ( $v$ ) defines the refraction ( $n$ ):

$$n = \frac{c}{v}. \quad (1.1)$$

Maxwell's equations for a medium with no free charges or currents can be assigned to the wave equation leading to the following equation for the phase velocity of an electromagnetic wave in the medium [31]:

$$v = \frac{c}{\sqrt{\epsilon_r \mu_r}}. \quad (1.2)$$

With the relative magnetic permeability  $\mu_r = 1$  at optical frequencies, equation 1.1 and equation 1.2 can be combined to:

$$n = \sqrt{\epsilon_r} \quad (1.3)$$

giving a relationship between the refractive index  $n$  and the relative dielectric function  $\epsilon_r$ . In the more general case, absorption has to be taken into account and equation 1.3 has to be considered as complex:

$$N^2 = \epsilon_r, \quad (1.4)$$

with

$$\epsilon_r = \epsilon_1 + i\epsilon_2, \quad (1.5)$$

the complex relative dielectric function and

$$N = n + i\kappa, \quad (1.6)$$

the complex refractive index, with  $\kappa$  the extinction coefficient characterizing the absorption. Deduced from one complex parameter, the imaginary part  $\kappa$  and the real part  $n$  are not independent of each other ( $n$  and  $\kappa$  can be connected by the Kramers-Kronig relationships) as well as  $N$  is not independent of  $\epsilon_r$ . The following relations can be achieved by combining equations 1.4, 1.5 and 1.6:

$$\epsilon_1 = n^2 - \kappa^2 \quad (1.7)$$

$$\epsilon_2 = 2n\kappa \quad (1.8)$$

$$n = \frac{1}{\sqrt{2}}(\epsilon_1 + (\epsilon_1^2 + \epsilon_2^2)^{\frac{1}{2}})^{\frac{1}{2}} \quad (1.9)$$

$$\kappa = \frac{1}{\sqrt{2}}(-\epsilon_1 + (\epsilon_1^2 + \epsilon_2^2)^{\frac{1}{2}})^{\frac{1}{2}}. \quad (1.10)$$

For very small absorption (very small  $\kappa$ ) these equations can be simplified to:

$$n = \sqrt{\epsilon_1} \quad (1.11)$$

$$\kappa = \frac{\epsilon_2}{2n}. \quad (1.12)$$

$\epsilon_r$  depends on the polarizability of the solid and describes as well as  $N$  the optical properties of a solid. The development of the complex dielectric function with frequency can be quantified by the Lorentz dipole oscillator model. Treating the possible specific excitations of a solid as oscillating electric dipoles and light as electromagnetic wave, this classical model leads to [31]:

$$\epsilon_1(\omega) = 1 + \chi + \frac{Ne^2}{\epsilon_0 m_0} \frac{\omega_0^2 - \omega^2}{(\omega_0^2 - \omega^2)^2 + (\gamma\omega)^2} \quad (1.13)$$

$$\epsilon_2(\omega) = \frac{Ne^2}{\epsilon_0 m_0} \frac{\gamma\omega}{(\omega_0^2 - \omega^2)^2 + (\gamma\omega)^2} \quad (1.14)$$

for an isotropic material with a single resonant frequency  $\omega_0$  and with  $N$ , the number of atoms per unit volume,  $\epsilon_0$ , the electric permittivity of free space,  $m_0$ , the mass of the electron,  $e$ , the magnitude of the electric charge of the electron and  $\gamma$ , the damping rate. In the ansatz to derive the formulae 1.13 and 1.14 an electric susceptibility  $\chi$  accounting for all other (non-resonant) contributions to the polarizability of the atoms was applied [31]. Concentrating on frequencies close to resonance ( $\omega \approx \omega_0 \gg \gamma$ ), the high frequency limit  $\epsilon_r(\infty) \equiv \epsilon_\infty$  results in  $\epsilon_\infty = 1 + \chi$  and describes a real number in equation 1.13. Likewise, equations 1.13 and 1.14 simplify more [31], leading to a

frequency dependent development of  $\epsilon_1$  and  $\epsilon_2$ , schematically shown in figure 1.1 (adapted from [31]). Typical resonant frequencies of a solid are found e.g. in the infrared region ( $10^{12} - 10^{13}$  Hz) due to vibrations of the atoms and in the infrared, visible and ultraviolet region ( $10^{14} - 10^{15}$  Hz) caused by bound electrons. By superposing specific resonance characteristics, the dipole oscillator model can take account of different contributions to the dielectric function. In contrast to the description above for an isotropic material, real solids often show more complicated symmetries resulting in varying optical properties along different crystal orientations. This optical anisotropy allows to gain knowledge about the crystal structure via the dielectric constant tensor.

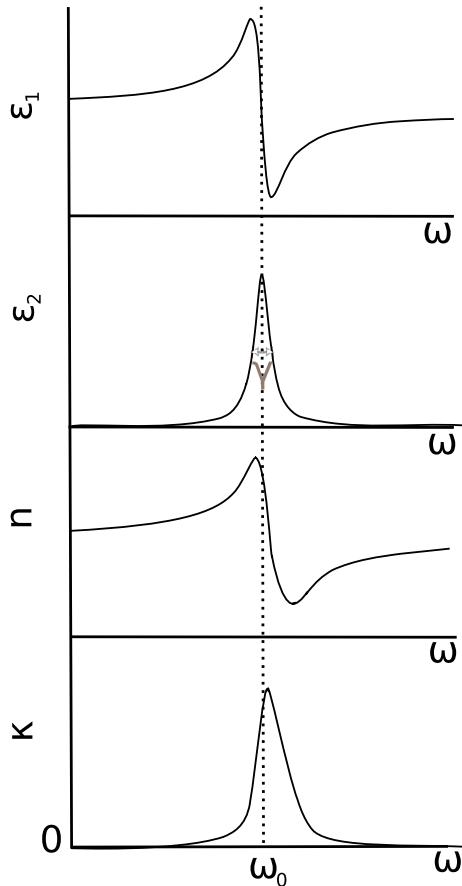


**Figure 1.1:** A sketch of the frequency dependencies of the real and imaginary part of the complex dielectric function ( $\epsilon_1$  and  $\epsilon_2$ ) according to the dipole oscillator model in the vicinity of a sharp atomic absorption line ( $\omega_0$ ) and the calculated functions of the refractive index  $n$  and the extinction coefficient  $\kappa$  by using  $\epsilon_1$  and  $\epsilon_2$  and applying equations 1.9 and 1.10 (adapted from [31]) are depicted exemplarily. While  $n$  is mainly influenced by  $\epsilon_1$ ,  $\kappa$  essentially follows  $\epsilon_2$ , which can be deduced from equations 1.11 and 1.12. Although the assumption of small absorption there is not exact near  $\omega_0$ , the typical characteristics can be figured out. The frequency ranges, in which the characteristics shown in the figure can be found, are affected by  $\gamma$  and are more extensive for  $n$  than for  $\kappa$ . The outcome of this is that dispersion in the refractive index as a consequence of the resonance is observed also in frequency ranges with no absorption. Passing through more resonances, the background  $n$  (dielectric function respectively) outside the resonances increases each time with decreasing frequency as it is influenced by the wings of the oscillators at higher frequencies.



# Chapter 2

## Manganites

### 2.1 Strongly correlated electron systems and manganites

The investigated  $\text{LaMnO}_3$  sample is classified into the field of strongly correlated electron systems based on transition metal compounds, in which the partially filled 3/4/5d levels play a crucial role in the variety of the electronic structures they exhibit. High- $T_c$  superconductivity, spintronics, multiferroicity and magnetoelectricity e.g. can be traced back to the physics of these compounds [24]. One subgroup - the manganites - became famous for their magnetoresistivity effect (MR) [6, 33]. Already in 1950 the interplay between magnetism and conductivity in the manganites was observed [18, 62]. An increase in the conductivity could be reached by lowering the temperature into the magnetically ordered phase. An even by orders of magnitude higher effect of magnetoresistance - the so called colossal magneto resistance (CMR) - was discovered at the beginning of the 1990s in manganite thin films (1000-fold change in the resistance) [17] by applying a magnetic field. Still manganites are an interesting subject of research due to their applicability as reading heads in the magnetic data storage technology e.g., but also in order to understand fundamental mechanisms appearing in these classes of materials. Their prominent features are versatile and exotic phase diagrams resulting from strong and not completely understood interactions between their specific electronical, magnetical and structural degrees of freedom. These phases are tunable by e.g. applied magnetic or electric fields, doping or chemical composition respectively and also by optical excitations. The latter opens the possibility of optically controlled high speed switches

e.g. [63]. The strong correlations require a separate theoretical treatment as the free-electron model and perturbation approaches are no longer sufficient to explain the electronic properties of these materials. An example is the incomprehensible at first sight behavior of a Mott insulator. While a conventional band insulator becomes insulating due to the Pauli exclusion principle when the highest occupied band is filled with two electrons per unit cell, a Mott insulator shows its insulating nature because of different correlation effects [16, 38, 39, 40, 44]. In case of strong electron-electron repulsion, double occupancy at the same site would be possible only at the prize of the Coulomb repulsion energy resulting in a splitting of the highest occupied band into two: one (lower) band for electrons occupying an empty site and another (higher) one for electrons sharing the same site as the first one. The outcome is an insulator at already one electron per site due to the filled lower and empty upper band in this so-called Mott insulator coming along with further extraordinary material properties specified briefly below. As in transition metals the spatial extension of the d orbitals is relatively small, the Coulomb correlation  $U$  for two electrons at one site is to be considered as large. Within the Hubbard model a simple Hamiltonian is set up taking this into account [11]:

$$H = -t \sum_{\langle ij \rangle \sigma} (a_{i\sigma}^+ a_{j\sigma} + h.c.) + U \sum_i n_{i\uparrow} n_{i\downarrow} \quad (2.1)$$

$n_{i\sigma} = a_{i\sigma}^+ a_{i\sigma}$  are the occupation number operators. The kinetic energy is described by the first term, with  $t$  representing the hopping integral and only nearest neighbor hopping processes considered. Interactions between electrons take place only when they are located on the same site via the constant on-site Coulomb repulsion  $U$ . The relative values of  $U$  and  $t$  determine physical properties like insulating and conducting states, respectively, as for  $U \gg t$  e.g. electrons tend to localize not investing Coulomb repulsion energy to be itinerant, which would be energetically favorable in this case. Delocalization of an electron, on the other hand, would lower the kinetic energy as it is proportional to the curvature of the electronic wavefunction or more precise to its derivative. Undoped, nondegenerate Mott insulators with  $n=1$  and  $U \gg t$  exhibit antiferromagnetic ordering due to the superexchange mechanism with the exchange integral  $J \sim 2t^2/U$  (cf. figure 2.6) as partial delocalization is energetically reasonable but requires antiferromagnetism [24]. Interesting phase transitions (e.g. a metal to insulator transition in the CMR region) can be investigated if these competing energies converge, as can be seen in the phase diagram of  $\text{La}_{1-x}\text{Ca}_x\text{MnO}_3$  e.g. (cf. figure 2.10). Several

extensions to the Hubbard model (e.g. the electron-phonon coupling via the Jahn-Teller effect) should be taken into account for a more detailed and exact description, but though ignoring so far the role of ligands, multiband effects (only electrons in a single band are considered) and intersite Coulomb forces e.g., the simplified Hamiltonian of the Hubbard model depicts low-energy and low-temperature properties of strongly correlated transition metal oxides often well (including the transition between a Mott insulator to a metal) [16]. A full Hamiltonian taking the most important contributions to the physics of electrons in manganites into account can be given by [9]:

$$H = H_{kin} + H_{Hund} + H_{AFM} + H_{el-ph} + H_{el-el}, \quad (2.2)$$

with  $H_{kin}$ , the kinetic term of the  $e_g$  electrons,  $H_{Hund}$ , the Hund coupling between the  $e_g$  electron spin and the localized  $t_{2g}$  spins,  $H_{AFM}$ , the AFM Heisenberg coupling between nearest neighbor  $t_{2g}$  spins,  $H_{el-ph}$ , the coupling between the  $e_g$  electrons and the local distortions of the  $\text{MnO}_6$  octahedron and  $H_{el-el}$ , the Coulomb interactions among the  $e_g$  electrons. Most models found in literature are simplifications of this ansatz. If the lowest charge-carrying excitations are determined by a gap described by the Hubbard model (energy difference:  $U$  between lower and upper Hubbard band) or by a transfer of an electron from an anion valence band (oxygen e.g.) to the upper Hubbard band (energy difference:  $\Delta_{CT}$ ), classifies a material into a Mott-Hubbard ( $U < \Delta_{CT}$ ) or into a charge-transfer insulator ( $U > \Delta_{CT}$ ). In the manganite oxides the special case of orbitally degenerate 3d orbitals leads to the introduction of the modified so-called orbitally degenerate Hubbard model (ODHM) in the theoretical treatment of this class of materials. The ODHM includes furthermore the orbital to the spin and charge degrees of freedom.  $\text{LaMnO}_3$  sorts into the group of manganites exhibiting all above introduced features and is explained in more detail in the following subchapter.

## 2.2 Mixed valence manganese oxides and $\text{LaMnO}_3$

Doped manganites can be organized into the structure family of the Ruddlesden-Popper series  $(A,B)_{1+n}\text{Mn}_n\text{O}_{3n+1}$  (with A a divalent and B a trivalent cation). In case of  $n \rightarrow \infty$ , mixed valence manganese oxides  $\text{Re}_{1-x}^{3+}\text{Ae}_x^{2+}\text{MnO}_3$  (R = trivalent rare-earth cation, Ae = divalent alkali or alkaline earth cation), exhibiting perovskite structures, are achieved. One end-member at  $x=0$  e.g.

is the insulating undoped parent compound  $\text{LaMnO}_3$ . Its unit cell, the perovskite structure and an oxygen octahedron surrounding the manganese atom are depicted in figure 2.1.

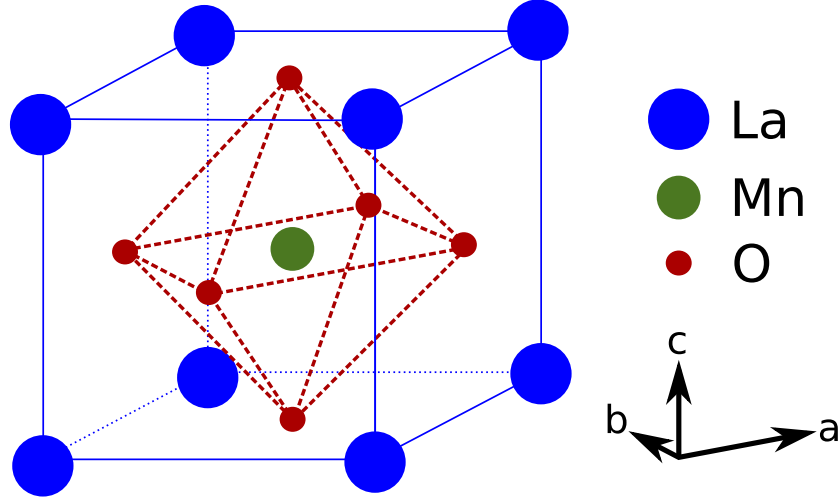


**Figure 2.1:** Undistorted perovskite unit cell of  $\text{LaMnO}_3$ .

As already mentioned, the interesting physical properties of the transition metal compounds like in the manganese atom in this case arise from the electronic structure. The electronic configuration of a manganese atom in free space (spherical environment) is that of argon plus 2 electrons in a filled  $4s^2$  and 5 in a half filled  $3d^5$  shell [1]. In  $\text{LaMnO}_3$  the manganese atom is surrounded by an oxygen octahedron creating an octahedral ligand field. In this (pseudo)cubic environment the crystal field splits the former fivefold degenerate 3d levels into 2 upper  $e_g$  and 3 lower  $t_{2g}$  subshells energetically separated by  $\Delta_{cf}$  (see figure 2.2).

A cubic crystal field now leads to modified eigenfunctions of the d orbitals. They can be described by a linear combination of the spherical harmonics following from the Schrödinger equation for atoms resulting in the shapes shown in figure 2.2 embedded in the regular oxygen octahedra [24, 53]. Both  $e_g$  orbitals ( $d_{3z^2-r^2}$  and  $d_{x^2-y^2}$ ) point directly towards negatively charged oxygen atoms in this octahedral surrounding, while all 3  $t_{2g}$  orbitals ( $d_{xy}$ ,  $d_{xz}$ ,  $d_{yz}$ ) point between them explaining the energetic arrangement of the 2 subshells. Within this compound, the manganese atom becomes trivalent ( $\text{Mn}^{3+}$ ) adopting the high spin electronic configuration  $t_{2g}^3 e_g^1$  for the remaining 4 electrons in the 3d shell, which results from the Hund's rules and the fact that  $\Delta_{cf}$  is small in comparison to the spin pairing energy ( $\Delta_{cf} < 3 J_H$  with  $J_H$  the Hund's rule coupling [24]). The energy scheme in cubic environment is

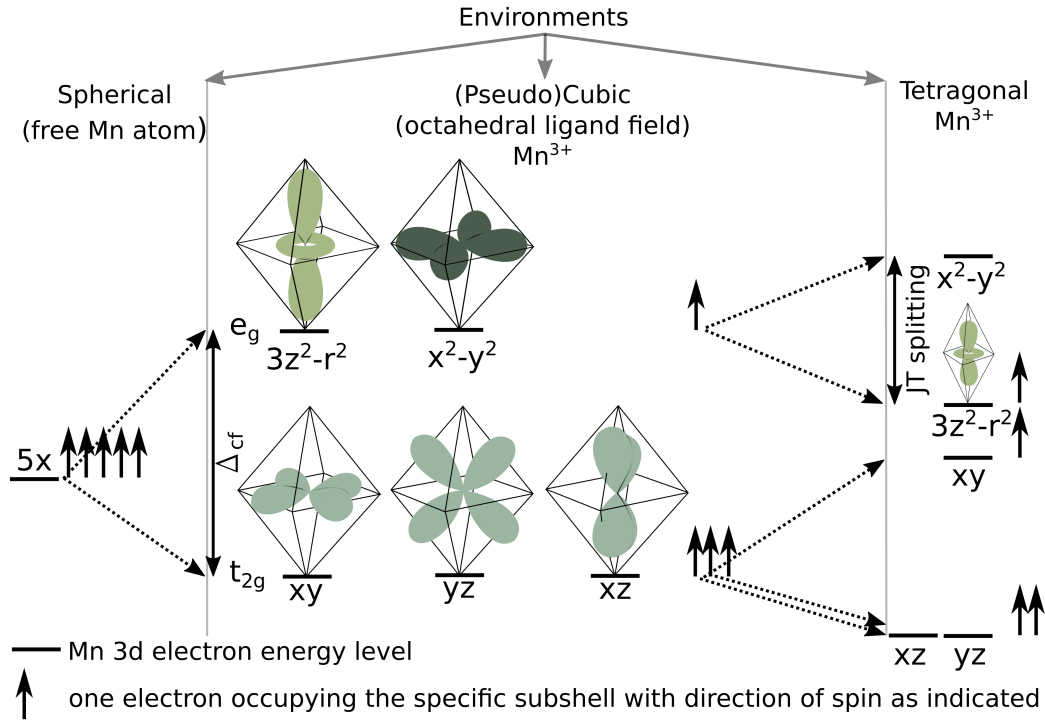


**Figure 2.2:** (Partially adapted from: [65]) Mn 3d orbitals in different environments and the corresponding lattice distortion and energetical splitting (see text).

sustainable for  $\text{LaMnO}_3$  down to  $\sim 780$  K. Below this temperature,  $\text{LaMnO}_3$  shows orbital ordering as revealed by elastic X-ray techniques [41], and a so called Jahn-Teller (JT) splitting has to be taken into account. The JT effect states that in case of electronic degeneracy, a lowering of the symmetry of a system occurs in form of a lattice distortion and a corresponding lifting of the orbital degeneracy due to the electron-lattice coupling. As in  $\text{LaMnO}_3$  the  $e_g$  subshell is double-degenerate and singly occupied, the JT splitting results in an upper unoccupied and a lower occupied  $e_g$  level, which is energetically favorable. The lattice is distorted from a cubic symmetry as the former regular octahedron elongates or shortens respectively along specific Mn-O bond directions. Figures 2.3 and 2.9 demonstrate the shifted oxygen positions in relation to the occupied ordered orbitals (cooperative JT distortion).

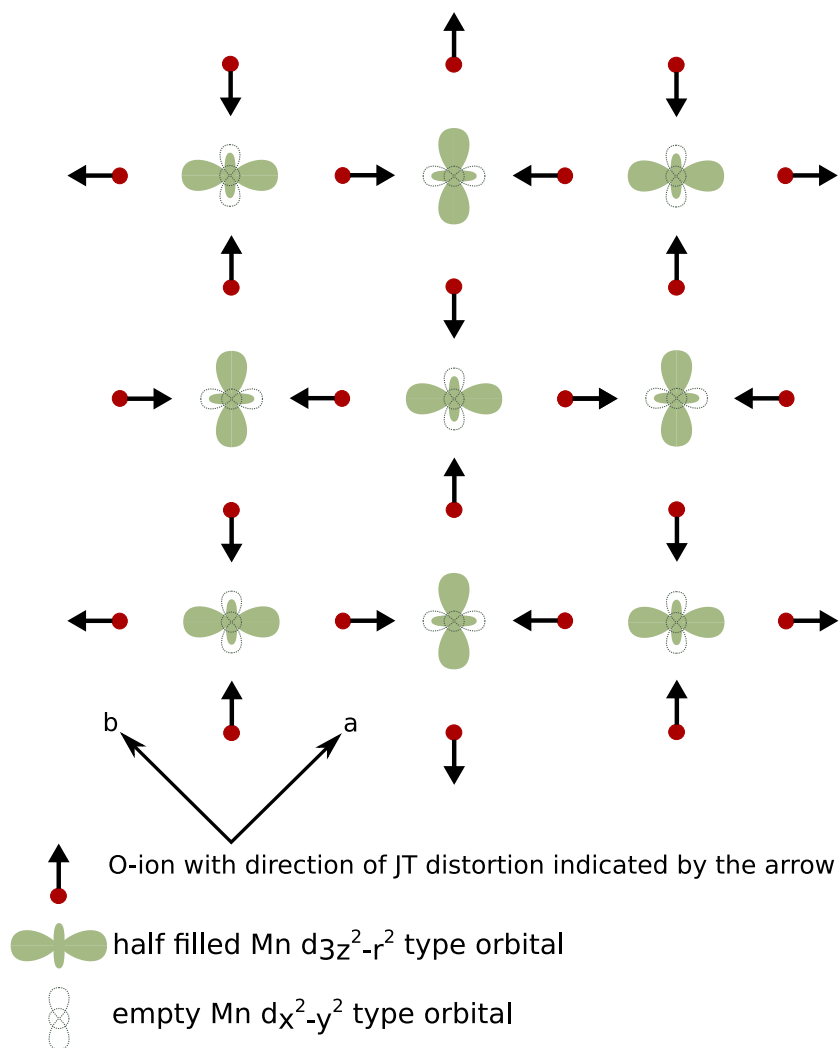


**Figure 2.3:** Top view of the Mn 3d  $e_g$  orbital ordering within the ab plane. JT distortions are indicated by black arrows, while tilting and rotation distortions are omitted in this scheme.

One tetragonal JT distortion of  $\text{LaMnO}_3$  e.g. lowers the  $d_{3z^2-r^2}$  orbital energy and increases that of the  $d_{x^2-y^2}$  orbital (see figure 2.2). This purely  $Q_3$  - distortion (see explanation below) is one possibility that can be associated with  $\text{LaMnO}_3$  [24]. In general possible JT distortions of the oxygen octahedron ( $Q_2$  and  $Q_3$ ) are depicted in figure 2.4.

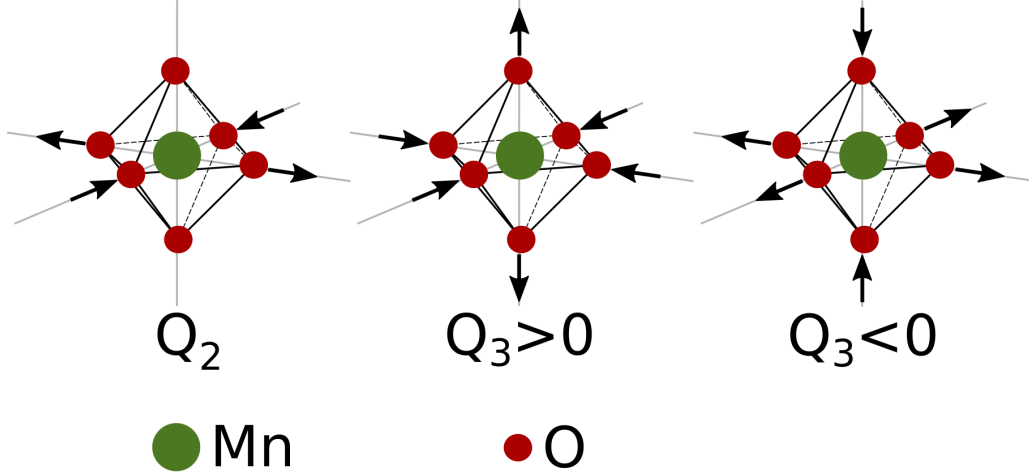


**Figure 2.4:** Examples of JT distortions of  $e_g$  symmetry (purely  $Q_2$  or  $Q_3$  respectively). The corresponding displacements of the regular oxygen octahedra are illustrated by arrows (adapted from: [24, 49]).

These specific orthorhombic or tetragonal JT distortions and the shape of the JT-ion 3d  $e_g$  orbital influence and stabilize each other. The concrete assignment of the lower occupied  $e_g$  orbital to the  $d_{3z^2-r^2}$  orbital might be a simplification as also a mixing of the  $Q_2$ - and  $Q_3$ -distortions accompanied by an effective mixture of the  $e_g$  symmetry orbitals has to be taken into account. The combined  $Q_2$  and  $Q_3$  Jahn-Teller distortion can be associated with an orbital-mixing relation of the  $e_g$  symmetry orbitals described by an angle  $\theta$  in the following way [24, 58, 61](see figure 2.5):

$$\begin{aligned} \theta_{occ}^{\pm} &= \cos \frac{\theta}{2} |3z^2 - r^2\rangle \pm \sin \frac{\theta}{2} |x^2 - y^2\rangle \\ \theta_{unocc}^{\pm} &= \pm \sin \frac{\theta}{2} |3z^2 - r^2\rangle - \cos \frac{\theta}{2} |x^2 - y^2\rangle \end{aligned} \quad (2.3)$$

$\pm$  refers to the corresponding sublattices due to the orbital ordering. And the indices *occ* and *unocc* stand for the occupied and unoccupied Mn 3d ground state orbital wave functions of  $e_g$  symmetry. The lattice distortion  $Q$  can be decomposed into the two basic JT distortions like:

$$(Q_3, Q_2) = Q(\cos\Theta, \sin\Theta). \quad (2.4)$$

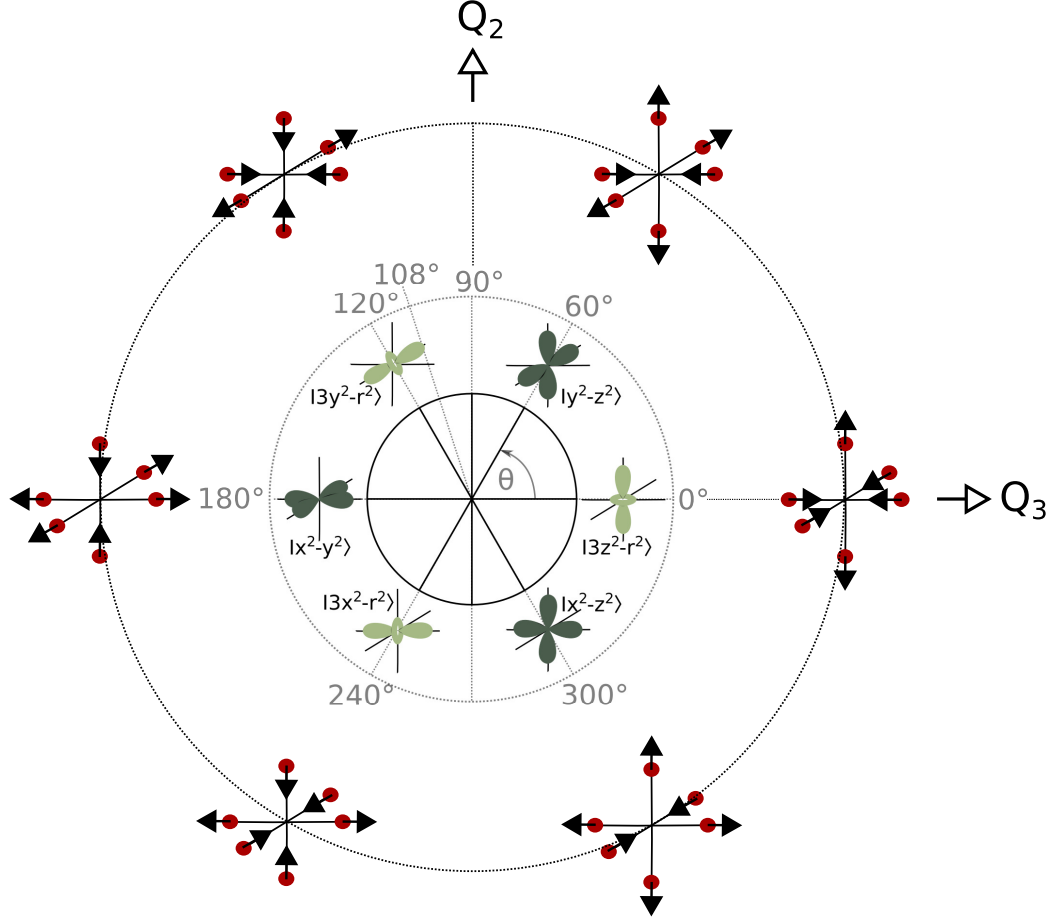


**Figure 2.5:** (Adapted from [24].) Inner circle: different possible orbital states of a Mn 3d  $e_g$  electron and outer circle: corresponding combinations of the JT lattice distortions within the  $Q_2$  / $Q_3$  plane. Both are described by the mixing angle  $\theta$  (see text).

Commonly the lattice distortions and the corresponding orbital occupations follow each other as far as only nearest neighbor ligands and no other influences contribute to the electron energy [24]. For this reason, in the following the equation  $\theta = \Theta$  should hold. As the  $e_g$  electrons couple likewise to the  $Q_2$ - and  $Q_3$ -distortions, the energies of the different resulting states due to the mixing - depicted by the outer circle in figure 2.5 - are equal. Or in other words - at amplitude  $Q = \sqrt{Q_3^2 + Q_2^2}$  the model Hamiltonian predicts a minimum [2, 34], which is degenerate with respect to angle  $\Theta$ . This assumption

is valid unless anharmonic or strain terms are added to select a direction in  $Q_2/Q_3$  space leading to energies dependent on  $\Theta$  [2]. However, as local compression of the orbital is practically never observed in  $e_g$  systems but "cigar-shaped" elongated octahedral orbitals instead, anharmonicity effects and higher order JT interactions may be necessary to be taken into account [24]. The evaluation of JT distortions observed by neutron scattering suggests an angle of  $\sim 108^\circ$  [50].

In literature, controversial arguments can be found whether the orbital ordering in  $\text{LaMnO}_3$  arises from the Jahn-Teller effect or from the superexchange model [2, 3, 36, 52]. The latter can as well explain the interdependent orbital and magnetic structures within the Goodenough-Kanamori-Anderson (GKA) rules [12]. In  $\text{LaMnO}_3$  a connection via the p orbital of the oxygen between two half-filled or two empty manganese orbitals leads to an antiferromagnetic coupling, while a connection between a half-filled and an empty orbital or between a filled and a half-filled orbital leads to ferromagnetic coupling due to the GKA rules [63]. Figure 2.6 illustrates these properties resulting from the Pauli exclusion principle and the Hund's rule respectively.

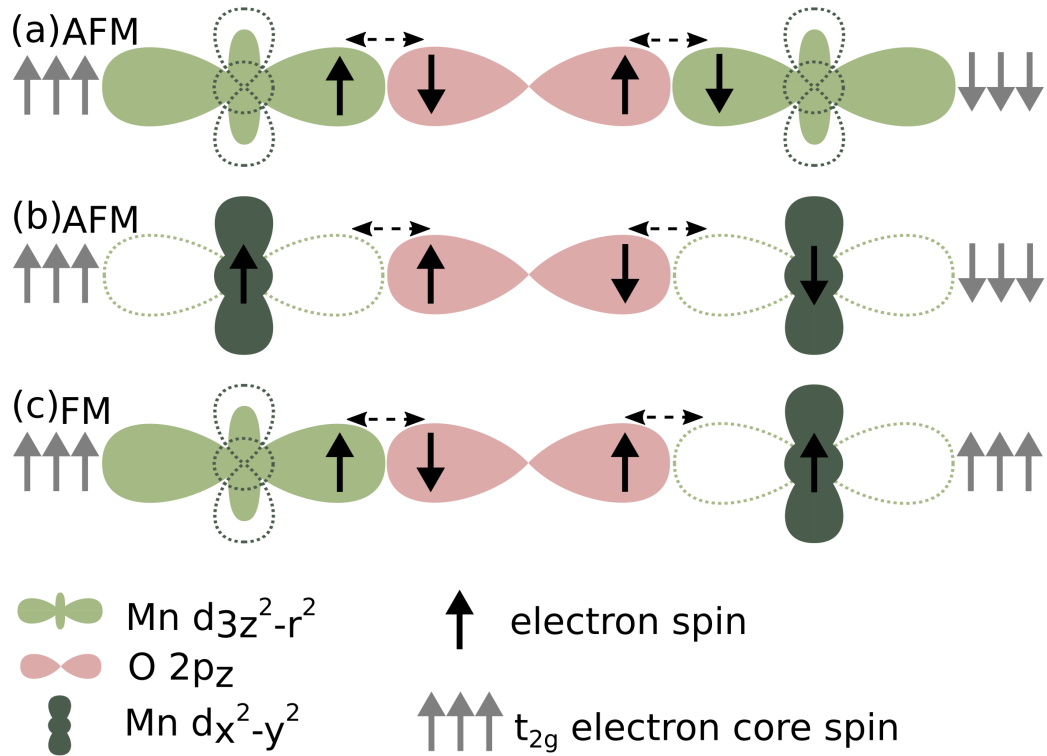


**Figure 2.6:** Examples of the superexchange mechanism in general on the basis of two  $\text{Mn}^{3+}$   $d_{3z^2-r^2}$  typ orbitals pointing towards each other and bridged by an O  $2p_z$  orbital (in different surrounding conditions): a) 2 half-filled  $d_{3z^2-r^2}$  typ orbitals antiferromagnetically connected - through a covalent bonding with the oxygen - as the by horizontal arrows indicated virtual electron transfer can take place only in this configuration due to the Pauli exclusion principle. b) Antiferromagnetic order between two empty  $d_{3z^2-r^2}$  typ orbitals c) Half-filled  $d_{3z^2-r^2}$  typ orbital ferromagnetically connected to a manganese ion with an empty  $d_{3z^2-r^2}$  typ orbital. Due to a non-zero probability density function of the spin-up O  $2p_z$  electron at the empty  $d_{3z^2-r^2}$  orbital on the right hand side, it polarizes the  $t_{2g}$  core electrons ferromagnetically because of Hund's rule (adapted from:[43]).

In this way in case of  $\text{LaMnO}_3$ , the spin interaction of two manganese atoms occurs via a bridging oxygen atom [63]. From the rules described above follows that the half-filled  $t_{2g}$  orbitals interact antiferromagnetically in all directions, additionally unoccupied  $e_g$  orbitals do so along the  $c$ -axis [9]. In contrast within the  $ab$  plane with occupied  $d_{3z^2-r^2}$  type orbitals ordered in the manner (mutually orthogonal) that an O  $2p$  orbital bridges this occupied one with an unoccupied  $d_{x^2-y^2}$  type orbital (see figure 2.3), the resulting magnetic order becomes ferromagnetic particularly as well as the  $\sigma$ -bonding of the  $e_g$  orbitals is stronger than the  $\pi$ -bonding of the  $t_{2g}$  orbitals. This is because of the greater overlap of the  $\sigma$ -bond wavefunctions and their smaller energy difference. The outcome of the GKA rules with regard to  $\text{LaMnO}_3$  is a ferromagnetic coupling of the manganese atoms within the  $ab$  plane and an antiferromagnetic coupling between those  $ab$  planes along the  $c$ -axis (A-type AFM ordering) at  $T_N=140$  K accompanied by a staggered orbital ordering within the  $ab$  plane, which is repeated in the neighboring layers along the  $c$ -axis (C-type orbital ordering) with an inset already at  $\sim 780$  K (see figure 2.7) [67].

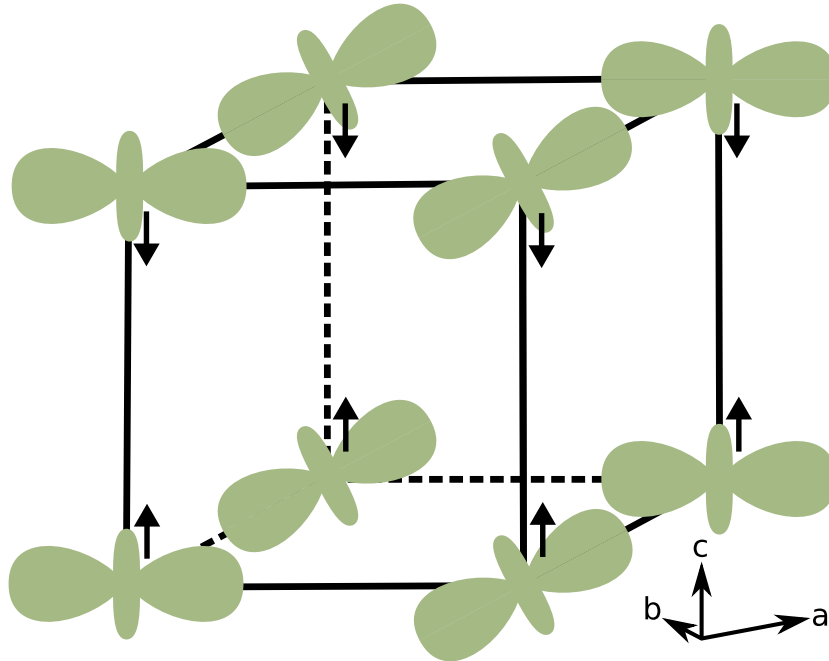


**Figure 2.7:** Three-dimensional orbital and spin ordering (black arrows) of the Mn  $3d e_g$  orbitals (see text).

Furthermore, the chemical composition influences the deviation of the ideal cubic perovskite structure. In order to balance a possible size mismatch

between the A-site cation (like La) and the Mn-ion causing internal strain and to achieve closer packing, the oxygen octahedra tilt about the b-axis and rotate around the c-axis in alternating directions (see figure 2.8) [9, 24, 46].

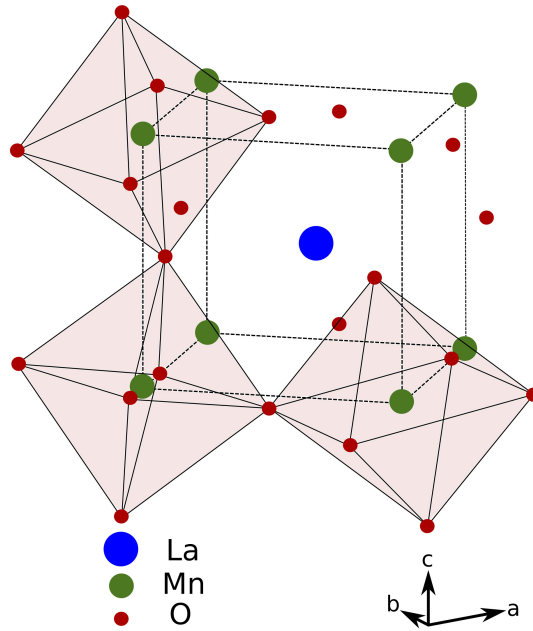


**Figure 2.8:** Tilting and rotation of the oxygen octahedra in LaMnO<sub>3</sub>. JT distortions are omitted in this scheme (adapted from: [59]).

The size mismatch is expressed by the tolerance factor:

$$t = \frac{(r_A + r_O)}{\sqrt{2}(r_{Mn} + r_O)}, \quad (2.5)$$

with the ionic radii  $r_A$ ,  $r_{Mn}$  and  $r_O$  of the A-site, Mn- and O-atoms respectively. Around a tolerance factor of 1 the cubic structure is preserved while

for lower  $t$  (smaller A-site cation) the cubic structure distorts involving a decrease of the Mn-O-Mn bond angle from  $180^\circ$  towards smaller angles (see figure 2.9). In case of  $\text{LaMnO}_3$ , this angle becomes  $\varphi \sim 155^\circ$  [4] and the distortion orthorhombic.

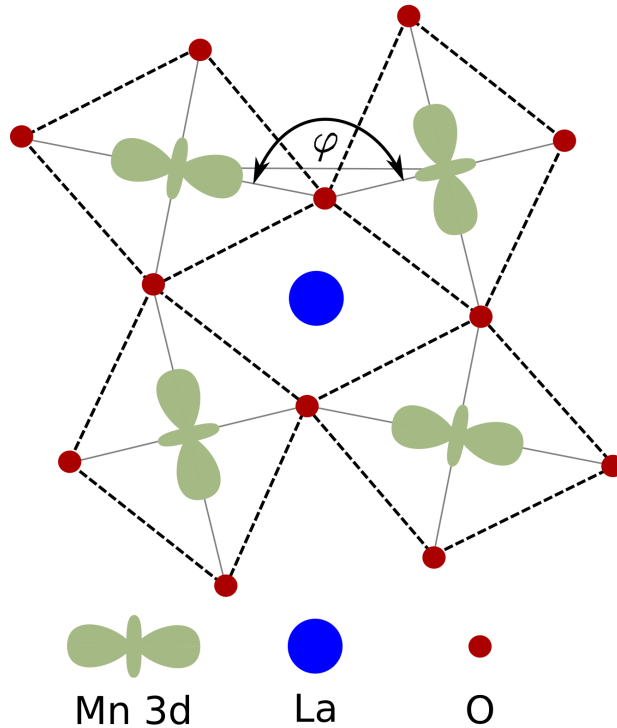


**Figure 2.9:** Top view of the JT distortions and orbital ordering in the  $ab$  plane. The rotations of the oxygen octahedra are indicated as well as the Mn-O-Mn bond angle  $\varphi$  (see text)(adapted from [57]).

Summing up,  $\text{LaMnO}_3$  orders into the exemplary phase diagram  $\text{La}_{1-x}\text{Ca}_x\text{MnO}_3$  of a doped manganite as an antiferromagnetic insulator, which we have investigated at room temperature (see light green cross in figure 2.10(a)).

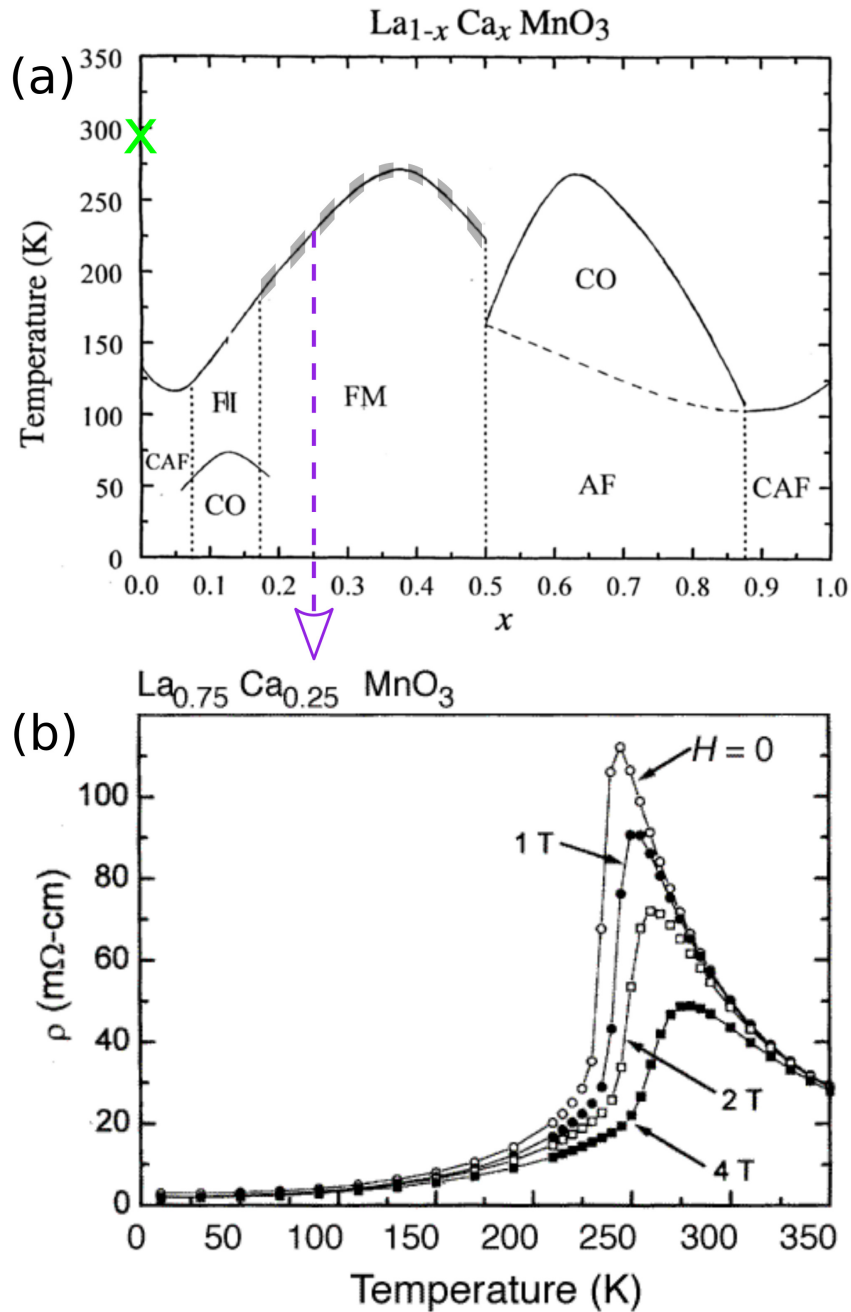


**Figure 2.10:** (a) Phase diagram of the doped manganite  $\text{La}_{1-x}\text{Ca}_x\text{MnO}_3$  (adapted from: [35]) with  $\text{LaMnO}_3$  position investigated within this thesis emphasized by the light green cross. Depicted are the following phases at lower temperatures: CAF (Canted Antiferromagnetic Insulator), FI (Ferromagnetic Insulator), CO (Charge Ordered Insulator), FM (Ferromagnetic Metal) and AF (Antiferromagnetic Insulator). Not shown is the PI (Paramagnetic Insulator) phase at higher temperatures separated to the FM phase by the CMR region (light gray striped area). The CMR effect (strong change of resistivity around  $T_c$  by applying a magnetic field) at a sample with doping  $x=0.25$  is demonstrated in (b) (adapted from: [54]).

By doping  $\text{Ca}^{2+}$  ions into  $\text{LaMnO}_3$  (hole doping), the percentage of  $\text{Mn}^{4+}$  ions ( $t_{2g}^3 e_g^0$ ) in the manganite is determined. While  $\text{Mn}^{3+}$  is a JT active ion,  $\text{Mn}^{4+}$  due to its unoccupied  $e_g$  subshell is not JT active. This doping results in diverse phases of the rich phase diagram depicted in figure 2.10(a). The most interesting region is around 250 K in the range of  $x$  between  $\sim 0.2$  and  $0.5$  (light gray striped area in figure 2.10(a)), as the CMR effect appears in this area. Strong changes in the resistivity occur crossing  $T_c$  from the paramagnetic insulating into the ferromagnetic metallic region. This transition is not only influenced by the temperature, but can also be driven by a magnetic field. An applied magnetic field leads to a shift of the transition temperature  $T_c$  into the ferromagnetic part of the phase diagram towards higher temperatures accompanied by a broadening of the transition. In the region around  $T_c$ , a strong decrease in resistivity with  $H$  is the observed result. This so called negative magnetoresistance is demonstrated in figure 2.10(b). The arising conductivity can be explained by the double exchange mechanism allowing  $e_g$  electrons to hop from a  $\text{Mn}^{3+}$  to a  $\text{Mn}^{4+}$  ion via an oxygen ion in between, as demonstrated in figure 2.11.

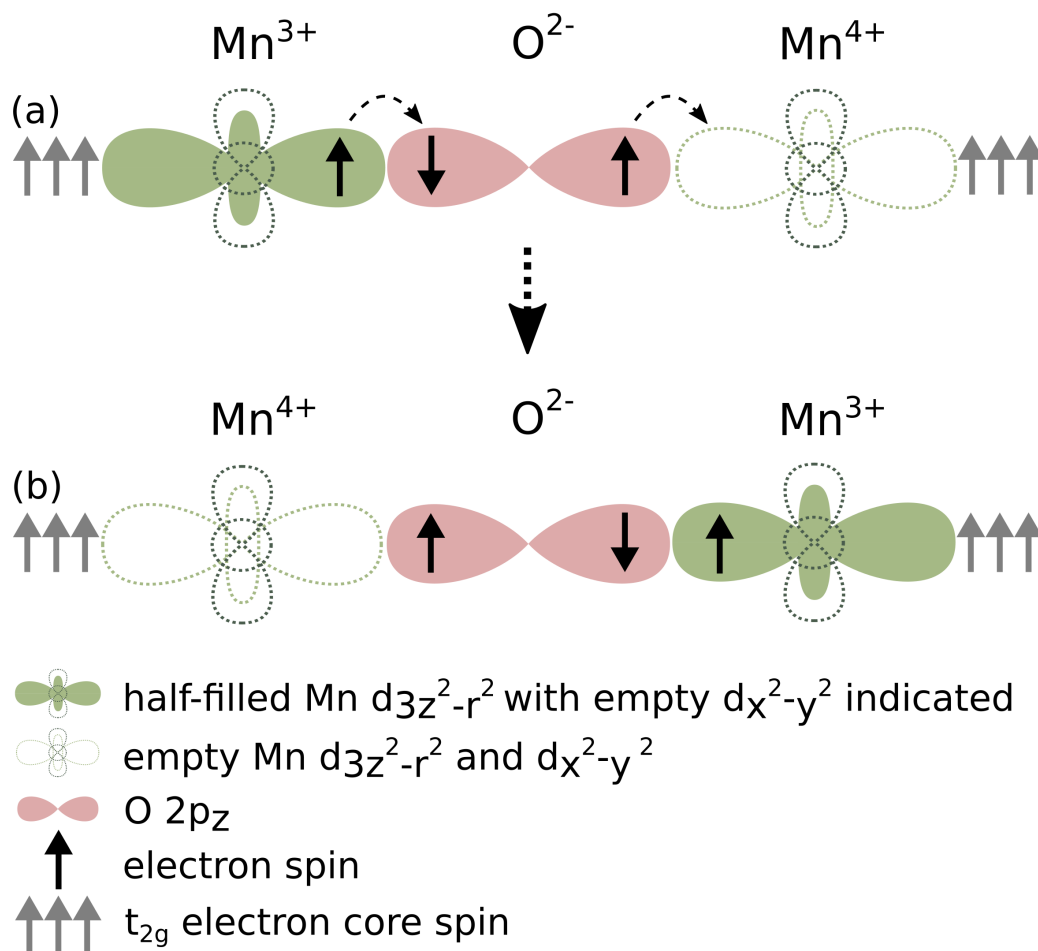


**Figure 2.11:** Depicted is the electron hopping process within the double exchange mechanism. Electrical conductivity accounts for a ferromagnetic ordering between the Mn-ions and vice versa within this mechanism as no energy due to Hund's rule coupling has to be invested during the hopping process this way. Mixed valencies (half-filled  $\text{Mn}^{3+}$   $d_{3z^2-r^2}$  orbital connected to an empty  $\text{Mn}^{4+}$   $d_{3z^2-r^2}$  orbital) also promote this mechanism saving coulomb repulsion energy  $U$  (adapted from: [43]). a) Initial state b) After the electron hopping process.

Ferromagnetism supports this mechanism and an applied magnetic field provides the ferromagnetism by aligning the  $t_{2g}$  core spins for their part influencing the conducting  $e_g$  electrons through a strong Hund's coupling. Quantitatively the large change in resistivity, however, cannot be described by the double exchange mechanism alone (as disordered spins do not scatter electrons enough). A solution was found by introducing a strong JT coupling that localizes the  $e_g$  charge carriers via the electron-phonon coupling above the transition temperature  $T_c$  [9, 37]. In addition, phase separation should be mentioned as it is also discussed to be important to explain the CMR effect (percolative conduction) [10]. As already mentioned at the beginning of this chapter, localization and delocalization of the electrons determine the phase diagram of the doped manganites, which can also be described as a competition of the JT and the double exchange effect.

The importance of the electron-phonon coupling - with regard to the CMR effect e.g. - as well as coupled spin, orbital and charge phenomena were demonstrated by means of the  $\text{La}_{1-x}\text{Ca}_x\text{MnO}_3$  phase diagram. Some of these effects also determine a controversial discussion in literature concerning the origin of the orbital ordering in  $\text{LaMnO}_3$ . Solving the question what leads to orbital ordering could shed light on mechanisms working at other parts of the phase diagram as well motivating further investigations. As mentioned before, two mechanisms are proposed: orbital ordering triggered by the JT interaction or by superexchange. The orbital ordering originating from superexchange can be described with an Hamiltonian resulting from the degenerate Hubbard model that takes the orbital occupation, the spin and in addition their interaction into account [9, 28, 29]. A coupling to the lattice is not necessary to receive orbital ordering within this description. While within the JT mechanism an interaction of the orbitals to the lattice via the electron-phonon coupling is essential, this latter case in contrast does not depend on the magnetic ordering. Though both scenarios result in orbital ordering, they differ in the energy scale that drives it and therefore as well in the energy scale of the expected corresponding excitation spectrum, as due to the symmetry breaking by the orbital ordering a new particle - the so called orbiton - should appear. In the JT (lattice distortion) scenario the dominating influence of the electron-phonon coupling leads to an energy scale in the order of magnitude of about 1.5 eV [2, 3, 36] and to local excitations with no dispersion. Within the purely electronic mechanism of orbital ordering (related to the strength of the Coulomb on-site repulsion) energies about 0.16 eV are predicted [2, 3, 52] and collective excitations with strong dispersion.

Figure 2.12 depicts an idea of an orbital wave in the orbital-ordered ground

state proposed by Saitoh and coworkers [52].

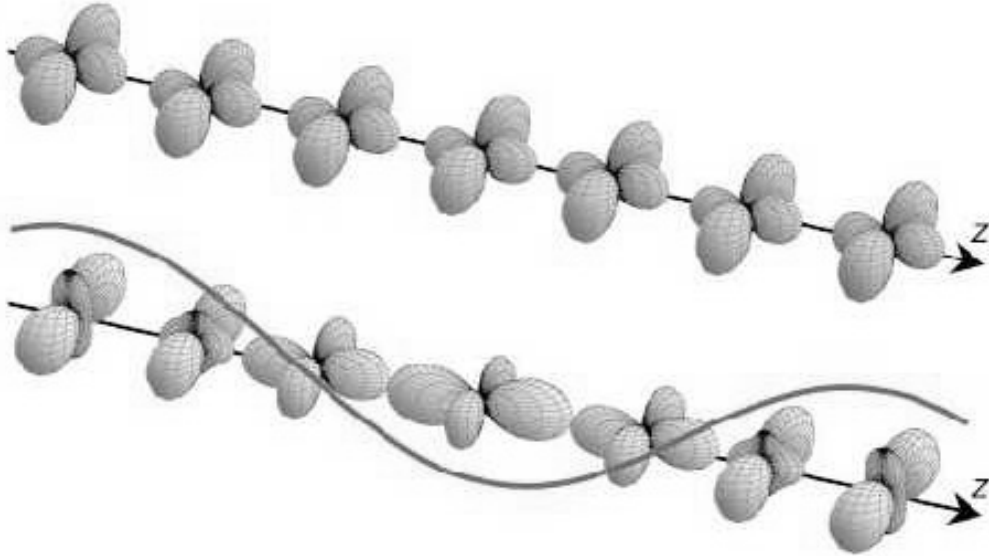


**Figure 2.12:** Schematic illustration of a possible orbital wave [52]. Electron orbitals in the undisturbed ordered ground state (upper row). Orbital wave in form of a modulation in the relative shape of the ordered orbitals propagating through the crystal (lower row).

By changing one orbital occupation state, this deviation of the orbital-ordered state could propagate through the crystal via the interactions between orbitals at different ions. This collective oscillation of the partly filled  $e_g$  subshell can be compared with the spinwave mechanism working in a similar way. The change of the orbital occupation state could be realized by a photon-induced exchange of electrons between e.g. nearest neighboring Mn-ions or nearest neighboring O- and Mn-ions. The incident photon excites an electron (from an O 2p or Mn-ion) into the unoccupied Mn  $e_g$  orbital, while within a second photon interaction one electron returns. As this scattering process does not leave the Mn-ion in necessarily the same occupation state as it showed before, an orbiton might be excited this way. Raman measurements at  $\text{LaMnO}_3$  with an excitation energy of 2.4 eV displaying excitations interpreted as orbitons within the above presented smaller energy scale scenario seem to confirm this prediction [52]. Selected spectra measured at  $T = 9$  K are displayed in Fig. 2.13.

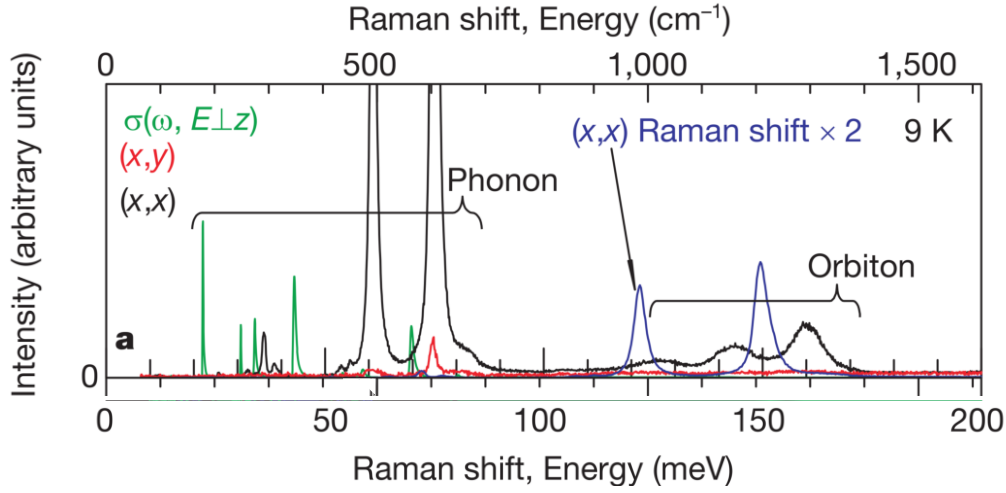


**Figure 2.13:** Raman spectra measured by Saitoh and coworkers (black and red) as well as the estimated two-phonon region (blue). Controversially discussed is the origin of the peaks between about  $1000 \text{ cm}^{-1}$  and  $1400 \text{ cm}^{-1}$  (see text) (adapted from: [52]).

The black curve is measured in parallel polarization configuration along the in-plane crystal axis ((x,x) in their labeling). The 3 peaks between wavenumbers of about  $1000 \text{ cm}^{-1}$  and  $1400 \text{ cm}^{-1}$  ( $125 \text{ meV}$ ,  $145 \text{ meV}$  and  $160 \text{ meV}$  respectively) are assigned to an orbiton. The energetically highest visible peak at  $\sim 1300 \text{ cm}^{-1}$  corresponds to  $\sim 0.16 \text{ eV}$  and cannot be reproduced by any combination of the observed one-phonon Raman modes as they argue. The doubled Raman shifts (blue line) of the Jahn-Teller modes at  $\sim 60 \text{ meV}$  and  $\sim 75 \text{ meV}$  result in a maximal peak position at about  $150 \text{ meV}$ , as shown for comparison. Charge excitations and two-magnon scattering are also excluded to explain the Raman bands between  $1000$  and  $1400$  wavenumbers in (x,x) polarization configuration, as the charge gap energy in the ground state of  $\text{LaMnO}_3$  is in the order of magnitude of eV and magnon scattering is prohibited due to the A-type AF ordering. Controversial interpretations of this orbiton assignment can be found in literature [1, 13]. The presumed orbiton is related to an overtone of a conventionally IR active mode becoming allowed due to possible symmetry breaking is another interpretation [13]. The fact that the coupling of orbitons to phonons is omitted in the theoretical interpretation is rejected as well [1]. Effectively figure 2.13 gives reason to the assumption that a disorder induced mode at  $\sim 80 \text{ meV}$  ( $\sim 650 \text{ cm}^{-1}$ ), which is indicated as a foot at the mode at  $\sim 75 \text{ meV}$ , might be necessary to be taken into account, as this energy doubled yields quite exactly the energy of the last peak of the estimated orbiton at  $\sim 1300 \text{ cm}^{-1}$ . Debated in

literature is also the assignment of the energy gap around 2 eV. A charge-transfer between the O 2p and the Mn 3d orbitals is under consideration [5, 52, 60], but likewise a Mott-Hubbard gap [26]. The theoretical idea of a JT gap i.e. an intramolecular peak (d-d) due to the Franck-Condon process can be found in [3]. A manifestation of the Franck-Condon effect is expected in the Raman spectrum especially if the excitation energy is near the Jahn-Teller gap. Multiphonon Raman features of the Jahn-Teller related vibrations should appear with enhanced intensity giving the motivation for a resonance Raman scattering study within this thesis to further solve the question of the mechanism driving the orbital ordering and the assignment of the electronic gap around 2 eV. An introduction to the Franck-Condon mechanism is, therefore, given in the following sub-chapter.

## 2.3 Franck-Condon mechanism

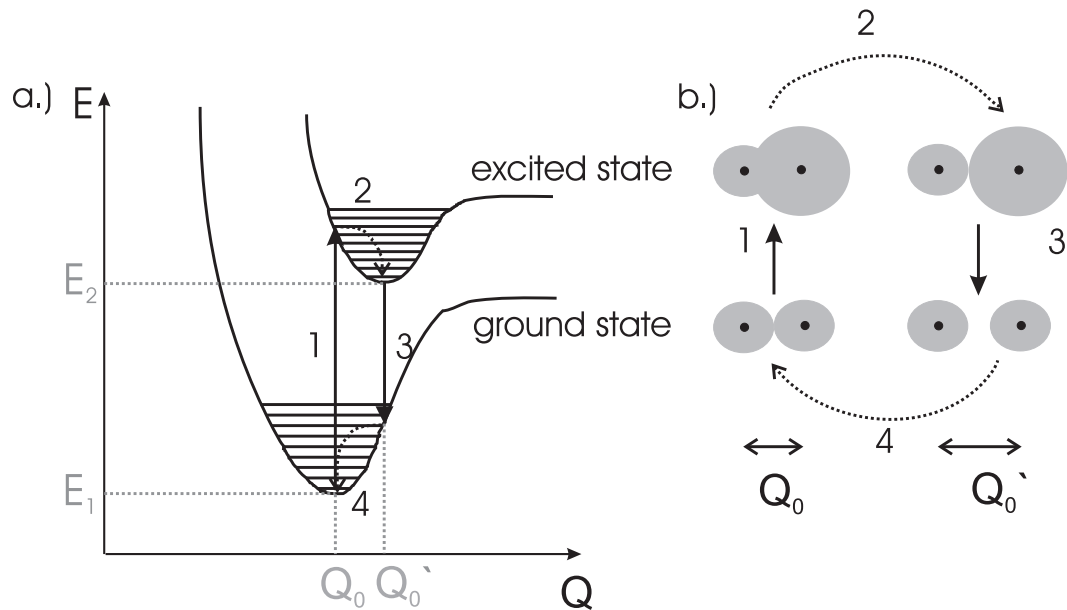


**Figure 2.14:** Schematic of the Franck-Condon mechanism in a diatomic molecule in four steps: a.) Oscillator potentials of the ground and excited state. Depicted are the energy levels of the vibronic states in dependence of the generalized coordinate  $Q$  - in this case the nuclear separation  $r$ . b.) 'Dumb-bell' diagrams of the molecule with its two different equilibrium separations  $Q_0$  and  $Q'_0$  during the Franck-Condon process. The radius of one atom is increased in the excited state (adapted from: [31]).

Within the Franck-Condon mechanism the intensities between different vibronic (vibrational-electronic) transitions can be calculated. A simple example to explain this mechanism can be given for a diatomic molecule [31]. In a molecule the electronic states involve vibrational levels as a consequence of the vibrations of the atoms about their bonds. A common way to depict the possible vibronic spectra of a molecule are configuration diagrams (2.14a), showing the electronic energy in terms of the configuration coordinates. In this case of a diatomic molecule these are represented by the internuclear separation, in a more general case by generalized coordinates  $Q$  (2.14b). An illustration as in Fig. 2.14a is allowed because the electronic and nuclear motions can be seen as independent due to much heavier nuclei than electrons. An electronic transition takes approximately  $10^{-14} - 10^{-15}$  seconds (in the visible and ultraviolet spectral region), while a period of a nuclear vibration takes about  $10^{-13}$  seconds (in the infrared spectral range). During the transitions between the ground state and the excited state (2.14a) no significant change of the internuclear separation appears (Franck-Condon principle). Consequently, these transitions have to be depicted with vertical lines. The interplay of the attractive forces of the atoms and the electron-electron and proton-proton repulsion results in two different equilibrium separations  $Q_0$  and  $Q'_0$  of the ground and excited state, as the radius of one atom in the excited state is increased and the overlap of the electronic wave functions is diverse (see 'dumb-bells' in figure 2.14b). Figure 2.14a.) and b.) demonstrate the Franck-Condon principle in four steps: At first a photon is absorbed and delivers the molecule into an excited state (step 1) whereby the nuclear separation  $Q_0$  is not altered so far. This means, an electron is promoted from the bottom of the ground state to a vibrational excited upper state. Shortly after (less than 1 ps in a solid) a non-radiative vibrational relaxation occurs (step 2) - the electron relaxes to the bottom of the upper band - accompanied with a nuclear separation of now  $Q'_0$ . This is followed by a re-emission of a photon (step 3) after  $\sim 1$  ns with the internuclear separation constant at  $Q'_0$  during this step. As the molecule is not situated in an equilibrium position with  $Q'_0$  in the ground state, a further vibrational relaxation process occurs (step 4), so that the equilibrium position of  $Q_0$  in the ground state is rebuilt. These vibrational relaxation processes can be understood as excitations of specific vibrational modes of the material (see step 2 and 4 in figure 2.14a). The Raman intensities of the vibrational modes depend on the electron-phonon coupling constant  $g$  and are proportional to  $g^{2n}$  in the conventional Raman scattering process for a  $n$ -phonon peak. Within the Franck-Condon mechanism the intensities of  $n$ -phonon peaks are proportional to  $g$  due to in this case shifted oscillator potentials. In general  $g$  is a small number of  $\sim 10^{-1} - 10^{-2}$ . In the Franck-Condon mechanism  $g$  is correlated with the shift of

the equilibrium positions of the initial and final state of the shifted oscillator potentials. The  $g$ -dependencies in the conventional Raman process and the Franck-Condon mechanism should allow for enhanced multiphonon excitations within the Franck-Condon process. The following calculations give a mathematical expression of the above explained. As a result of the electric dipole approximation, the matrix element for a transition from an initial state  $\Psi_1$  to a final state  $\Psi_2$  can be given as:

$$M_{12} = \langle 2 | e\vec{r} \cdot \vec{\mathcal{E}}_0 | 1 \rangle, \quad (2.6)$$

with  $\vec{r}$ , the position vector of the electron and  $\vec{\mathcal{E}}$ , the electric field of the light wave. Because of the different masses of the electrons and nuclei, another approximation (Born-Oppenheimer) can be taken into account for the total wave functions of the vibronic states. The wave function for an electronic state  $i$  and a vibrational level  $n$  can be described as a product of an electronic wave function, depending only on the electron coordinate  $\vec{r}$ , and a vibrational wave function, which is just the wave function of a simple harmonic oscillator centered at  $Q_0$ , depending only on the configuration coordinate  $Q$ :

$$\Psi_{i,n}(\vec{r}, Q) = \psi_i(\vec{r})\varphi_n(Q - Q_0) \quad (2.7)$$

From equations 2.6 and 2.7 the following matrix element can be obtained:

$$M_{12} \propto \int \int \psi_2^*(\vec{r})\varphi_{n_2}^*(Q - Q'_0)x\psi_1(\vec{r})\varphi_{n_1}(Q - Q_0)d^3\vec{r}dQ, \quad (2.8)$$

considering the light is polarized along the  $x$ -axis. The matrix element can be separated into two parts:

$$M_{12} \propto \int \psi_2^*(\vec{r})x\psi_1(\vec{r})d^3\vec{r} \cdot \int \varphi_{n_2}^*(Q - Q'_0)\varphi_{n_1}(Q - Q_0)dQ, \quad (2.9)$$

as long as the first term of equation 2.9 is independent of the position of the nuclei. This first term is the electric dipole moment for the electronic transition (orbital selection rule). The second term depends on the overlap of the initial and final vibrational wave functions and shows in form of equation 2.10 (related to Fermi's golden rule) the intensity of a specific vibronic transition:

$$I_{n_1, n_2} \propto \left| \int_0^\infty \varphi_{n_2}^*(Q - Q'_0) \varphi_{n_1}(Q - Q_0) dQ \right|^2 \quad (2.10)$$

This is the so called Franck-Condon factor. In other words, the most likely transition is one that changes the vibrational wave function least. In case of harmonic oscillators, which are considered here, wave functions peak at the edge of the potential well with increasing  $n$ . This means, the wave functions match best if the edge of the classical potential well of a specific level is near  $Q_0$ . The Franck-Condon factor of these transitions is largest.



# Chapter 3

## Experimental techniques: theory and setup

### 3.1 Theory of ellipsometry

By spectroscopic ellipsometry the change of polarization of a light beam through a reflection upon the boundary of two (or more) media with different refractive indices is investigated [8, 42, 56]. The acknowledgment of the absolute phases and amplitudes is not necessary - this optical technique is self-normalizing, which makes the measurement independent of possible fluctuations of the light source. Due to the interaction of the light with the sample, spectroscopic ellipsometry can be applied to determine optical properties of solids like the complex refractive index or the complex dielectric function, respectively, as well as layer thicknesses and electronic properties like band-to-band transitions. (By conventional ellipsometry e.g. the diagonal tensor element  $\epsilon_{xx}$  in case of unmagnetised isotropic media can be figured out.) The real and the imaginary part of the dielectric function ( $n$  and  $\kappa$  respectively) can be identified simultaneously for a bulk system with no need to use the Kramers-Kronig relations.

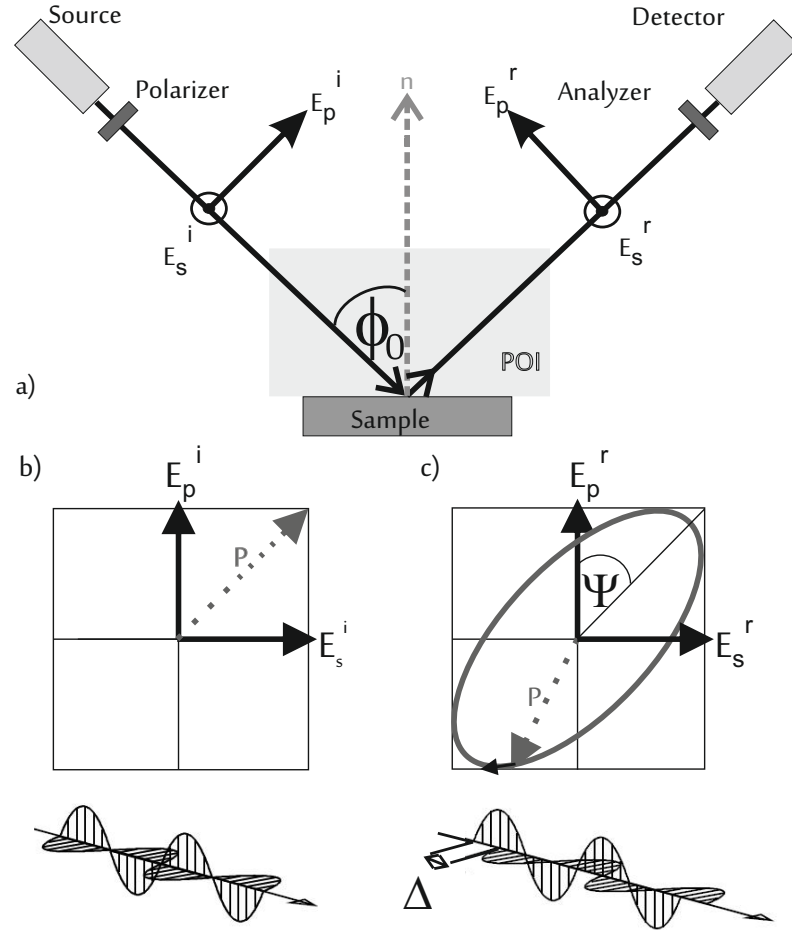


**Figure 3.1:** (a) Depicted is a simplified spectroscopic ellipsometry setup consisting of a light source, a polarizer producing linearly polarized light before the sample is irradiated under an angle  $\phi_0$  with the surface normal ( $n$ ), an analyzer and a detector measuring the intensity of the directly reflected light in dependence of the analyzer angle. Spectroscopic ellipsometry determines the parameters  $\Psi$  and  $\Delta$  in a specific spectral range in dependence of the wavelength of the incident light. For simplification the polarization states of the electrical field  $E$  are decomposed into 'p-polarized' (parallel to the plane of incidence (POI), which is defined by the directions of the incident and reflected light) and 's-polarized' (perpendicular to the POI). The indices  $i$  and  $r$  refer to the incoming and reflected light. (b) and (c) depict an example (identical absolute value of the electrical field components) of the polarization states of the incoming (linearly polarized) and reflected (elliptically polarized) light, with  $\Delta = \delta_p - \delta_s$ , being the phase shift difference of the s and p component of the electrical field,  $\tan \Psi = \frac{|r_p|}{|r_s|}$ , which refers to the relative change of amplitude of the two components upon reflection, and  $P$  indicating the resulting polarization direction (adapted from [64]).

The change of the electrical field of a monochromatic light beam after being reflected by a sample can be presented by complex reflection coefficients (equations 3.2), describing the relation of amplitude and phase of a specific linear polarization component of the electrical field of the incoming and reflected light. Due to the fact that any polarization state can be completely described by a superposition of two orthogonal electrical field components with linear polarization and their specific phases, the electrical field of the incoming and reflected light may be decomposed into components with a polarization parallel and perpendicular to the plane of incidence (POI)(see figure 3.1). In the following, a basic example of how to determine optical parameters by spectroscopic ellipsometry is given for a simple bulk system [8, 42, 56]. Assuming that the sample is isotropic, homogeneous, not magnetic (magnetic permeability  $\mu_1 = 1$ ), much thicker than the penetration depth of the light with a vanishing surface charge  $\vec{\rho}$  and current  $\vec{j}$  and surrounded by air ( $\mu_0 = 1; N_0 = 1$ ), the complex reflection coefficients can be substituted by the Fresnel coefficients. Deduced from the Maxwell equations with appropriate continuity conditions for the amplitude of the electromagnetic wave at the boundary between two dielectrics, the Fresnel coefficients for the parallel and perpendicular polarization components can be obtained [14]:

$$\begin{aligned} r_p &= \frac{E_p^r}{E_p^i} = \frac{N_1 \cos \phi_0 - N_0 \cos \phi_1}{N_1 \cos \phi_0 + N_0 \cos \phi_1} \\ r_s &= \frac{E_s^r}{E_s^i} = \frac{N_0 \cos \phi_0 - N_1 \cos \phi_1}{N_0 \cos \phi_0 + N_1 \cos \phi_1}. \end{aligned} \quad (3.1)$$

Presented are only the Fresnel coefficients concerning the reflection (not the transmission), with the indices i, r, p and s of the incident, reflected, parallel and perpendicular to the POI polarized electrical field components.  $N_1$  and  $N_0$  denote the complex refractive indices of the sample (subscript 1) and the surrounding medium (subscript 0) while  $\phi_1$  and  $\phi_0$  refer to the angles of the light beam with respect to the surface normal inside and outside of the sample. The complex reflection coefficients  $r_p$  and  $r_s$  can also be written in dependence of the phases  $\varphi$  of the incoming and reflected electrical field components as well as in dependence of their phase shift  $\delta$ :

$$\begin{aligned}
r_p &= \frac{|E_p^r|}{|E_p^i|} e^{i(\varphi_p^r - \varphi_p^i)} = |r_p| e^{i\delta_p} \\
r_s &= \frac{|E_s^r|}{|E_s^i|} e^{i(\varphi_s^r - \varphi_s^i)} = |r_s| e^{i\delta_s}.
\end{aligned} \tag{3.2}$$

The ratio of the complex reflection coefficients,  $r_p$  over  $r_s$ , can be connected with the parameters  $\Psi$  and  $\Delta$  [7], which are obtained through the ellipsometric measurement:

$$\frac{r_p}{r_s} = \frac{|r_p| e^{i\delta_p}}{|r_s| e^{i\delta_s}} = \frac{|r_p|}{|r_s|} e^{i(\delta_p - \delta_s)} = \tan \Psi e^{i\Delta} = \rho \tag{3.3}$$

with  $\rho$ , the complex reflectance ratio,  $\Delta = \delta_p - \delta_s$ , the phase shift difference of the s and p component of the electrical field, and  $\tan \Psi = \frac{|r_p|}{|r_s|}$ , which refers to the relative change of amplitude of the two components upon reflection (cf. figure 3.1b) and c)). Replacing  $r_p$  and  $r_s$  in equation 3.3 by the equations in 3.1 and using Snell's law [14]:

$$N_0 \sin \phi_0 = N_1 \sin \phi_1 \tag{3.4}$$

to replace  $\phi_1$  with a function dependent on  $\phi_0$ ,  $N_0$  and  $N_1$  leads to

$$N_1 = N_0 \tan \phi_0 \left[ 1 - \frac{4\rho}{(1 + \rho)^2} \sin^2 \phi_0 \right]^{1/2}, \tag{3.5}$$

the complex refractive index  $N_1$  of the sample in dependence of  $\rho$  containing  $\Psi$  and  $\Delta$  (see equation 3.3). In the more general case of more complex samples (e.g. layered or relatively thin samples, rough interfaces), a theoretical model has to be developed to determine the optical properties of the sample as they can not be calculated analytically.

## 3.2 Setup of ellipsometry

Ellipsometric data presented within this thesis were performed on a SENTECH SE 850 spectral ellipsometer in combination with two light sources, a Xe-discharge lamp (220 nm to 790 nm) and a halogen lamp (790 nm to 2600 nm) under clean room conditions ( $T = 22^\circ\text{C} \pm 0.5^\circ\text{C}$ , humidity:  $40\% \pm 3\%$ ).

## 3.3 Theory of Raman scattering

Raman spectroscopy in general can be applied to examine a sample of interest with regard to composition, orientation, restraint, temperature, structure and further material properties. The frequency shift (Raman shift) of the incident laser light and the inelastically scattered light is measured, whereupon the corresponding energy difference relates to a specific excitation of the sample of e.g. electronic, vibrational or magnetic origin. In a Raman experiment these diverse excitations as well as their potential coupling can be measured at once - qualifying this method especially to investigate strongly correlated systems.

Several approaches to describe Raman scattering mathematically can be found [23, 25, 30, 51] and are either useful to explain it in an appealing manner or necessary to understand the physical process as e.g. the quantum-mechanical description in the special case of resonant Raman scattering. For this reason, different derivations are combined in the following introduction. A simple access to Raman scattering can be obtained from the classical view with scalar quantities [25, 30]. The electrical polarizability  $\alpha$  of a sample is not necessarily constant in time during the illumination with light represented by its electric field  $E(t) = E_0 \cos \omega t$ . Excited quasiparticles can modulate the polarizability - as e.g. phonons through their oscillations estimated as harmonic oscillators with a phonon amplitude  $Q(t) = Q_0 \cos \Omega t$  here. Due to their small impact on the polarizability,  $\alpha$  can be developed into a Taylor series:

$$\alpha(Q) = \alpha_0 + \left(\frac{\partial \alpha}{\partial Q}\right)_0 Q + \dots, \quad (3.6)$$

which with

$$\cos(x) \cdot \cos(y) = \frac{1}{2}(\cos(x - y) + \cos(x + y)) \quad (3.7)$$

results in an induced dipole moment:

$$\begin{aligned} p &= \alpha E = (\alpha_0 + (\frac{\partial \alpha}{\partial Q})_0 Q + \dots) E_0 \cos(\omega t) = \\ &\alpha_0 E_0 \cos(\omega t) + (\frac{\partial \alpha}{\partial Q})_0 Q_0 \cos(\Omega t) \cdot E_0 \cos(\omega t) + \dots = \\ &\underbrace{\alpha_0 E_0 \cos(\omega t)}_{\text{Rayleigh}} + \underbrace{\frac{1}{2} (\frac{\partial \alpha}{\partial Q})_0 E_0 Q_0 \cos((\omega - \Omega)t)}_{\text{Stokes}} + \underbrace{\frac{1}{2} (\frac{\partial \alpha}{\partial Q})_0 E_0 Q_0 \cos((\omega + \Omega)t)}_{\text{Anti-Stokes}} \dots \end{aligned} \quad (3.8)$$

Neglecting higher order terms, equation 3.8 shows three terms, which can be assigned to the non frequency shifted elastically scattered light (Rayleigh) and the inelastically Raman scattered light towards lower (Stokes) or higher (Anti-Stokes) frequencies respectively (see also figure 3.2). These sidebands are associated with specific quasiparticles of the sample and lead to the selection rules

$$\begin{aligned} \omega &= \omega' \pm \Omega \\ \vec{k} &= \vec{k}' \pm \vec{K} \end{aligned} \quad (3.9)$$

for energy and momentum conservation with  $\omega'$  and  $\vec{k}'$  the frequency and momentum of the scattered light and  $\vec{k}$  and  $\vec{K}$  the momentum of the incoming light and the quasiparticle respectively. In the more general case the polarizability  $\alpha$  is substituted by the susceptibility tensor  $\chi_{jl}$  [30]:

$$\chi_{jl} = (\chi_{jl})_0 + \sum_k (\frac{\partial \chi_{jl}}{\partial Q_k})_0 Q_k + \sum_{k,m} (\frac{\partial^2 \chi_{jl}}{\partial Q_k \partial Q_m})_0 Q_k Q_m + \dots \quad (3.10)$$

with the indices  $j$  and  $l$  from 1-3 each and  $k$  representing all optical modes and the normal coordinate  $Q_k$  of a specific mode. Every mode can now be related to a specific  $3 \times 3$  matrix  $\frac{\partial \chi_{jl}}{\partial Q_k}$ . Similarly, each crystal space group can be fractionized by factor group methods into its basis of irreducible representations, which are eponymous for the corresponding modes deduced above,

as symmetries characterize the crystal space groups and their possible oscillations likewise. A universal derivation of the number and symmetries of all possible modes in all crystal space groups is calculated by means of group theory. So called character tables represent the results [30].

Group theory calculations also give information which of these predicted modes are Raman active, id est fulfill the selection rules for a Raman process. A comparable but more intuitive description of this selection rule is obtained by looking again at the polarizability  $\alpha$ . Equation 3.8 depicts the necessity of  $(\frac{\partial\alpha}{\partial Q})_0 \neq 0$  during a scattering process to receive Raman sidebands. Figure 3.2 shows exemplarily a symmetrical and an asymmetrical stretching mode of a molecule with inversion center. In these kinds of molecules vibrational modes are either Raman active or infrared active, as all oscillations anti-symmetric to the inversion center are Raman forbidden and all oscillations symmetric to the inversion center are not infrared active. Oscillations creating a dipole moment  $p$  however can lead to infrared absorption. This rule of mutual exclusion also holds for centrosymmetric crystals, which were investigated within this work exclusively.

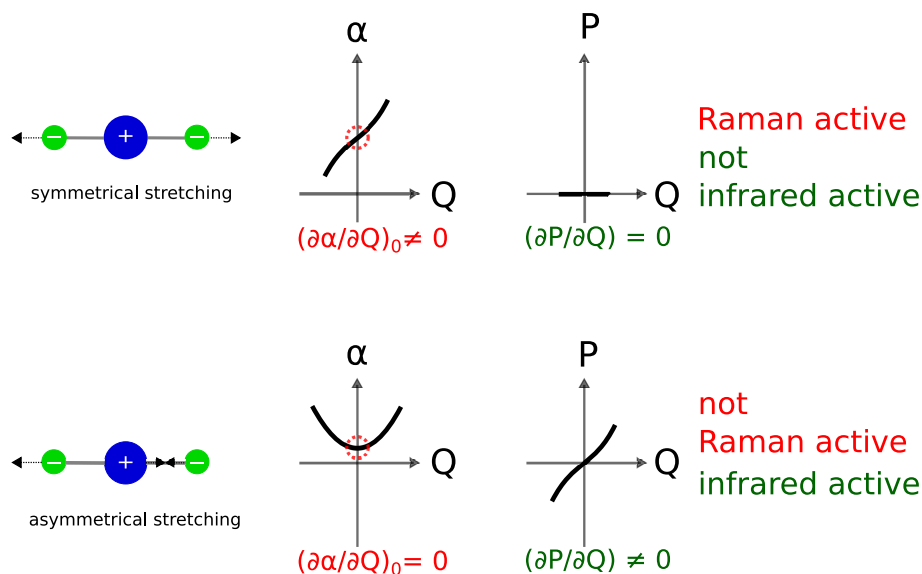


**Figure 3.2:** To illustrate the mutual exclusion of Raman and infrared active modes in a molecule with inversion center a symmetrical stretching mode (upper row) and an asymmetrical stretching mode (lower row) together with their corresponding developments of the polarizability  $\alpha$  and the dipole moment  $p$  with the normal coordinate  $Q$  are shown exemplarily.

Furthermore, a vibrational mode can only be observed in the Raman spec-

trum if proper experimental conditions are chosen. The polarizations of the incoming and scattered light are described by the polarization unit vectors  $e_i$  and  $e_s$ , respectively, and determine the geometry of the measurement and select the measurable symmetries by probing different components of the Raman tensor  $\frac{\partial \chi_{jl}}{\partial Q_k}$  (see equation 3.10). This way no quantitative information about scattering intensities can be obtained, but a qualitative statement about the scattering intensities in the different scattering geometries will be received through the Raman tensor in combination with the polarization selection rules. Neither mode assignment can be done through group theoretical calculations. Therefore, lattice dynamics calculations have to be involved. A predication of the Raman intensity can be done by using the double differential Stokes Raman scattering cross section from a crystalline solid [51]:

$$\frac{d^2\sigma}{d\Omega d\omega_s} \propto \left(\frac{\omega_s}{c}\right)^4 (n(\omega) + 1) \text{Im} [R(\omega + i\delta)] V_{eff} \quad (3.11)$$

with  $\omega_s$  the frequency of the scattered photon,  $c$  the speed of light,  $n(\omega)$  the Bose-Einstein statistical factor,  $R(\omega)$  the response function,  $V_{eff}$  the effective sample volume (cf. section 3.5). Equation 3.11 shows different factors that influence the double differential Stokes Raman scattering cross section.

As can be seen by the Fourier transform  $R(t - t')$  of the response function  $R(\omega)$  the interaction Hamiltonian of the light with the electrons  $H'$ , which is explained later in this section in more detail, is incorporated as follows

$$R(t - t') = \langle \Psi | T H'(t') H^\dagger(t) | \Psi \rangle, \quad (3.12)$$

with  $T$  the time-ordering operator and  $|\Psi\rangle$  the ground state [51]. Raman spectra also have to be Bose-corrected due to the retarded nature of the response function (see equation 3.11). In general, an applied perturbation can dissipate energy to a system caused by a specific process that finally ends up as heat. The other way round, the present heat of the system can trigger fluctuations (related to the specific process mentioned above) that, themselves, influence the response of the system to the perturbation. These fluctuations can be quantitatively connected to the dissipation (the response of the system respectively) by the fluctuation-dissipation theorem originated by statistical thermodynamics. In the case of Raman scattering, the fluctuation-dissipation theorem leads to a relation between the differential scattering cross section and the retarded Raman response function, which results in the Bose-correction factor  $n(\omega) + 1 = (1 - e^{-\beta\hbar\omega})^{-1}$  (in case of

Stokes scattering) [51].

Raman shifts are usually presented in wave numbers  $\tilde{\nu}$  defined as the inverse of the wavelength  $\tilde{\nu} = \frac{1}{\lambda}$  with the conversion formula in commonly used units

$$\tilde{\nu}(cm^{-1}) = \frac{10^7}{\lambda(nm)}. \quad (3.13)$$

Another often applied unit is electron volts (eV) with

$$1 \text{ eV} \hat{=} 1000 \text{ meV} \hat{=} 1240 \text{ nm} \hat{=} 8065.6 \text{ cm}^{-1} \quad (3.14)$$

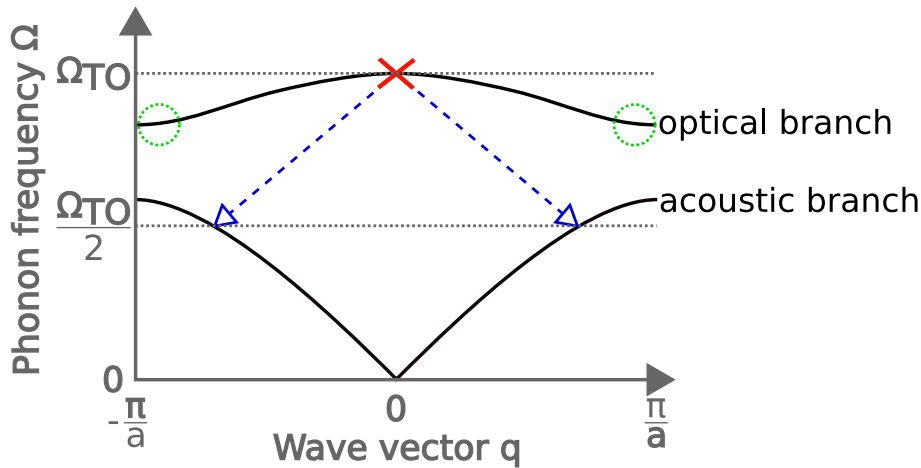


**Figure 3.3:** First-order Raman scattering is classified into a simple phonon dispersion curve near the Brillouin zone center ( $\Gamma$ -point) (red cross). This excited optical phonon can decay into two acoustic phonons (blue arrows). Green circles illustrate a favored combination for a two-phonon Raman scattering process.

When using an excitation source in the visible spectral region, only optical phonons near the Brillouin zone center ( $\Gamma$ -point) (red cross in figure 3.3) can be excited in first-order Raman scattering due to the comparatively large wavelength of the light in comparison to the lattice constant, as momentum conservation must be fulfilled. Two-phonon processes, however, are possible e.g. (see also equation 3.10) if momentum conservation is fulfilled by  $q_1 + q_2 = 0$ . Green circles in figure 3.3 show a favored two-phonon combination, as excitations at these points of the optical branch in the phonon dispersion show enhanced probability due to the higher density of states here (group velocity = 0). As a consequence of anharmonic potential wells, short lifetimes of optical phonons result coming along with e.g. three-phonon

processes depicted by blue arrows in figure 3.3 showing the annihilation of one phonon and involving the creation of two new ones. Such a process is an example of how the lifetime, damping and line width, respectively, of a spectral mode might be influenced. Different origins of interactions (e.g. phonon-phonon or electron-phonon) of the phonon modes in the crystal result in diverse line shapes. The Lorentzian line shape e.g. is describing the natural line width, while the Fano profile is involving correlations between phonons and excitations of electronic origin [6].

### 3.4 Theory of resonance Raman scattering

To establish an understanding of resonance Raman scattering, a quantum-mechanical description has to be taken into account. Therefore, light coupled to a scattering medium may be presented by the Hamiltonian

$$H = H_0 + H' + H'' \quad (3.15)$$

with the Hamiltonians  $H_0$  for the unperturbed scattering medium,  $H'$  for the coupling of the photons to the electrons and  $H''$  for the electron-lattice interaction, or in the more general case, the coupling between the different excitations in the scattering medium respectively. The undisturbed Hamiltonian [31]

$$H_0 = \frac{\vec{p}^2}{2m_0} + V(\vec{r}) \quad (3.16)$$

with  $V(\vec{r})$  the potential energy of an electron in the atom can be modified by

$$\vec{p} \rightarrow (\vec{p} + e\vec{A}). \quad (3.17)$$

This way the perturbation of light to the system is involved by the impact of the electromagnetic field via its vector potential  $\vec{A}$  on the charge  $-e$  of an electron as it changes the momentum  $\vec{p}$  of the electron like 3.17, which is known from classical electromagnetism. From this follows

$$H_0 + H' = \frac{1}{2}m_0(\vec{p} + e\vec{A})^2 + V(\vec{r}) = H_0 + \frac{e}{2m_0}(\vec{p} \cdot \vec{A} + \vec{A} \cdot \vec{p}) + \frac{e^2\vec{A}^2}{2m_0}. \quad (3.18)$$

The possible reduction of the resulting interaction Hamiltonian  $H'$  of 3.18 to

$$H' = \frac{e}{m_0}\vec{p} \cdot \vec{A} \quad (3.19)$$

as in the Coulomb gauge  $\nabla \cdot \vec{A} = 0$  the operators  $\vec{p}$  and  $\vec{A}$  commute and  $\vec{A}^2$  is disregarded due to its marginal impact on  $H'$  compared to  $\vec{p} \cdot \vec{A}$  is continued by further modifications. With

$$\vec{A}(\vec{r}, t) = \vec{A}_0 \exp i(\vec{k} \cdot \vec{r} - \omega t) \quad (3.20)$$

and  $\vec{A}_0$  pointing along  $\vec{\mathcal{E}}_0$  (electric field of the light wave) as well as  $e^{i\vec{k}\vec{r}}$  developed into a Taylor expansion

$$e^{i\vec{k}\vec{r}} = 1 + i\vec{k} \cdot \vec{r} + \frac{1}{2}(i\vec{k} \cdot \vec{r})^2 + \dots \approx 1 \quad (3.21)$$

that may be terminated behind the first term of 3.21 (electric dipole approximation) because of the insignificance of  $|\vec{k} \cdot \vec{r}|$  due to the larger dimension of light at optical frequencies to the average atomic scale and the approximation

$$\vec{\mathcal{E}}_0 = i\omega\vec{A}_0 \quad (3.22)$$

$H'$  turns into

$$H' = -\vec{p}_e \cdot \vec{\mathcal{E}}_0. \quad (3.23)$$

Equation 3.23 corresponds to the interaction Hamiltonian of a dipole in an electric field as

$$\vec{p}_e = -e\vec{r} \quad (3.24)$$

describes the electric dipole moment of the electron giving reason for calling the above deduced approximation electric dipole approximation.

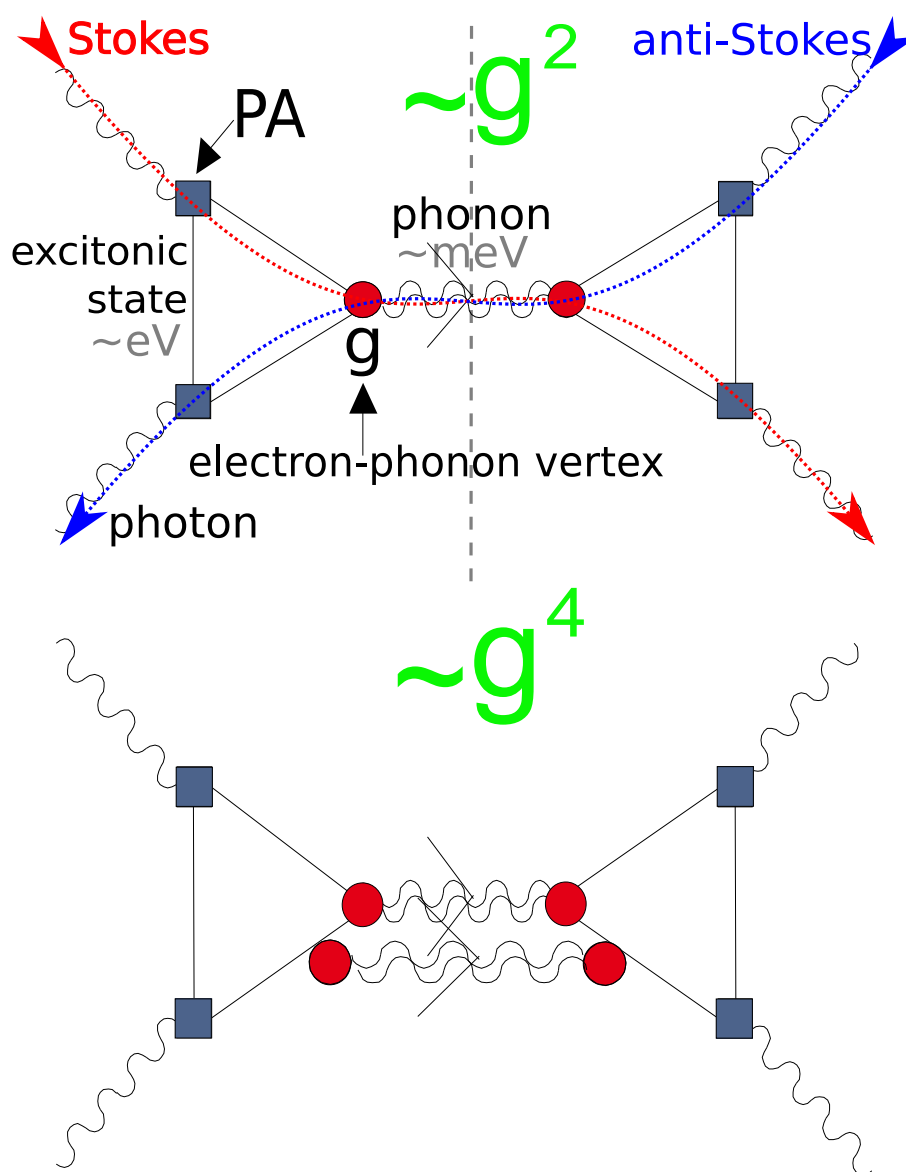


**Figure 3.4:** Raman scattering process based on a four-photon Green's function as derived by Kawabata [21, 22], visualized with the help of Feynman diagrams. A more detailed description of the one-phonon Raman process (upper diagram) and the two-phonon Raman process (lower diagram) is found in the text below. Additionally, in the upper Feynman diagram symbolic anti-Stokes (blue shifted) and symbolic Stokes (red shifted) processes are shown by the dashed blue and red lines respectively. The photon-electron interaction vertices (blue squares) indicate the  $I \propto \omega^4$  proportionality of the Raman scattering intensity resulting from the dipole approximation.

Arisato Kawabata [21, 22] developed a microscopic theory of Raman scattering based on a four-photon Green's function, which can be visualized with the help of Feynman diagrams, as figure 3.4 shows. Likewise, the following derivation within third-order time-dependent perturbation theory can be illustrated by Feynman diagrams. The upper Feynman diagram in figure 3.4 depicts the transition rate of a one-phonon Raman scattering process described in equation 3.26 [23]. Each step of the Raman scattering process is related to a mathematical term in equation 3.25 [23] and is documented in the way along the interaction vertices (blue squares for the photon-electron interaction vertices and red dots for the electron-phonon vertices respectively) in the Feynman diagram. Literature often operates with half a Feynman diagram, which is also done here in the following. For symmetry reasons only the left half of the Feynman diagram is discussed (see separating line in the upper Feynman diagram in figure 3.4) in equation 3.25.

The incoming light couples to an excitonic state of a typical order of magnitude of several electronvolts (eV). This photon-electron interaction is represented by the Hamiltonian  $H'$  describing in combination with the initial state  $|i\rangle$  and a first intermediate state  $|\alpha\rangle$  and the corresponding term in the denominator  $[\hbar\omega_i - (E_\alpha - E_i)]$  in equation 3.25 the initial step of the Raman scattering process.  $E_i$  and  $E_\alpha$  represent the energy of the initial and first intermediate state respectively and  $\hbar\omega_i$  the photon energy of the incident light. The created electron-hole pair can develop into, for example, a one-phonon process (which is in the order of magnitude of meV), as taken into account here and introduced in equation 3.25 by the term  $\langle\beta|H''|\alpha\rangle$  and its corresponding denominator.  $H''$  is the Hamiltonian for the electron-lattice interaction containing the electron-phonon coupling constant  $g$ ,  $\beta$  a further intermediate state with energy  $E_\beta$  and  $\hbar\omega_0$  the phonon energy. Finally, the electron recombines from the  $|\beta\rangle$  to the  $|i\rangle$  state by emitting a photon (compare remaining terms in equation 3.25).

$$\sum_{\alpha,\beta} \frac{\langle i | H' | \beta \rangle \langle \beta | H'' | \alpha \rangle \langle \alpha | H' | i \rangle}{a \cdot b \cdot c}$$

with the following substitutions:

(3.25)

$$a = [\hbar\omega_i - (E_\alpha - E_i)]$$

$$b = [\hbar\omega_i - (E_\alpha - E_i) - \hbar\omega_0 - (E_\beta - E_\alpha)]$$

$$c = [\hbar\omega_i - (E_\alpha - E_i) - \hbar\omega_0 - (E_\beta - E_\alpha) - \hbar\omega_f - (E_f - E_\beta)]$$

Simplifying the denominator and ensuring energy conservation (with  $E_f - E_i = 0$ ) equation 3.25 results in the formula for the transition rate in

$$P = \frac{2\pi}{\hbar} \left| \sum_{\alpha, \beta} \frac{\langle i | H' | \beta \rangle \langle \beta | H'' | \alpha \rangle \langle \alpha | H' | i \rangle}{[\hbar\omega_i - (E_\alpha - E_i)][\hbar\omega_i - \hbar\omega_0 - (E_\beta - E_i)]} \right|^2 \delta[\hbar\omega_i - \hbar\omega_f - \hbar\omega_0] \quad (3.26)$$

Another scenario could be the electron-hole pair developing into a two-phonon process, as depicted in the lower Feynman diagram in fig. 3.4. Whereas the one-phonon process is proportional to  $g^2$ , the two-phonon process is proportional to  $g^4$  influencing the relative intensities of the one- and two-phonon modes in the Raman spectra as can be estimated by the following simple numerical example. A  $g$  of size  $10^{-1}$  would lead to a proportionality factor  $g^2 = 10^{-2}$  for the one-phonon process and to a proportionality factor  $g^4 = 10^{-4}$  for the two-phonon process demonstrating the enhanced probability of the one-phonon process. Manuel Cardona and his group have measured the one- and two-phonon spectra of silicon with different laser excitation energies and have compared the one- and two-phonon resonance profiles [48] (figure 3.5a-c). Though the behavior of the two-phonon modes varies with excitation wavelength, it can be gathered from figure 3.5b) and c) that the one- and two-phonon mode resonances, respectively, show identical profiles, which is of interest with regard to the interpretation of the results of the LaMnO<sub>3</sub> study within this thesis. Furthermore, from these resonance profiles information about the electron-phonon coupling and information about the coupling strength of the phonons to the intermediate electronic states can be obtained.

While in the conventional Raman scattering process the frequency dependence of the intensity is determined by the  $\omega^4$ -factor, in the resonance Raman scattering process other effects become dominating. If either the incoming or the scattered light coincides with a real excitonic state, the respective states in the summation over all intermediate states get into focus and lead to the special case of resonance Raman scattering with clearly enhanced Raman intensities (up to a factor of  $\sim 10^6$ ), as can already be deduced from the denominator in equation 3.26. Alternatively, the resonance Raman scattering process can be explained by the above deduced  $\vec{p} \cdot \vec{A}$  term, which can become resonant. The real excitonic state, dominantly taken into account within the resonance Raman scattering process, can be excited into its specific vibronic states via the Franck-Condon process (cf. section 2.3). The excitation of one phonon within this process is proportional to the electron-phonon coupling

constant  $g$  - instead of  $g^2$  in comparison to the conventional Raman scattering process. This results in an enhancement of the phonons connected to the selected excitonic state, and also the corresponding overtones arise with stronger intensities in the spectrum, as these one- or multiphonons can be excited in one step only dependent on the magnitude of the Franck-Condon overlap factors connecting the intermediate and final states [66].

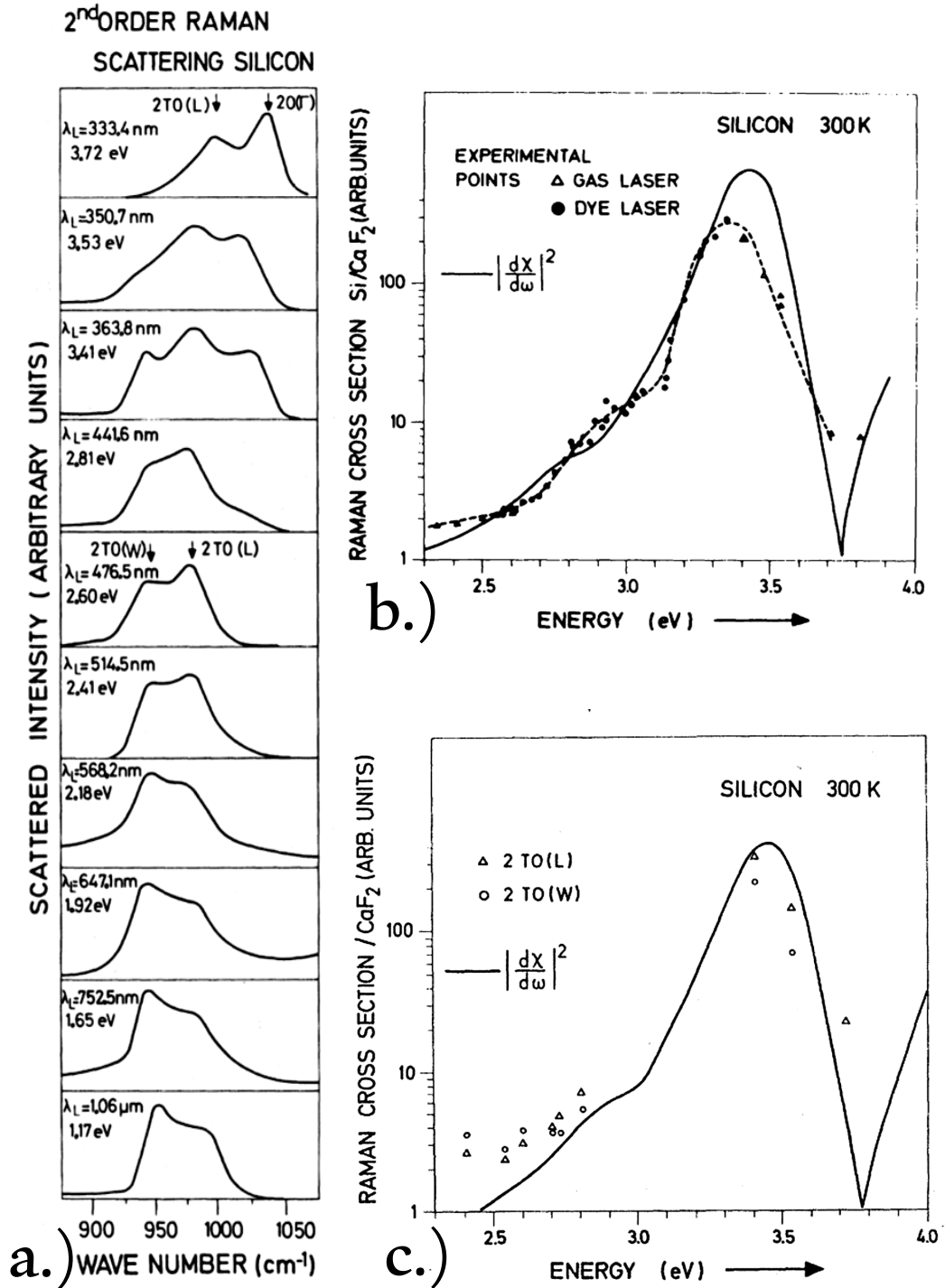


Figure 3.5: a.) Second-order phonon spectra of silicon measured by Manuel Cardona and his group [48] in dependence of the excitation laser wavelengths. b.) and c.) show the resonance profiles of the first- and second-order phonon modes of silicon respectively. The Raman cross section is depicted in dependence of the laser excitation energy in electron volts (eV).

### 3.5 Effective sample volume

The Raman intensity is dependent on the scattering volume. This volume depends on the refractive indices and absorption coefficients of the sample and on the limiting collecting angle of the objective. While the limiting collecting angle of the reflective objective  $\theta_{obj} = 26.56^\circ$  is constant for the UT-3, the complex refractive index of the sample may vary with changing experimental conditions like e.g. different excitation energies, geometrical setups and sample temperatures. In the following, these effects are described in detail [32, 45, 55, 56] and are summarized in the effective sample volume correction making the Raman spectra comparable under varying experimental conditions.

The intensity of the incident laser light as well as the intensity of the scattered light is reduced due to reflections at the sample surface. The amount of light that enters the sample at the sample surface  $(1 - R(\omega_i))$  as well as the amount of the scattered light leaving the sample at the sample surface  $(1 - R(\omega_s))$  depends on the reflection coefficient

$$R(\omega) = \frac{n'(\omega)^2 + k'(\omega)^2 + 1 - 2n'(\omega)}{n'(\omega)^2 + k'(\omega)^2 + 1 + 2n'(\omega)}, \quad (3.27)$$

with  $n'(\omega)$ , the refractive index and  $k'(\omega)$ , the absorption coefficient of the sample. In case of a small difference of the frequency of the incident light ( $\omega_i$ ) and the scattered light ( $\omega_s$ ) (small Raman shift) and/or low variation of  $R(\omega)$ , the approximation  $R(\omega_i) \approx R(\omega_s)$  results in the simplified correction factor  $[1 - R(\omega_i)]^2$ . The two factors may be combined, as in backscattering geometry  $R(\omega)$  is identical inside and outside of the sample.

Another effect results from the varying penetration depth

$$\beta(\omega_{i,s}) = \frac{c}{2\omega_{i,s}k'(\omega_{i,s})} \quad (3.28)$$

of the light involved in the Raman process. In case of a quasi-backscattering setup,  $d_1$ , the distance the incident photon propagates inside of the sample up to the point of the Raman process (probability:  $f_{12}$ ), can be set equal to  $d_2$ , the distance the scattered photon propagates back to the sample surface. The probability to observe a scattered photon at the sample surface is then

$$P = \int \exp\left(\frac{-d_1}{\beta(\omega_i)}\right) \cdot f_{12} \cdot \exp\left(\frac{-d_2}{\beta(\omega_s)}\right) dd_1 = f_{12} \cdot \frac{\beta(\omega_i)\beta(\omega_s)}{\beta(\omega_i) + \beta(\omega_s)} \stackrel{!}{=} f_{12} \cdot \tilde{\beta} \quad (3.29)$$

with

$$\exp\left(\frac{-d}{\beta(\omega)}\right) \quad (3.30)$$

the probability of a photon propagating a distance  $d$  within the sample (in case  $\beta(\omega) \ll$  geometrical depth of the image of the objective). Only first-order scattering processes have been taken into account as in comparison the probability of higher order scattering processes is small [45]. To correct Raman spectra with small Raman shifts and a smooth function of  $k'(\omega)$ , the approximation  $\beta(\omega_i) \approx \beta(\omega_s)$  is acceptable.

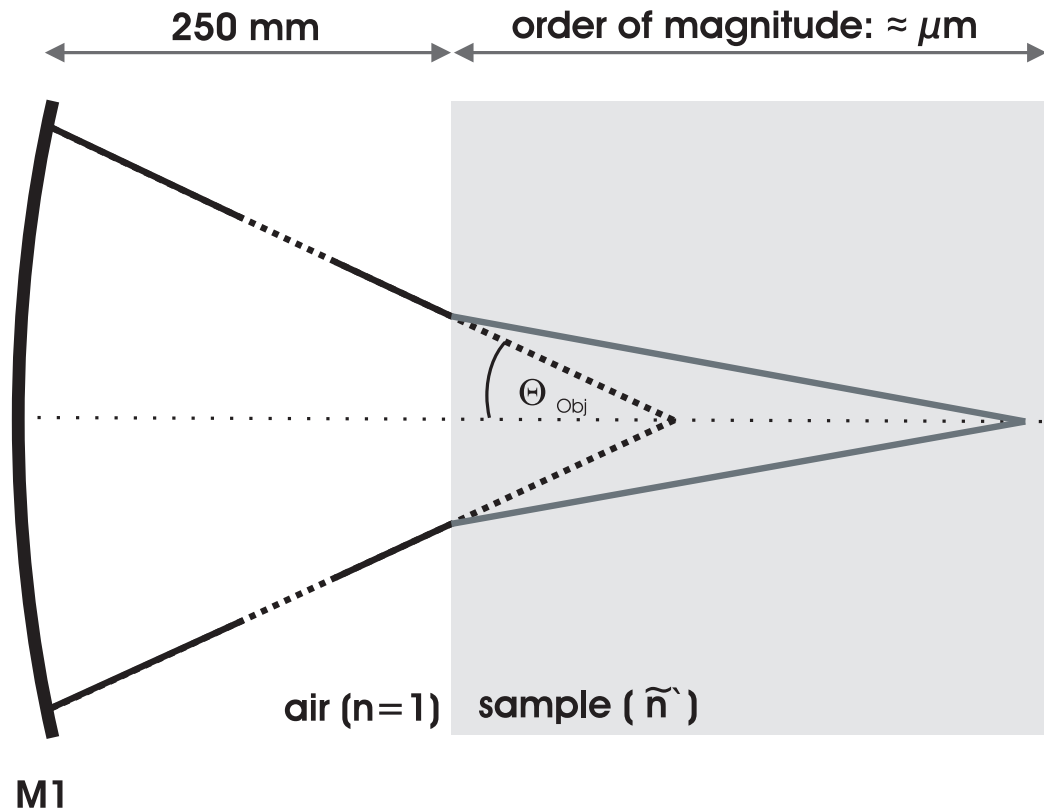


**Figure 3.6:** Possible paths of the incident and detectable Raman scattered light lying within the cones depicted with solid lines. The cone inside the sample is defined by the limiting collecting angle  $\theta_{obj}$  of the mirror M1 and the complex refractive index  $\tilde{n}'$  of the sample. The interruptions of the solid lines outside the sample by dotted lines indicate a break in the order of magnitude of this depiction in respective area.

Furthermore, only a fraction of the Raman intensity can be detected by the

entrance optics of the UT-3 as it is scattered into all directions. Figure 3.6 depicts the path of the incident light and analogously the detectable directions of the scattered light lying within the cone that is defined by the limiting angle  $\theta_{Obj}$  and the complex refractive index of the sample as will be explained in the following. The cone can be described by its solid angle. The solid angle in general is defined by  $\Omega = \frac{A}{R^2}$  with A a surface area of a spherical cap (without the area of the base) and R the radius of a sphere. Thus, the solid angle here can be set proportional to  $\tan^2 \theta_{sam}$ . This approximation is valid in case of relatively small values of  $\theta_{sam}$ , which still apply to our case (cf. appendix A).

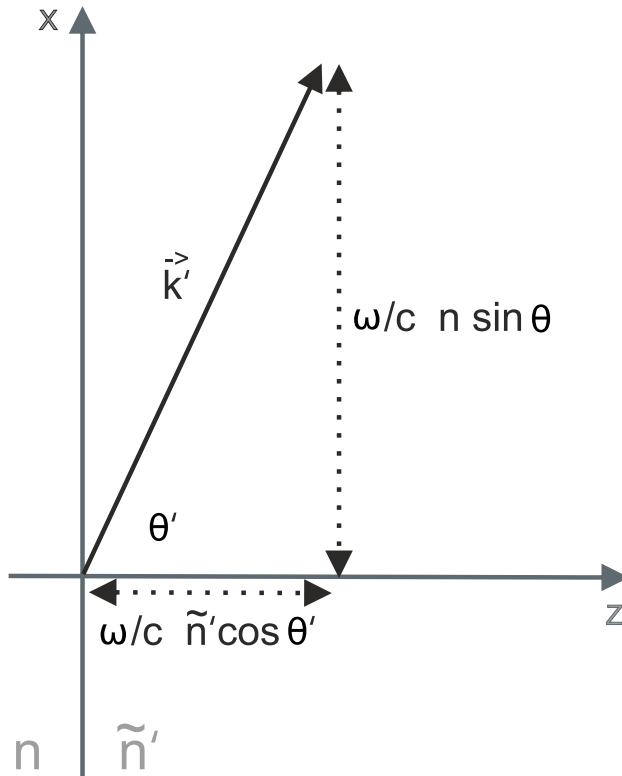


**Figure 3.7:** Depicted is the transmitted complex wavevector  $\vec{k}'$  from a non absorbing medium with refractive index  $n$  to a medium with a complex refractive index  $\tilde{n}'$ . The boundary surface is the  $xy$  plane and  $\theta$  the angle of incidence (not depicted here).

To obtain  $\theta_{sam}$ , a look at the transmitted complex wavevector  $\vec{k}'$  from a non-absorbing medium with refractive index  $n$  to a medium with a complex refractive index  $\tilde{n}'$  is useful [32]. The  $xz$  plane is defined as plane of incidence as depicted in figure 3.7. Due to continuity conditions at the boundary surface

(xy plane), the x-component of  $\vec{k}'$  remains unchanged and the transmitted complex wave vector can be written as

$$\vec{k}' = \frac{\omega}{c}(n \sin \theta, 0, \tilde{n}' \cos \theta'). \quad (3.31)$$

In this case  $\theta'$  has to be handled with care. As at least one medium is described with a complex refractive index with a non-negligible absorption coefficient,  $\theta'$  is not identical with the direction of the transmitted light. The definition of a plane wave within an absorbing medium must be reformulated, which is associated with a modification of the refraction law in absorbing media towards

$$n_T \sin \theta_{sam} = n \sin \theta, \quad (3.32)$$

containing the new definitions  $n_T$  and  $\theta_{sam}$  described in the following. Figure 3.7 shows that the z-component of  $\vec{k}'$  can be expressed in dependence on the incident angle  $\theta$ :

$$\tilde{n}' \cos \theta' = \sqrt{\tilde{n}'^2 - n^2 \sin^2 \theta} \equiv \eta e^{i\phi}, \quad (3.33)$$

with

$$\eta^2 \cos 2\phi = n'^2 - k'^2 - n^2 \sin^2 \theta \quad (3.34)$$

and

$$\eta^2 \sin 2\phi = 2n'k'. \quad (3.35)$$

The new expression of the transmitted wave vector

$$\vec{k}' = \frac{\omega}{c}[n \sin \theta, 0, (\eta \cos \phi + i\eta \sin \phi)], \quad (3.36)$$

set into the spatial part of the plane wave function  $\exp(-i\vec{k}' \cdot \vec{r})$ , delivers the planes of constant real phase in the absorbing medium leading to the definition of  $n_T$  that fulfills equation 3.32:

$$n_T \equiv \sqrt{n^2 \sin^2 \theta + \eta^2 \cos^2 \phi}. \quad (3.37)$$

In case of the UT-3 with air as surrounding medium the refraction index  $n = 1$  and  $\theta = \theta_{Obj}$ . With  $\cos^2 \phi = \frac{1+\cos 2\phi}{2}$  from equations 3.34, 3.35 and 3.37 can be concluded:

$$n_T^2 = \frac{1}{2} \left[ \sqrt{(n'^2 - k'^2 - \sin^2 \theta_{Obj})^2 + (2n'k')^2} + (n'^2 - k'^2 + \sin^2 \theta_{Obj}) \right]$$

$$n_T^2 = n'^2 + \frac{1}{2}(n'^2 + k'^2 - \sin^2 \theta_{Obj}) \left[ \sqrt{1 + \frac{4k'^2 \sin^2 \theta_{Obj}}{(n'^2 + k'^2 - \sin^2 \theta_{Obj})^2}} - 1 \right] \quad (3.38)$$

With equation 3.32

$$\theta_{sam} = \sin^{-1} \frac{\sin \theta_{Obj}}{n_T} \quad (3.39)$$

and thus

$$\tan^2 \theta_{sam} = \tan^2 \left( \sin^{-1} \frac{\sin \theta_{Obj}}{n_T} \right). \quad (3.40)$$

Equations 3.38 and 3.39 show that  $\theta_{sam}$  does not only depend on the incident angle, but also on the complex refraction index of the sample.

Finally, the Raman intensities have to be corrected for all the above mentioned effects summarized in the effective sample volume  $V_S(\omega_i)$  (with the approximation  $\omega_i \approx \omega_s$ ):

$$I_{cor} = \frac{I_{raw}}{V_S(\omega_i)}. \quad (3.41)$$

With all preceding approximations  $V_S(\omega_i)$  results in:

$$V_S(\omega_i) \propto [1 - R(\omega_i)]^2 \cdot \beta(\omega_i) \cdot \tan^2 \left( \sin^{-1} \frac{\sin \theta_{Obj}}{n_T} \right). \quad (3.42)$$

Due to the strong frequency dependence of equation 3.42, the effective sample volume correction is especially important for resonance Raman measurements.

### 3.6 Resonance Raman setup (UT-3)

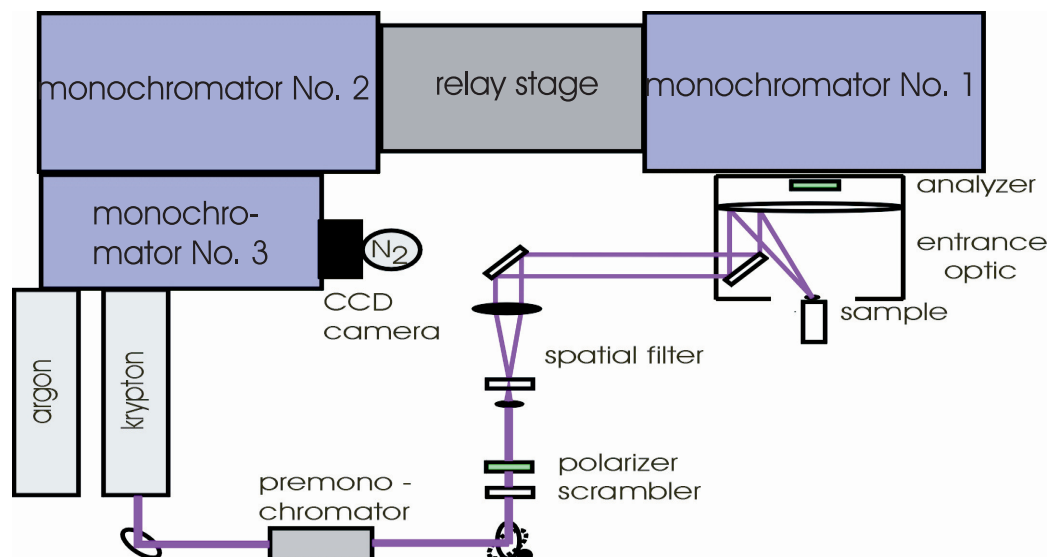


**Figure 3.8:** Scheme of the resonance Raman setup: An argon and a krypton laser produce monochromatic light, which is guided through a premonochromator (to exclude plasma lines of the laser), a scrambler and polarizer (to select a polarization direction of the light) and a spatial filter (to eliminate inhomogeneities of the laser beam) into the fully achromatic entrance optics. A parabolic mirror focuses the light onto the sample. The Raman scattered light is collected by the entrance optics and directed through an analyzer (to select a specific polarization direction of the Raman signal) into the Raman spectrometer (monochromators No. 1, No. 2, No. 3 and a relay stage) and finally onto a nitrogen cooled CCD camera.

The setup (figure 3.8 and 3.9(c)), which has been utilized for all Raman measurements, is situated in a climate controlled clean room (temperature :  $22.0^{\circ}\text{C} \pm 0.5^{\circ}\text{C}$ , relative humidity:  $40\% \pm 3\%$ ) to guarantee long-time stability of the whole mechanical system. Monochromatic light is produced by a "Beamlok" krypton-ion laser and a "Beamlok" argon-ion laser partially combined with an intracavity frequency doubler. These light sources allow for resonance Raman measurements with a broad range of excitation energies from 1.55 eV (near infrared) to 6.01 eV (deep ultraviolet). The laser light is guided through several optical elements (figure 3.8) like a premonochromator, a scrambler, a polarizer and a spatial filter. The premonochromator excludes plasma lines of the laser from the beam path. The scrambler creates uniformly distributed polarization directions of the laser light, allowing to choose the desired polarization direction via the polarizer without oversized loss of intensity. A small lens brings the laser light into focus on a

pinhole of only several  $\mu\text{m}$  diameter. In this way inhomogeneities of the laser beam are eliminated and the spot size on the sample is minimized. A second lens collimates the light to an enlarged beam of a few cm diameter. All three components together are called spatial filter. Two mirrors guide the laser light into the entrance optics (figure 3.9(a) and (b)), which is assembled of four on-axis parabolic mirrors (M1, M2, M3 and M4). Due to the use of only reflecting components, the entrance optics works fully achromatic holding the advantage of not changing foci of the parabolic mirrors in dependence on excitation wavelengths. A realignment of the entrance optics with the change of excitation energy in a resonance Raman study is not necessary. The beam path through the Cassegrain type designed entrance optics is illustrated in seven steps in figure 3.9(a). The enlarged parallel laser light is guided onto M1 (step1), focusing the light onto the sample (step 2), which is positioned in a hole in M2. Spot sizes of a few  $\mu\text{m}$  can be achieved. The elastically and inelastically (Raman) and in all directions scattered light (step 3) is collected with M1. A large total collection angle of  $53^\circ$  corresponding to a numerical aperture of 0.5 provides a good yield of the commonly weak Raman signal. M1 collimates the light onto M2 (step 4), which focuses the light again (step 5). At this point an analyzer (e.g. a beam-cube analyzer) with a small hole along the optical axis is inserted into the entrance optics not influencing the light so far. Behind the focal point, the light is collimated by M3 and directed through the analyzer to select the desired polarization direction of the Raman signal (step 6). Not depicted in figure 3.9(a) is the conically drilled hole of the analyzer ensuring that almost all light is polarized. M4 focuses the light into the entrance slits of the Ultimate Triple 3 (UT-3) Raman spectrometer (step 7). A fraction of the stray light is already blocked at this point by the entrance slits. A periscope can be lowered into the beam path behind the entrance slits to visualize the sample position and the laser spot on the sample. The UT-3 Raman spectrometer is made up of two main components: the premonochromator and monochromator No. 3, the spectrograph stage, in combination with a CCD camera (figure 3.10). The premonochromator itself consists of monochromator No. 1, a relay stage and monochromator No. 2. The UT-3 is an all reflecting and this way achromatic Raman spectrometer with three high dispersive gratings. As reflecting optics only off-axis parabolic mirrors are inserted into the premonochromator to minimize image aberrations. Together with small source spots (implemented by the previous Raman setup and the entrance optics), high resolution and excellent stray light rejection can be realized over a broad wavelength range (165 nm - 1000 nm). In monochromator No. 1 the light is collimated, spectrally dispersed and focused onto slit 1. Due to wavelength dependent slightly shifted foci of the spectrally resolved light along slit 1 a band pass can be formed. The high

intensity laser wavelength and stray light is blocked. The slit is consisting of two blades, which can independently be moved from each side into the beam path. This enables many facilities to select specific band passes. Slit 2 supports slit 1 as once more stray light is rejected in the relay stage by collimating and focusing the regular beam into slit 2. Monochromator No. 2 is subtractively coupled to monochromator No. 1, i.e., the spectrally resolved signal is merged into one beam again and focused into slit 3. Further laser wavelength rejection at this point allows for Raman measurements down to a few wavenumbers cut off to the laser wavelength. Monochromator No. 3 spectrally resolves the light and focuses the Raman signal onto a nitrogen cooled CCD camera. Optimized focusing on the CCD camera due to an elliptical mirror (together with the possibility to adjust a small binning of the CCD camera) improves the signal to noise ratio. The CCD camera as well as the whole UT-3 setup is computer controlled. For more detailed information see [55].

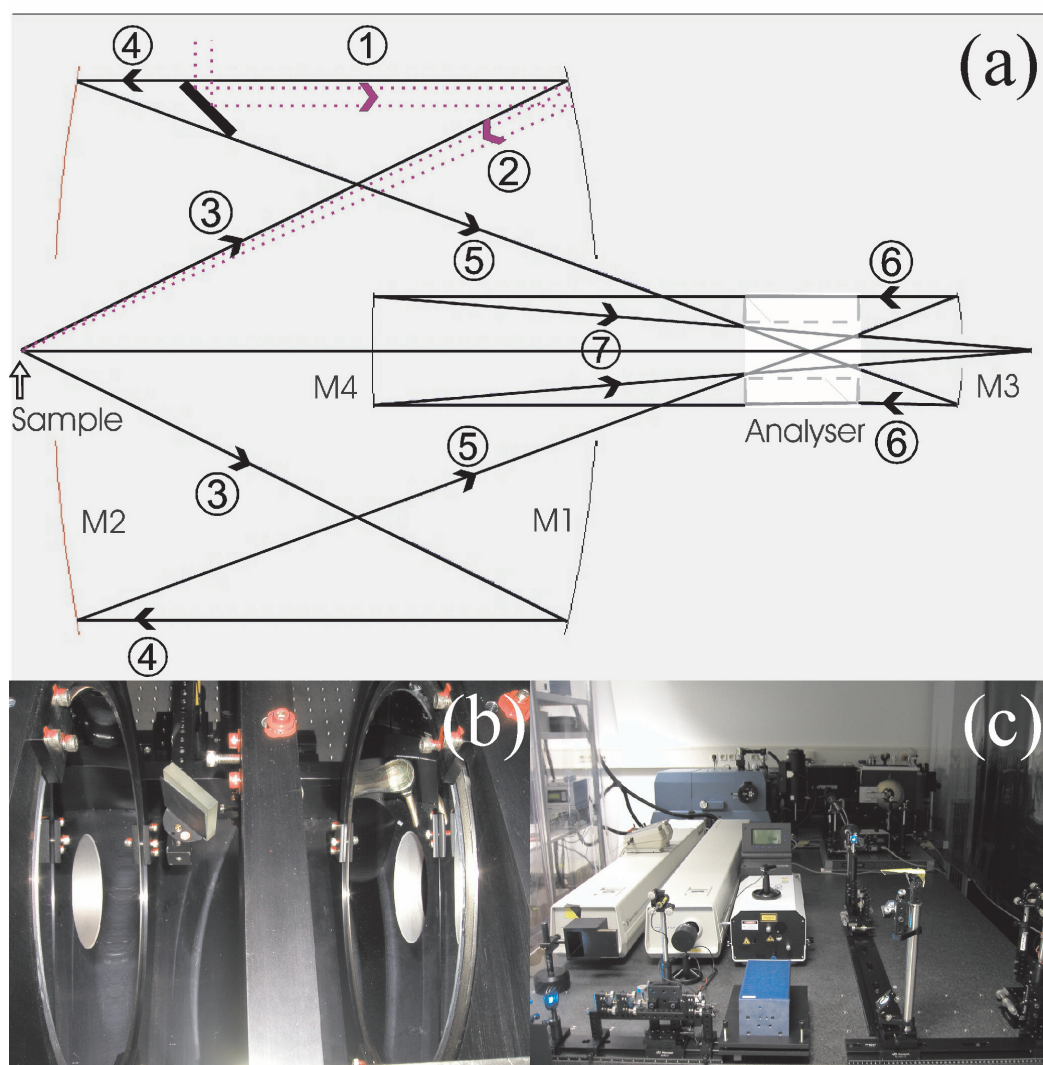


**Figure 3.9:** (a) Top view of a scheme of the achromatic entrance optics consisting of four on-axis parabolic mirrors (M1, M2, M3, M4). The beam path is shown in 7 steps. Step 1: Enlarged laser light is guided onto M1 (dotted lines). Step 2: M1 focuses the laser light onto the sample. Step 3 and 4: The scattered Raman signal is collected and collimated onto M2 by M1. Step 5: The light is focused into a hole of an inserted analyser - not influenced by the analyser so far - and collected by M3. Step 6: M3 collimates the light, which is afterwards directed through the analyser. Not depicted is the conically drilled hole of the analyser ensuring that almost all light is polarized. Step 7: M4 focuses the light into the UT-3 Raman spectrometer. (b) Top view of the entrance optics. M2 and M1 (each with a diameter of 250 mm) are visible. (c) Image of the Raman setup.

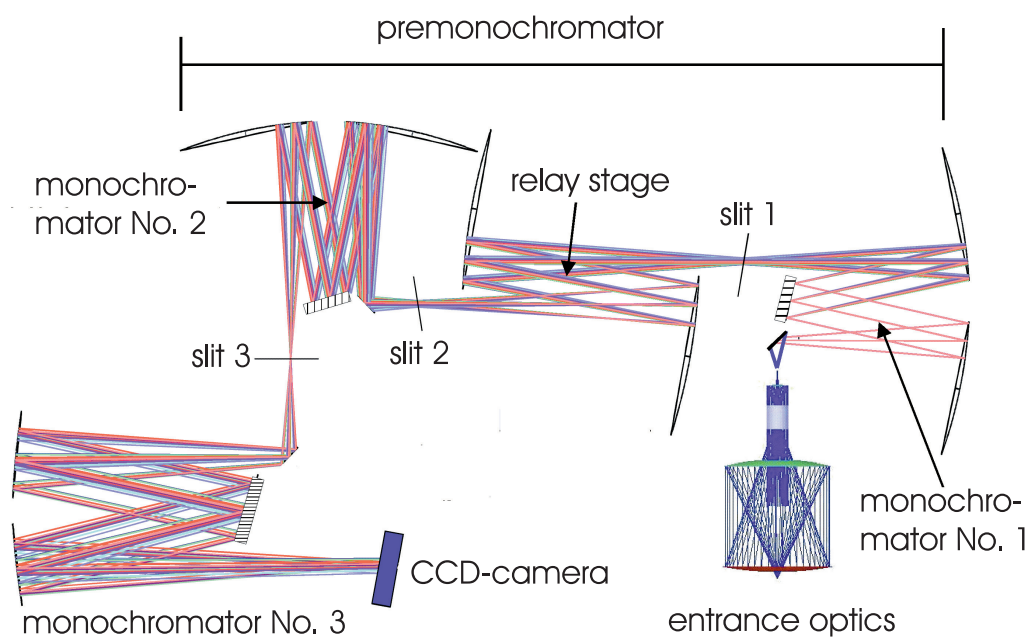


**Figure 3.10:** Ray tracings of the UT-3 Raman spectrometer (premonochromator and monochromator No. 3) and the entrance optics. The UT-3 is an all reflecting and this way achromatic Raman spectrometer with three high dispersive gratings. Off-axis parabolic mirrors in the premonochromator, consisting of subtractively coupled monochromator No. 1 and monochromator No. 2 and a relay stage, minimize image aberrations. Slit 1 and slit 2 form the band pass. Within the premonochromator an excellent stray light rejection can be realized and in combination with monochromator No. 3, the spectrograph stage, which spectrally resolves the light and focuses the Raman signal onto a nitrogen cooled CCD camera, high resolution is achieved. This allows for Raman measurements over a broad wavelength range (165 nm - 1000 nm).

### 3.7 Setup: Orbital-ordered $\text{LaMnO}_3$

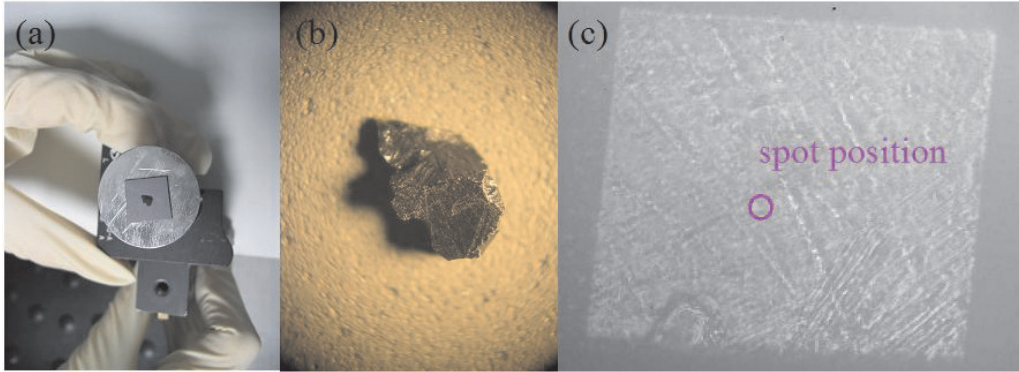


**Figure 3.11:** (a)  $\text{LaMnO}_3$  mounted on sand blasted silicon onto the sample holder and (b)  $\text{LaMnO}_3$  zoomed up. (c) Image of the sample surface in the plane of the entrance slits of the UT-3 (slit dimensions: 2 mm (width)/ 1.7 mm (height)) visualized by a periscope. The laser spot (marked) was placed onto the same position of the sample for all excitation wavelengths.

A resonance Raman scattering study at an orbital-ordered  $\text{LaMnO}_3$  single crystal has been performed with 12 excitation energies between 1.8 eV and 5.0 eV generated by a 2080 "Beamlok" krypton-ion laser (Kr) as well as a 2085 "Beamlok" argon-ion laser (Ar) - partially combined with an intracavity frequency doubler (manufactured by GWU-Lasertechnik GmbH) (laser light wavelengths in detail: 248.3 nm (Ar combined with frequency doubler), 275.4 nm (Ar), 302.4 nm (Ar), 334.5 nm (Ar), 350.7 nm (Kr), 413.1 nm (Kr), 530.9 nm (Kr), 568.2 nm (Kr), 575.3 nm (Kr), 631.2 nm (Kr), 647.4 nm (Kr), 676.5 nm (Kr)). The sample has been mounted on sand blasted silicon to minimize stray light (figure 3.11(a) and (b)). All measurements have been done at room temperature ( $T = 22 \pm 0.3^\circ\text{C}$ ) in a clean room (class 100) with controlled humidity ( $45\% \pm 3\%$ ) in backscattering configuration. The incoming and scattered light was polarized parallel along the in-plane axis. Reference measurements done by Iliev and coworkers [15] verify the right orientation of the sample by comparing the phonon spectrum. Figure 3.11(c) displays the sample surface and the well reproducible laser spot position (diameter of the spot:  $30 \mu\text{m}$ ) on the sample surface. A power of 8 mW on the sample prevented significant heating. Silicon reference measurements as well as an imaging of the sample in the plane of the entrance slits of the UT-3 complemented one another to an optimized alignment. This way the focal point of the entrance optics, in which the sample had to be positioned along the optical axis, could be found. Furthermore, the optimal focusing of the

laser spot on the sample and the sample position (figure 3.11(c)), which was reproduced at all excitation wavelengths, could be visualized. The overall sensitivity of the entire system was calibrated with the aid of two Ulbricht spheres calibration lamps. A white light spectrum originating from the Ulbricht spheres was guided into the entrance optics and detected for each bandpass. During the time flow of the resonance Raman scattering study accompanying the excitation energy changes, several silicon-reference spectra have been measured and compared resulting in a maximum error of less than 10 % in the UV. The main error originates from the achromatic behavior of the lenses in the spatial filter with changing excitation energies. Automated measurements over multiple band passes (so called "long scans" to acquire large Raman shifts) could be started computer controlled.

Paper I

Fully reflective deep ultraviolet to  
near infrared spectrometer and  
entrance optics for resonance  
Raman spectroscopy

Reprinted from  
B. Schulz, J. Bäckström, D. Budelmann, R. Maeser,  
M. Rübhausen, M. V. Klein, E. Schoeffel, A. Mihill, S.  
Yoon

REVIEW OF SCIENTIFIC INSTRUMENTS 76,  
073107 (2005)

<https://doi.org/10.1063/1.1946985>

with the permission of AIP Publishing.

# Fully reflective deep ultraviolet to near infrared spectrometer and entrance optics for resonance Raman spectroscopy

B. Schulz,<sup>a)</sup> J. Bäckström,<sup>b)</sup> D. Budelmann, R. Maeser, and M. Rübhausen  
*Institute of Applied Physics, Hamburg University, Jungiusstraße 11, 20355 Hamburg, Germany*

M. V. Klein  
*Department of Physics, University of Illinois, 1110 West Green Street, Urbana, Illinois 61801*

E. Schoeffel and A. Mihill  
*McPherson Inc., 7A Stuart Road, Chelmsford, Massachusetts 01824*

S. Yoon  
*National Renewable Energy Laboratory, 1617 Cole Boulevard, Golden, Colorado 80401  
 and Division of Nano Sciences and Department of Physics, Ewha Womans University,  
 11-1 Daehyun-dong, Seodaemun-Gu, Seoul 120-750, Korea*

(Received 10 February 2005; accepted 14 May 2005; published online 1 July 2005)

We present the design and performance of a new triple-grating deep ultraviolet to near-infrared spectrometer. The system is fully achromatic due to the use of reflective optics. The minimization of image aberrations by using on- and off-axis parabolic mirrors as well as elliptical mirrors yields a strong stray light rejection with high resolution over a wavelength range between 165 and 1000 nm. The Raman signal is collected with a reflective entrance objective with a numerical aperture of 0.5, featuring a Cassegrain-type design. Resonance Raman studies on semiconductors and on correlated compounds, such as  $\text{LaMnO}_3$ , highlight the performance of this instrument, and show diverse resonance effects between 1.96 and 5.4 eV. © 2005 American Institute of Physics. [DOI: 10.1063/1.1946985]

## I. INTRODUCTION

Inelastic light scattering, or Raman scattering, is a very versatile and powerful experimental probe, useful in many fields of physics, chemistry, and technology.<sup>1-5</sup> It can be used in applied fields such as forensics or to study very fundamental topics such as quasiparticle dynamics in condensed matter.<sup>6-9</sup> A successful realization of a Raman scattering measurement puts high demands on the spectrometer. Since the Raman signal itself has very low intensity compared to the incident monochromatic excitation light, high stray light rejection is necessary in order to cut out the excitation frequency and to be able to measure low-frequency excitations. Moreover, high spectral resolution is desirable for many applications such as the measurement of low-energy acoustic and soft modes.

Inelastic light scattering is a two photon process, which couples to a particle by means of the vector potential of the electromagnetic field  $\mathbf{A}$ . Considering a particle with mass  $m$  and its kinetic energy  $\tilde{\mathbf{p}}^2/2m$ , where  $\tilde{\mathbf{p}}$  is the canonical momentum. For a free particle, the canonical momentum  $\tilde{\mathbf{p}}$  equals the momentum  $\mathbf{p}=m\cdot\mathbf{v}$ , where  $\mathbf{v}$  is the velocity of the particle, yielding  $H_0=\mathbf{p}^2/2m$ . However, for a charged particle, the gauge invariance of the Maxwell equations yields a

canonical momentum  $\tilde{\mathbf{p}}\rightarrow\mathbf{p}-e/c\cdot\mathbf{A}$ , where  $e$  is the elementary charge. This yields:

$$\tilde{\mathbf{p}}^2\rightarrow\frac{\mathbf{p}^2}{2m}-\frac{e}{mc}\cdot[\mathbf{p}\cdot\mathbf{A}+\mathbf{A}\cdot\mathbf{p}]+\frac{1}{2m}\left(\frac{e}{c}\right)^2\mathbf{A}^2. \quad (1)$$

This leads to the following Hamiltonians:

$$\tilde{H}\rightarrow H_0+H^{\mathbf{P}\cdot\mathbf{A}}+H^{\mathbf{A}^2}=H_0+H_{\text{int}}. \quad (2)$$

The  $\mathbf{A}^2$ -term yields nonresonant inelastic light scattering. However, in most experimental situations, i.e., for NIR to UV light, sufficient optical matrix elements are available to activate resonant inelastic light scattering in second order perturbation using  $H^{\mathbf{P}\cdot\mathbf{A}}$ . The variation of the incident photon energy enables an identification of specific matrix elements and the quasiparticles that couple to them. If the excitation frequency of the incoming light is equal to the transition frequency from an initial to an intermediate state of the system, resonant Raman scattering occurs.<sup>10</sup>

The internal differential light scattering cross section for a virtual interband contribution to electronic Raman scattering is:<sup>11</sup>

$$\frac{d^2\sigma_{\text{in}}}{d\omega_s d\Omega_s}=\frac{\omega_s r_o^2}{\omega_i} [1+n(\omega_i-\omega_s)] A_{V_I} \times \sum_F |T_{FI}^i|^2 \delta\left(\omega_i-\omega_s-\frac{E_F-E_I}{\hbar}\right), \quad (3)$$

where  $\omega_i(\omega_s)$  is the frequency of the incident (scattered) light,  $n(\omega)$  is the Bose factor,  $A_{V_I}$  is the average over initial

<sup>a)</sup> Author to whom correspondence should be addressed; electronic mail: Ben99@gmx.net

<sup>b)</sup> Present address: Joakim Bäckström, PhD, Development Engineer, Permascand AB, Box 42, SE-84010, Ljungaverk, Sweden.

states  $I$ ,  $F$  represents final states,  $E_{I,F}$  represents their energies,  $r_o$  is the classical electron radius  $e^2/mc^2$ . The dimensionless second order “transition matrix element”  $T_{FI}^{si}$  is given by a sum over intermediate states  $M$ :

$$T_{FI}^{si} = \sum_{M \neq I, F} \frac{1}{m} \left( \frac{\langle F|P_s|M\rangle \langle M|P_i|I\rangle}{E_I - E_M + \hbar\omega_i + i\delta} + \frac{\langle F|P_i|M\rangle \langle M|P_s|I\rangle}{E_I - E_M - \hbar\omega_s - i\delta} \right), \quad (4)$$

where  $P_i(P_s)$  is the component of the total electron momentum operator along the polarization direction of the incident (scattered) light, and  $E_I(E_M)$  is the energy of the initial (intermediate) state. To obtain the above results, we have taken the limit of zero wave vector transfer ( $q=0$ ). The parameter  $\delta$  is a positive infinitesimal. The effect of scattering and many-body interactions on the state  $M$  can be approximately taken into account by replacing  $\delta$  by the inverse lifetime  $\Gamma$  of the state  $M$ .<sup>12</sup>

The quantity  $T_{FI}^{si}$  bears a close resemblance to the polarization operator that describes the self-energy acquired by a photon of frequency  $\omega$  propagating through the scattering medium due to interband transitions. In the limit of zero photon wave vector, the polarization operator for a photon polarized along direction  $\alpha$  is given by

$$\Pi^{\alpha\alpha}(\omega) = \frac{e^2}{mV} A_{VI} \sum_M \frac{1}{m} \left[ \frac{\langle I|P_\alpha|M\rangle \langle M|P_\alpha|I\rangle}{E_I - E_M + \hbar\omega + i\delta} + \frac{\langle I|P_\alpha|M\rangle \langle M|P_\alpha|I\rangle}{E_I - E_M - \hbar\omega - i\delta} \right], \quad (5)$$

where  $V$  is the normalization volume of the system. The essential difference between Eqs. (4) and (5) is that the final state  $F$  in Eq. (4) becomes the initial state  $I$ , which is averaged over in Eq. (5). The connection between the polarization operator and the local or interband contribution to the dielectric constant tensor  $\epsilon_{\alpha\beta}(\omega)$  is<sup>13</sup>

$$\Pi^{\alpha\alpha}(\omega) = -\frac{[\epsilon_{\alpha\alpha}(\omega) - 1]\omega^2}{4\pi}. \quad (6)$$

The similarity between Eqs. (4) and (5), together with Eq. (6) leads to the suggestion that one should compare the interior Raman cross section as a function of  $\omega_i \approx \omega$  with  $|\epsilon_{\alpha\alpha}(\omega) - 1|^2 \omega^4$ . Therefore, one can use optical absorption edges in the ultraviolet spectral range ideally to improve the signal. Furthermore, it is crucial to be able to investigate especially biological samples in spectral regions other than the visible, since the intrinsic luminescence can be very strong. The large accessible wavelength range, therefore, enables one to enlarge the fields of research.

In this paper, we present the concept, design, construction, and performance tests of a new all-reflecting achromatic triple-grating micro-Raman setup with extreme spectral agility (maximum usable wavelength range with current mirror coatings 165–2000 nm) and high spatial as well as spectral resolution. Key ingredients to the concept include diffraction-limited imaging, parabolic as well as elliptical mirror optics, software coupled subtractive or triple additive operation of the high performance gratings.

When comparing Raman spectra acquired using different excitation energies, the optical properties of the sample at the respective energies have to be taken into account. Parameters like the reflection coefficients of solids and the penetration depth change with energy, therefore, the Raman spectra have to be corrected.

The optical parameters  $n$  and  $k$  or  $\epsilon_1$  and  $\epsilon_2$  at the used excitation energies have to be derived using spectroscopic ellipsometry. The reflection coefficients can be calculated knowing those parameters; the fraction  $R(\omega_i)$  of the incident laser light will be directly reflected, thus  $[1 - R(\omega_i)]$  of the light penetrates the sample. Analogously,  $[1 - R(\omega_s)]$  of the scattered light leaves the sample. Furthermore, the penetration depth as a function of incident and scattered photon energy of the light needs to be considered. This can be done by using an effective penetration depth:

$$\tilde{\beta} = \frac{\beta(\omega_i)\beta(\omega_s)}{\beta(\omega_i) + \beta(\omega_s)}, \quad (7)$$

with

$$\beta(\omega_{r,s}) = \frac{c}{2\omega_{r,s}k'(\omega_{r,s})}, \quad (8)$$

where  $k'$  is the frequency dependent absorption coefficient, the imaginary part of the complex refractive index.

Additionally, the properties of the collecting objective are important, since the scattered light has to lie in a cone defined by the opening angle  $\theta_{\text{Obj}}$ . How many photons are situated in this cone is also dependent on the optical properties of the sample. This correction is called solid-angle correction. Due to the refraction at the sample surface, the angle  $\theta_{\text{Obj}}$  is changing to  $\theta_{\text{Sam}}$  according to the modified refraction law:<sup>14</sup>

$$n \sin(\theta_{\text{Obj}}) = n_T \sin(\theta_{\text{Sam}}). \quad (9)$$

In recent publications, the value of  $n_T$  was set equal to  $n'(\omega)$ , the real part of the complex refractive index of the sample material.<sup>15</sup>  $n_T$  actually has a complicated dependence on the optical properties of the sample, which are frequency dependent. Due to the large entrance optics of the UT-3, a non-negligible dependence on the collecting angle of the objective,  $\theta_{\text{Obj}}$ ,

$$n_T = \sqrt{n^2 \sin^2 \theta_{\text{Obj}} + \eta^2 \cos^2 \phi}, \quad (10)$$

with

$$\eta^2 \cos 2\phi = n'^2 - k'^2 - n^2 \sin^2 \theta_{\text{Obj}},$$

$$\eta^2 \sin 2\phi = 2n'k',$$

needs to be considered. This can be evaluated using  $n=1$  for air as surrounding medium and  $\cos^2 \phi = (1 + \cos 2\phi)/2$ :

$$n_T^2 = \frac{1}{2} \left[ \sqrt{(n'^2 - k'^2 - \sin^2 \theta_{\text{Obj}})^2 + (2n'k')^2} + (n'^2 - k'^2 + \sin^2 \theta_{\text{Obj}}) \right] \quad (11)$$

$$n_T^2 = n'^2 + \frac{1}{2}(n'^2 + k'^2 - \sin^2 \theta_{\text{Obj}}) \times \left[ \sqrt{1 + \frac{4k'^2 \sin^2 \theta_{\text{Obj}}}{(n'^2 + k'^2 - \sin^2 \theta_{\text{Obj}})} - 1} \right]. \quad (12)$$

Therefore, the solid angle correction can be calculated as:

$$\tan^2(\theta_{\text{Sam}}) = \tan^2\left(\sin^{-1} \frac{\sin \theta_{\text{Obj}}}{n_T}\right). \quad (13)$$

In total, the effective sample volume correction and the correction for the reflectivity of the investigated sample applied on the acquired spectrum with intensity  $I_{\text{raw}}$  may then be written as

$$I_{\text{cor}} = I_{\text{raw}} / \left[ \underbrace{[1 - R(\omega_i)]^2}_{\text{reflectivity}} \cdot \underbrace{\beta(\omega_i)}_{\text{penetration depth}} \cdot \underbrace{\tan^2\left(\sin^{-1} \frac{\sin \theta_{\text{Obj}}}{n_T}\right)}_{\text{volume solid angle}} \right] = I_{\text{raw}} / \underbrace{c_f}_{\text{correction factor}}. \quad (14)$$

The angle  $\theta_{\text{Obj}}$  is  $26.56^\circ$ , which corresponds to a total collection angle of  $53^\circ$ , the sine function squared yields a value of 0.2.

The solid-angle correction has to be applied also when comparing measurements at one wavelength with different polarization geometries in case the sample is anisotropic. Since the optical constants are dependent on the orientation of the sample to the polarization direction of the incident laser light, the solid-angle correction is different for light polarized parallel to one axis of the sample and for light polarized parallel to the other axis. In case circularly polarized light is used, the solid angle correction is calculated using the averaged optical properties. However, care needs to be taken with scattering configurations that lose polarization purity in anisotropic materials.

## II. SYSTEM OVERVIEW

In this section, we discuss the hardware of the spectrometer itself. To provide long-time stability of the whole setup, the system is situated in a climate controlled clean room with controlled temperature ( $22.0^\circ\text{C} \pm 0.5^\circ\text{C}$ ) and controlled relative humidity ( $40\% \pm 3\%$ ). This ensures mechanical stability and protection of mirror coatings, thus enabling work with short wavelengths. The system has two major parts, the entrance optics and the Raman spectrometer, referred to as UT-3. A mechanical and optical overview of the system is shown in Fig. 1.

### A. Entrance optics

Because the Raman signal is scattered in all directions, for weak scattering one needs to use as large a solid angle as possible. In resonance Raman work it is a great advantage not to have to refocus the collecting optics each time the exciting laser wavelength is changed. For these reasons, special entrance optics were designed. In this case, a Cassegrain

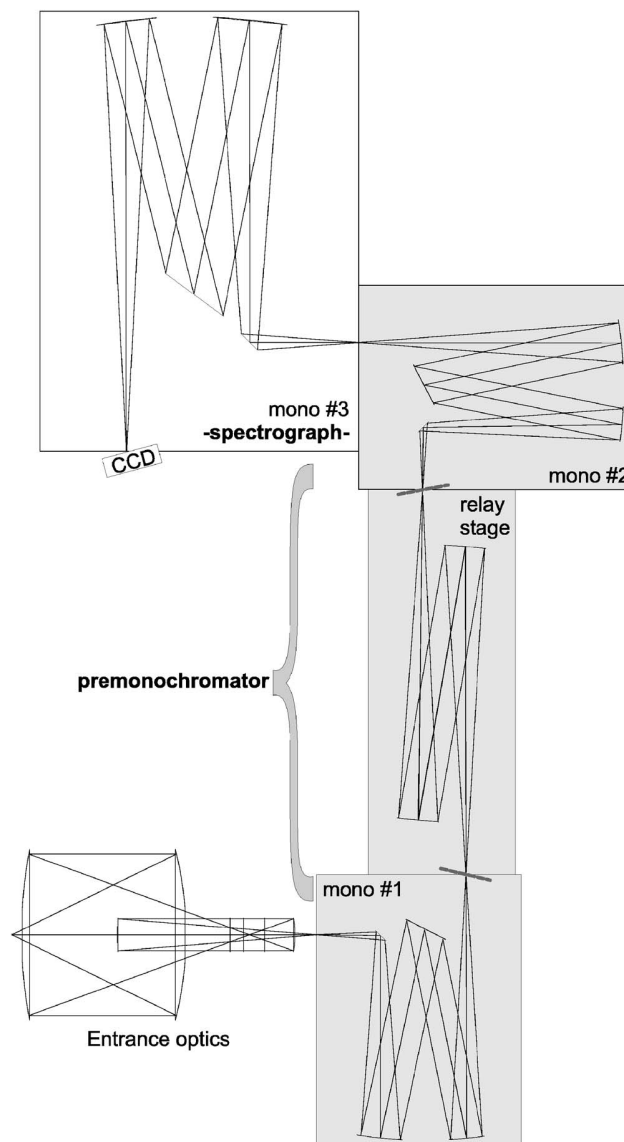


FIG. 1. Ray tracing drawing of the setup showing the entrance optics, which focuses the light into the first monochromator. Together with the relay stage and monochromator No. 2, they form the premonochromator (gray boxes). The light is spectrally resolved in monochromator No. 3, the spectrograph stage. Note, the tilted CCD plane as well as the tilted band pass slit planes (dashed grey lines) in the premonochromator stage to optimize focusing.

type design was adapted for the use as the entrance optics. This all-reflecting, fully achromatic, objective consists of four on-axis parabolic mirrors, as depicted in Fig. 2. The first mirror has a numerical aperture of 0.5, F-number 1; the last mirror has an F-number of 5.8. This is also the overall magnification of the system. The Raman signal is collected with M1, collimated onto M2, which forms an intermediate image in front of M3. This mirror collimates the light to provide a parallel beam section for the insertion of a polarization analyzer. Finally, M4 focuses the light into the spectrometer. A ray-tracing drawing together with images from the actual optics are shown in Fig. 2. The mirrors M1 and M2 have diameters of 250 mm, the mirrors M3 and M4 have a diameter of 50 mm. As analyzers, we use custom-made beam-splitter-cubes with a central hole manufactured by B. Halle Nach-

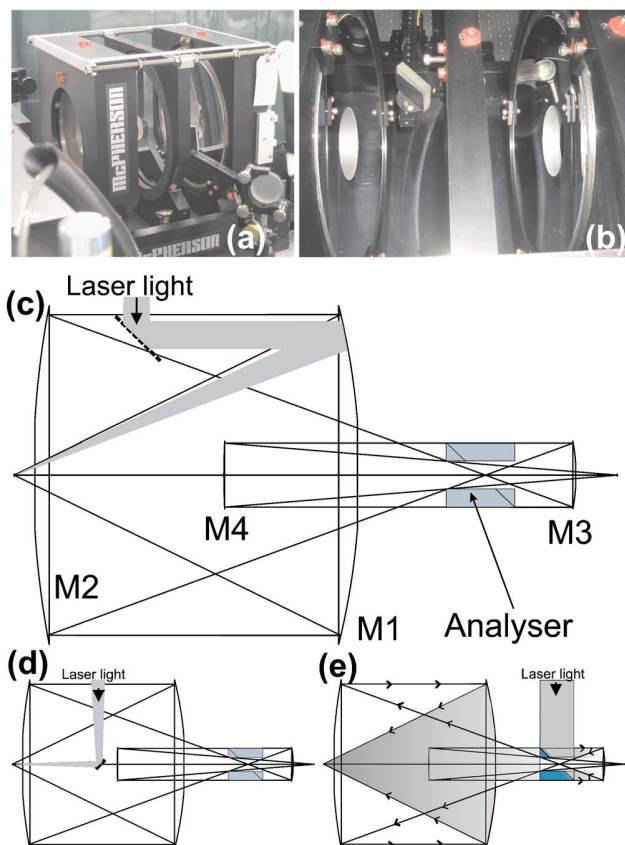


FIG. 2. Images and ray tracings of the entrance optics. Images (a) and (b) show the rigid mounts for the large parabolas. In (b), the 45-degree mirror which guides the laser light onto the sample is visible; (c) ray-tracing drawing of the entrance optics. The Raman signal is collected with M1, collimated onto M2, which focuses the light in front of M3. This mirror collimates the light to provide a parallel beam section for the insertion of an analyzing beam cube with central hole. Finally, M4 focuses the light into the spectrometer. The dashed line represents the 45-degree mirror, the gray area shows the incident laser light. This is the standard configuration; (d) and (e) show alternatives for coupling in the incident laser light, either using a small mirror behind M4 (d) or using the analyzing beam cube (e), thus realizing true backscattering geometry

folger GmbH. There are four different cubes optimized to different wavelength ranges.

Figure 2 also gives an overview of the different possibilities the entrance optics offers to couple the incident laser light onto the sample. In the standard configuration, the collimated laser beam emergent from the spatial filter is guided with two steering mirrors onto the parabola M1, which focuses the light on the sample in the focus point. This configuration is depicted in Fig. 2(c). Alternatively, there is the option of placing a small planar 45-degree mirror behind M4 to deflect the laser onto the sample. In this case, the collimated beam has to be focused using a lens with a long focal length outside the entrance optics. This configuration, schematically displayed in Fig. 2(d), will create a true backscattering geometry, but the spot size on the sample will be larger due to the diffraction and aberrations in the laser beam introduced by the focusing lens. Figure 2(e) shows a method for creating a true backscattering geometry and a very small focal spot. Here, the polarizing beam-cube analyzer is used to couple the light into the entrance optics; the laser beam

runs backwards through the mirrors onto the sample. Since the full aperture of the mirrors is used, the focal spot will be aberration free and very small.

## B. UT-3

The entrance optics focuses the collected light into the entrance slit of the first monochromator of the UT-3. The UT-3 can be divided in four parts: The first monochromator, mono No. 1; the relay stage; mono No. 2, the second monochromator, which is a mirrored copy of mono No. 1; and the third monochromator, mono No. 3. Mono No. 1 and No. 2 both have focal lengths of 400 mm, and mono No. 3 has a focal length of 667 mm. They all have an F-number of 5.8. All mirrors except the mirrors in mono No. 3 are off-axis paraboloids to minimize aberrations and ensure perfect focusing. Since off-axis paraboloids create very small focal points, which are free of aberrations on the optical axis, the stray light rejection by the premonochromator is extremely high. Moreover, the light is focused onto small areas of the CCD-chip, thus optimizing the signal-to-noise ratio. The collected light is spectrally resolved in mono No. 1 and then refocused on the entrance slit of the relay stage. This slit, as well as the exit slit of the relay stage, features monolateral slit blades to provide high versatility in forming the band pass. The relay stage collimates and refocuses the light to optimize the straylight rejection with the use of these two band pass slits. The monolateral slits allow for an asymmetric band pass setting, which may profit from the aberration free on-axis imaging. In mono No. 2, the light is collimated onto the grating, which merges the spectrally resolved light back into one beam, which is then refocused onto the entrance slit of mono No. 3, the so-called intermediate slit. In mono No. 3, one elliptical and one spherical mirror together with a large grating and long beam path provide high resolution on the CCD-camera. The elliptical mirror focuses the light also in the vertical direction, i.e., perpendicular to the direction of the wavelength dispersion due to the grating. This ensures high photon flux onto a small number of CCD-pixels, thereby optimizing the signal to noise ratio. The image formation at the entrance and intermediate slit can be surveyed with two periscopes, which can be lowered into the optical axis. In the present setup, the periscope at the entrance slit is configured to bring the image of the sample in the plane of the entrance slit onto a UV-sensitive CCD camera. This is used for sample positioning and focusing.

All three monochromators are equipped with revolving turrets holding kinematic mounts to change gratings in the system during a run. Currently, two sets of gratings are in use: One set covers the visible wavelength range from 350 to 860 nm (VIS). It consists of three holographic gratings with 1800 lines per millimeter, blazed for 500 nm. The second holographic set is for the use in the UV range, and is blazed at 250 nm, therefore covering the range from 185 to 400 nm (UV). For mono No. 1 and No. 2, 1800 lines per millimeter are used as well; the grating in the spectrograph stage has 2400 lines per millimeter. Table I summarizes these parameters and gives the grating sizes in the different stages.

TABLE I. Parameters of the gratings used in the UT-3. VIS denotes the spectral range from 350 to 860 nm, UV denotes the spectral range from 185 to 400 nm.

| Grating set | Mono No. | Ruling    | Size                    |
|-------------|----------|-----------|-------------------------|
| VIS         | 1        | 1800 l/mm | 64×64 mm <sup>2</sup>   |
| VIS         | 2        | 1800 l/mm | 64×64 mm <sup>2</sup>   |
| VIS         | 3        | 1800 l/mm | 110×110 mm <sup>2</sup> |
| UV          | 1        | 1800 l/mm | 64×64 mm <sup>2</sup>   |
| UV          | 2        | 1800 l/mm | 64×64 mm <sup>2</sup>   |
| UV          | 3        | 2400 l/mm | 110×110 mm <sup>2</sup> |

The wavelength separation and band pass formation in the spectrometer is versatile. The premonochromator stage is usually used in subtractive mode, i.e., the spatially dispersed light in mono No. 1 is partially blocked by the slit blades in the relay stage, resulting in a pass band of transmitted wavelength which is then collapsed by the action of mono No. 2. The spectrograph stage spatially disperses the light of the pass band again onto a liquid nitrogen cooled CCD-camera (Roper Scientific), where the direction of dispersion is parallel to the long axis of the CCD-chip. The spectrometer can also be used in additive mode. In this case, the light transmitted through the pass band would not be collapsed but dispersed even more in mono No. 2. Then the intermediate slit would define the wavelengths which are transmitted into the spectrograph stage. These already spatially separated wavelengths would be further dispersed, yielding an extremely high energy resolution image at the CCD-plane. However, this pass band would only cover a short wavelength range. Ray tracings show that the image would cover less than half of the wavelength range in subtractive mode, with at least doubled resolution.

Last, the setup includes the possibility of bypassing the complete premonochromator stage and coupling directly into

the spectrograph stage via a second entrance port and a notch filter to reject elastically scattered laser light. This option allows fast measurements with high efficiency, but lower stray light rejection and loss of the low-frequency region  $<150\text{ cm}^{-1}$  of the Raman spectra. Moreover, the notch filter can only be used at or around its design wavelength.

The whole system including CCD camera, turrets, slits, and grating angles is motorized and computer controlled. “Labview” control software was programmed and contains all needed procedures. The software controls grating movements, slit jaw movements for all slits (excluding manually adjustable horizontal jaws at the entrance of the UT-3) and the CCD-camera. The software also has functions to calibrate the system. The user is also able to run automated measurements to acquire multiple band passes. Data are stored in XML-format, including all relevant parameters, user comments, and the acquired spectrum. For further analysis, the software is able to export spectra in text format.

### C. Infrastructure

A broad band spectrometer like the UT-3 requires access to a large number of excitation energies, especially when doing resonance Raman spectroscopy. Therefore, we use two laser systems and an intracavity frequency doubling unit as light sources. The accessible excitation wavelengths, energies, and maximum output powers are given in Fig. 3. The laser systems are manufactured by Spectra Physics, Inc. and include a 2085 “Beamlok” argon-ion laser as well as a 2060 “Beamlok” krypton-ion laser. The argon laser tube is optimized for use in the UV-range; the lowest intrinsic line is at 275 nm or 4.51 eV. The intracavity frequency doubler is manufactured by GWU-Lasertechnik GmbH and consists of a housing holding an interchangeable mirror set and a specialized BBO crystal. Currently, three different crystals and mirror sets for frequency doubling lines between 502 and

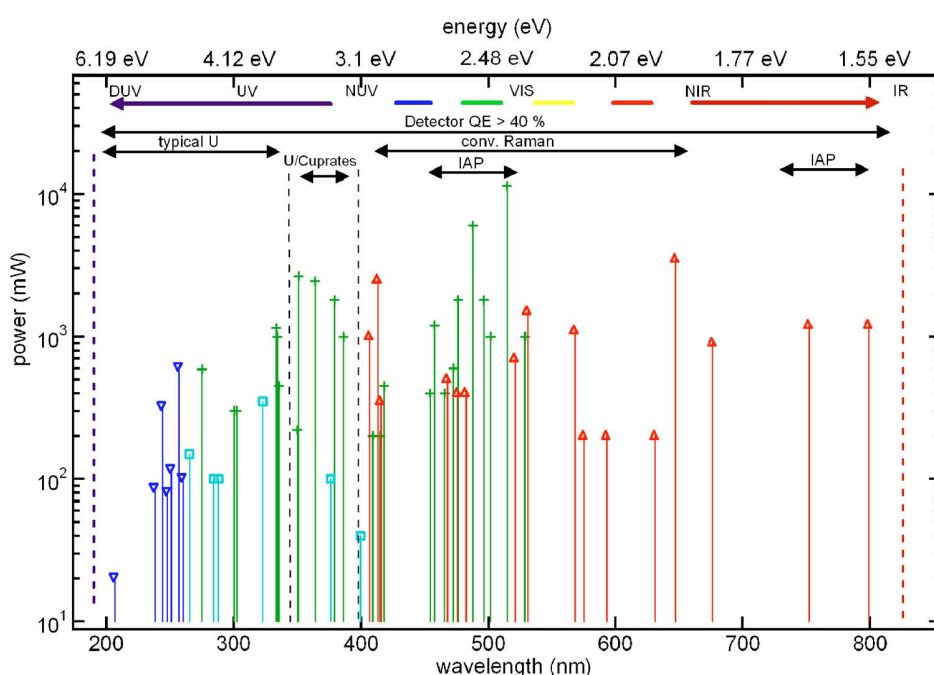


FIG. 3. Accessible wavelengths and energies in the Raman setup: (+) argon-ion laser, ( $\Delta$ ) krypton-ion laser, ( $\nabla$ ) intracavity frequency doubled laser lines, ( $\square$ ) frequency doubled lines accessible with other crystals.

476 nm, 520 and 495 nm, as well as 420 and 410 nm are available. The frequency doubled lines have energies between 4.77 and 6.01 eV.

The laser light is guided through a beam path on a large optical table with a premonochromator to eliminate plasma lines (SpectroLab), a scrambler and polarizer to select the incoming polarization and a spatial filter made from components from Newport Optics to produce a homogeneous spot on the sample. The spatial filter consists of a small lens with a focal length of 5 mm, an interchangeable, high power pinhole with diameters of 2–50  $\mu\text{m}$ , and a collimating lens with a focal length of 150 mm. The enlarged beam leaving the spatial filter is guided by two mirrors onto the mirror M1 of the entrance optics as described previously. In this geometry, the pinhole aperture is enlarged by a factor of 1.6, thus resulting in a spot size on the investigated samples of 3.5–80  $\mu\text{m}$ .

### III. DESIGN VERIFICATION

In this section, we show the expectations of the performance of the setup based on ray tracing and numerical simulations. These expectations are then compared with the actual performance of the setup. The ray tracings were made using ZEMAX optical design software. In this program, rays of specific wavelengths can be traced through optical systems. A given number of rays, ranging from 25 000 to 1 000 000, was used for the simulations shown here. These rays can also be spread over the defined wavelengths in a specific ratio. Usually the rays were spread evenly over the range of wavelengths. Only for the simulations of stray-light rejection the ratio was different. The software also allows apertures to be set where the slits are situated. The aperture sizes were set to match actual slit widths ranging from 25 to 200  $\mu\text{m}$ . When simulating intensities on the detector, the image plane in the software was set to be made of pixels 20  $\mu\text{m}$  by 20  $\mu\text{m}$  in size, thus resembling the actual CCD-camera parameters. Vignetted rays are deleted.

Simulated images on the CCD-plane of the spectrograph stage are presented in Figs. 4(a)–4(c). In the simulation, three energy regions are covered, around 4.96, 2.485, and 1.552 eV. Due to the limitations of the ray tracing software, only specific wavelengths can be calculated. They were selected to span the whole CCD-chip with its length of 26.8 mm and height of 8 mm. The center of the CCD coincides with the optical axis of the spectrograph stage. The centered wavelengths are optimally focused on the CCD. The larger the distance of a wavelength from the center, the broader the image. This is due to the off-axis aberrations. To minimize this effect, the elliptical mirror in the spectrograph stage was used. With a spherical mirror, the spread of the off axis wavelength spot would be three times larger than is shown in the simulation with the elliptical mirror. The corresponding experimental image acquired with the CCD-camera is depicted in Fig. 4(d). Here, a white light source was imaged through the system. The gratings were adjusted to image light around 2.48 eV (500 nm) with optimum subtractive coupling. As shown by the simulations, the image is more disturbed towards the edges of the spectrum and has a

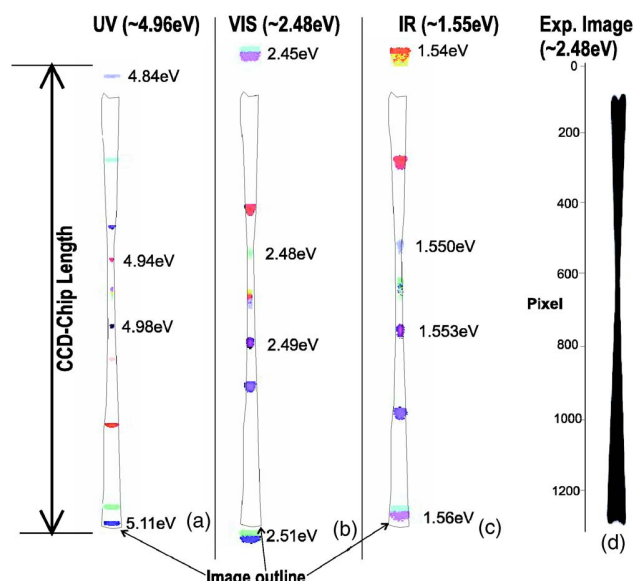


FIG. 4. (a)–(c) Dispersion in the ultraviolet (UV), visible (VIS), and infrared (IR) spectral regions. The colored dots represent simulated focal spots on the CCD image plane for various discrete photon energies when the gratings are rotated to put (a) 4.96 eV, (b) 2.48 eV, and (c) 1.55 eV photons at the center of the CCD chip. (Note that the dispersion is shown as occurring vertically, contrary to the actual horizontal dispersion.) Clearly visible are the effects of the off-axis aberrations, especially coma; (d) experimental image from a white light source on the CCD-camera, with gratings rotated as in (b); on the detector, each pixel is 20  $\mu\text{m}$  by 20  $\mu\text{m}$  in size. From (d), an outline of the spectrum is taken, producing the thin lines which encase the simulated images (a)–(c) very well.

waist in the center of the image, on the optical axis of the system. To be able to compare experimental results with the simulation, the outline of the experimental image was moved to the simulated images. This shows that the shape of the observed spectrum closely matches the simulations.

The experimental image shows only the spatial form of the pass band, not its intensity. The intensity shape of the pass band in high resolution mode, i.e., operating the spectrometer with very small entrance and intermediate slits, was also first simulated and then compared with the experimental results. Figure 5 shows an illumination plot of the CCD-plane; the envelope was drawn as a guide to the eye. The entrance slit of the system and the intermediate slit at the entrance of the spectrograph stage were set to 25 and 40  $\mu\text{m}$ , respectively. The resulting bell-shaped white light spectrum is also due to the increased off-axis aberrations at the positions far away from the optical axis of the system. Since the simulation cannot include CCD-binning, the drop off towards the edge is slightly overestimated compared to the measurements due to the geometrical image formation shown in Fig. 4. Figure 6 gives an example of the experimentally acquired white light spectra, depending on the used slit widths for entrance and intermediate slit. As already simulated, the spectrum is bell shaped when using very small slits. Enlarging the slits results in a flattening of the spectrum due to the increased on-axis aberrations of the enlarged on-axis image. Of course the resolution of the system is also lowered. All shown spectra were acquired using binned CCD-pixels.

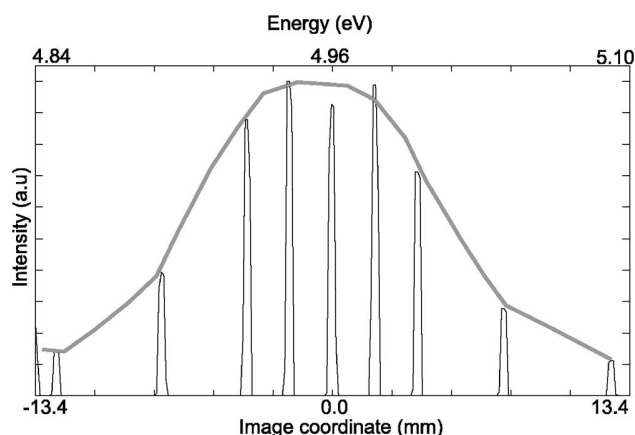


FIG. 5. Simulation of the white light signal on the CCD chip. Discrete lines from 4.48 to 5.17 eV and their corresponding positions on the CCD-chip are traced through the instrument in order to obtain their relative intensities. The peak height of these intensities have been connected to visualize the shape of a white-light source. The slit width for this simulation was set to 25  $\mu\text{m}$  for the entrance slit of the system, and 40  $\mu\text{m}$  for the intermediate slit at the entrance of the spectrograph stage.

Another important factor for the performance of such a system is the overall efficiency, i.e., the probability that a photon leaving the sample within the acceptance angle will actually reach the detector. Based on data sheets for the sensitivity of gratings and coated mirrors (Acton Research No. 2000 broadband VUV/UV coating), an overall sensitivity for the system was calculated. Figure 7 shows that this efficiency depends on the polarization state of the incoming light, a dependence that results from the polarization dependence of the grating efficiency. At the specified blaze wavelength of the VIS-gratings, around 2.48 eV, the overall efficiency is independent of the polarization. Strongly visible is also the weaker efficiency in the UV region below 3.5 eV. The envelope gives the expected efficiency when working always in the polarization direction having strongest sensitivity. For calibrating the overall sensitivity of the entire system shown in Fig. 1, two Ulbricht sphere calibration lamps were used, one for the UV-range and one for the VIS-range. Inside an Ulbricht sphere, a homogeneous radiation field over a broad energy range is generated. Thus Ulbricht

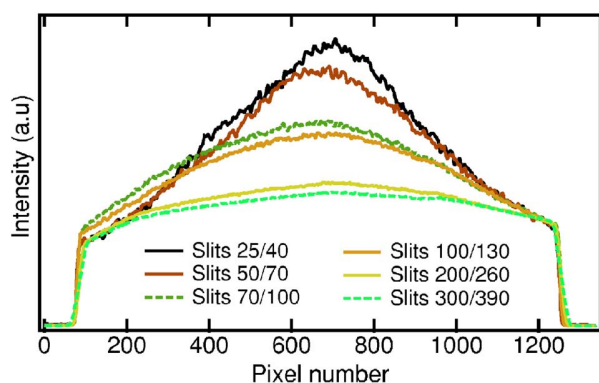


FIG. 6. Experimental results for a white light spectrum, shown using different slit widths for entrance/intermediate slit, respectively. Spectra have been scaled to match at the edges of the pass band. Note that the black solid curve corresponds to the simulation shown in Fig. 5.

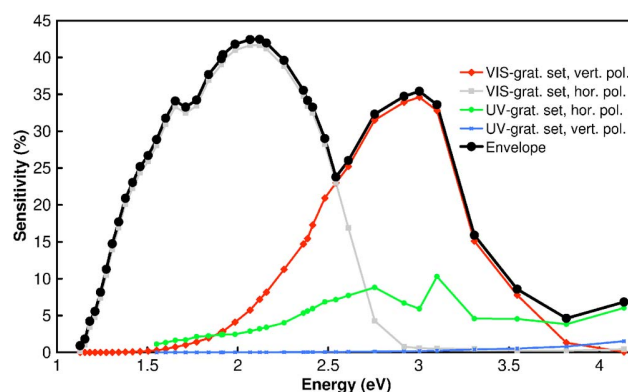


FIG. 7. Calculated sensitivity of the overall system based on data sheets for gratings, CCD efficiency, and mirror coatings, including different polarization sensitivity of the gratings (hor. pol.=horizontal polarization, vert. pol.=vertical polarization). The solid line represents the effective sensitivity of the instruments as it is used by adapting the polarization of the scattered photons.

spheres resemble a grey body radiator. The lamps had small ( $\approx 1$  cm diameter) exit holes, which were placed in the focal plane of the entrance objective. For each pass band, a white light spectrum was acquired. These spectra were corrected for integration time, electronic background and lamp brightness.

The measured sensitivity of the UT-3 system is given in Fig. 8. Only the polarization direction with the highest sensitivity is shown. An envelope was fitted through the obtained pass bands. The sensitivity without the use of an analyzer and with the more sensitive polarization direction is shown. The measured data resemble quite well the simulated results, apart from the obviously different blaze wavelength at around 2.26 eV.

One of the major parameters for a Raman spectrometer is its resolution. High resolution is a prerequisite for resolving doping, temperature, or energy related shifts in phonons or to ensure superb stray light rejection to investigate low energy regions. High resolution can be created by small source spots resulting in small images, and by strongly dispersive elements. In the UT-3 system, both schemes are used. The gratings are strongly dispersive, and the system pro-

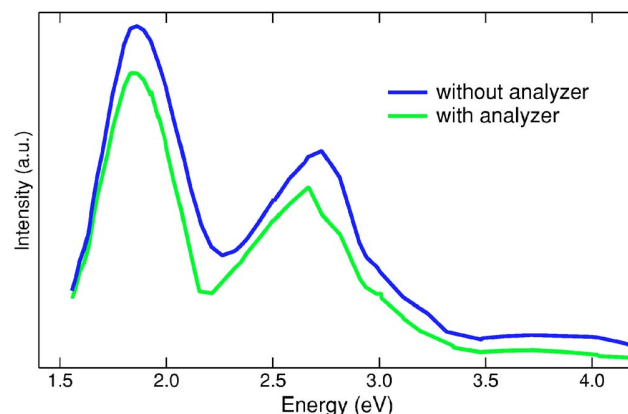


FIG. 8. Sensitivity of the UT-3 system as measured in optimal polarization direction (lower curve) and without the use of an analyzer (upper curve). Sensitivity is given in arbitrary units.

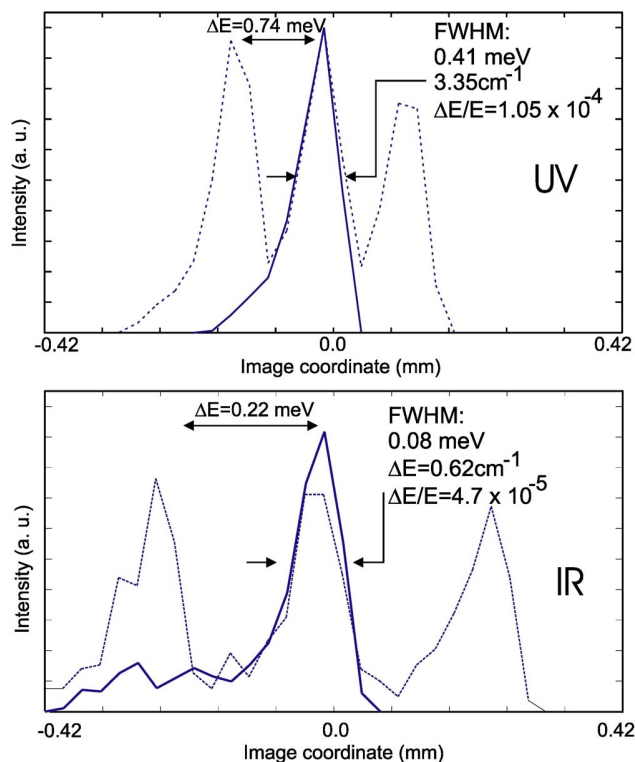


FIG. 9. Expected resolution function in subtractive mode for two different wavelengths in the UV and IR (315 and 750 nm, respectively). The size of the source for the simulations was set to  $25 \mu\text{m}$  at the entrance slit, thus yielding a spot size of  $4.3 \mu\text{m}$  at the sample, which is manageable with the optical setup. The numbers in the figure give information about the resolution at the simulated wavelengths and the ratio  $\Delta E/E$ .

duces laser spots on the sample smaller than  $5 \mu\text{m}$ . Together with the ability to close down the slits to  $25 \mu\text{m}$ , this enables us to achieve very good resolution over the entire wavelength range. The resolution of the UT-3 in subtractive mode was simulated by ray tracing. The outcome is displayed in Fig. 9. In the optimal system, a resolution of  $3 \text{ cm}^{-1}$  for the UV-grating set around 315 nm and a resolution of  $0.8 \text{ cm}^{-1}$  for the VIS-grating set around 750 nm is expected. For this simulation two wavelengths with known distance in energy space were ray traced. From their distance in real space, the FWHM of the wavelength could be calculated, yielding the resolution. The ray tracing was performed assuming a spot size at the entrance slit of  $25 \mu\text{m}$ . The software cannot model binning on a CCD; thus, the resolution is strongly underestimated when ray tracing larger slit widths. In Fig. 10 measurements from a neon lamp and a laser line are presented. These intrinsically sharp lines provide a good marker for the real resolution of the device. One neon line at 1.65 eV was analyzed showing that in the IR region the measured resolution is comparable to the simulated one. The laser line analyzed in the UV region was measured using a larger slit width. The resulting resolution of  $4.6 \text{ cm}^{-1}$  still resembles the expectation when taking the different slit widths into account.

Connected with the resolution is the stray light rejection. The UT-3 was designed to exhibit superior stray light rejection for Raman scattering. This is accomplished by setting the pass band of the premonochromator to block the laser

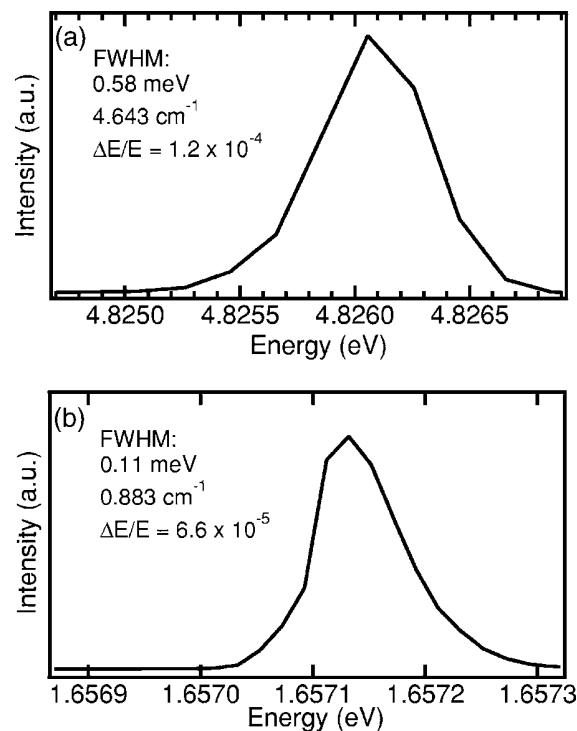


FIG. 10. Measured resolution function in subtractive mode for two different wavelengths. Spectral line in the UV is the frequency-doubled 514.5 nm argon laser line, spectral line in the IR is from a Ne lamp. (a) UV grating set, entrance slit width  $150 \mu\text{m}$ ; (b) VIS grating set, entrance slit width  $25 \mu\text{m}$ . The numbers in the figure give the energy resolution of the system and the ratio  $\Delta E/E$ .

line while passing the longer wavelength Raman-shifted light (for Stokes Raman scattering). Figure 11 depicts a simulation of stray light rejection. Here, one of the two ray traced wavelengths represents the elastically scattered laser light, the other an inelastic peak representing an inelastic light scattering process very close in wavelength and therefore in energy to the laser. The intensity ratio of laser to inelastic peaks is 100 to 1. In the inset of Fig. 11, it can be seen that the laser

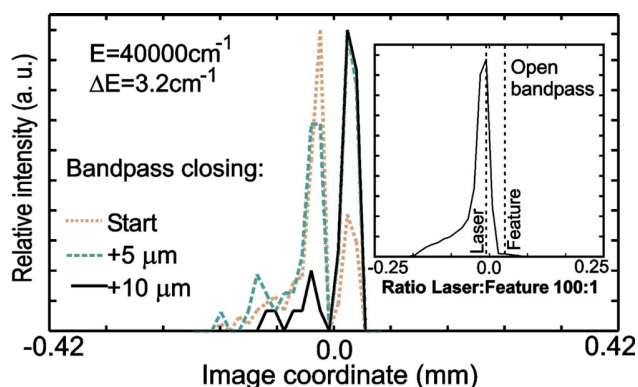


FIG. 11. Simulation of the stray light rejection of the UT-3 at nearly 5 eV. Two different energies representing the laser light (left) and a feature at  $3.2 \text{ cm}^{-1}$  are still separated. Once the slit blades are moved in so that the laser and the feature ratio has been modified from 100:1 down to 1:1 (Start value), moving the slit blades only  $10 \mu\text{m}$  further towards lower energies (half a pixel) suppresses the laser light completely. The inset shows the simulation with open pass band, where the feature is buried in the laser peak.

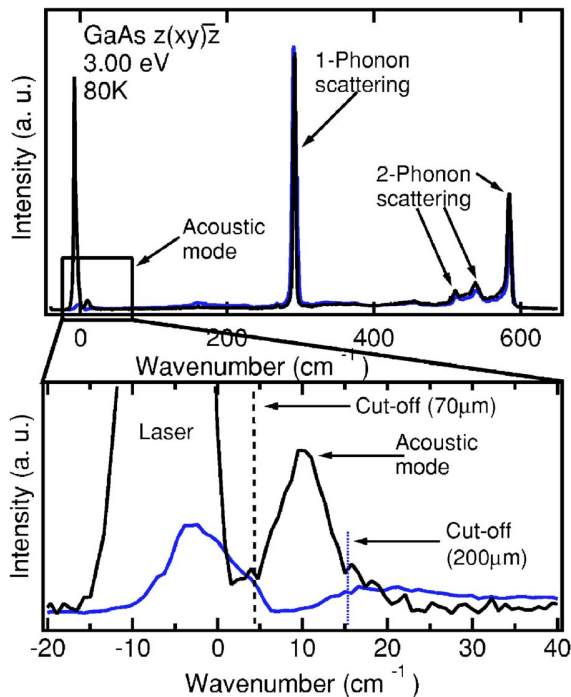


FIG. 12. Experimental results from a measurement on GaAs depicting the stray light rejection at 413 nm; rejection is better than  $5 \text{ cm}^{-1}$ . The vertical lines indicate the different cutoffs when closing the entrance slits and enlarging the pass band. The enlarged pass band reveals a new acoustic mode in the spectrum centered at around  $10 \text{ cm}^{-1}$ . The lower image also shows the change in shape and position of the laser line due to diffraction effects.

dominates the spectrum when the pass band lets both lines through without attenuation. Upon closing the pass band so that at the high energy end the laser line is partially blocked, we obtain the “Start” spectrum shown in the main part of the figure. Upon moving in the slit blades at entrance and exit slit of the premonochromator by only a few  $\mu\text{m}$ , it is seen that the laser line vanishes nearly completely. Due to image distortion effects occurring when blocking, the position and shape of the laser line changes slightly (see black curve). After closing the pass band, the laser line is seen to be suppressed, while the inelastic peak is undistorted and clearly visible. This simulation yielded stray light rejection to within about  $3 \text{ cm}^{-1}$  of the laser line in the deep-UV. When working with longer wavelengths, the gratings of the UT-3 have to rotate farther from normal incidence, thus increasing the coma in the focal spots. Therefore, due to the increase in spot size at the internal slits and the CCD-plane, stray light rejection is slightly degraded as one moves towards the IR. However, at the same time, the resolution is increased.

The experimentally measured rejection of stray light is illustrated in Fig. 12. The energy used for this experiment was 3 eV, which is close to one resonance of the GaAs sample. In this energy range, the instrument has a resolution of about two wave numbers. Here, a single crystal of GaAs was measured at 80 K twice on the same spot, once with standard sized slit widths,  $150 \mu\text{m}$  at the entrance slit, and  $200 \mu\text{m}$  at the intermediate slit, and once with small slit widths,  $50$  and  $70 \mu\text{m}$ . In the latter case, the laser is rejected better, thus enabling the edge of the pass band, which defines the cutoff, to be moved towards the laser line. At the same

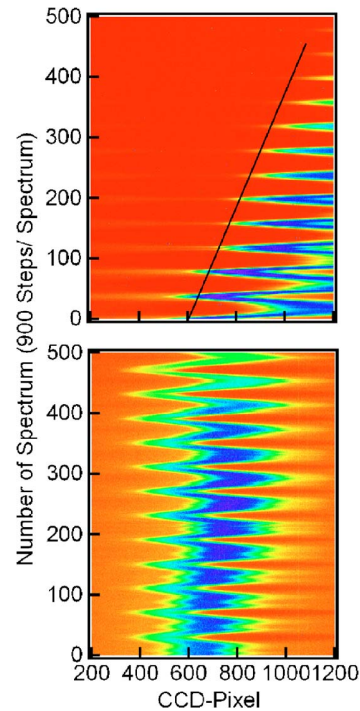


FIG. 13. (Color online) Coupling tests, gray scale coded, with intensity decreasing from dark to light. The  $x$  axes are the CCD-pixel numbers along the dispersion direction, the  $y$  axis shows different white light spectra where the pass band has been shifted by an energy range corresponding to 900 steps each. The top panel shows that without optimization the two monochromators lose their coupling immediately, not allowing to define starting windows. The solid line shows how the edges of the whitelight spectrum deteriorate fast. In this run, both mono No. 1 and No. 2 were each moved 900 steps. The bottom panel shows the improved coupling of the monochromators using a guessing routine. This routine calculates the number of steps mono No. 2 has to move as a function of the number of steps mono No. 1 is moving. The empirically determined correction factors in this guessing routine are:  $A=1.022$ ,  $B=140$ , and  $C=35\,240$ . The setting of the monochromators obtained by the guessing routine has to be optimized further using a calibrated white light lamp.

time, the shape of the laser line is disturbed due to edge diffraction effects at the slits. The measurement with small slit widths, allows an acoustic mode (Brillouin spectrum) to be seen in the spectrum, and the laser is rejected further compared to the measurements with larger slit openings. From this measurement, stray light rejection of about  $5 \text{ cm}^{-1}$  can be estimated, close to the simulated results. Also the change in shape and position of the laser line is comparable to that observed in the simulation.

#### IV. CALIBRATION OF WAVELENGTH DRIVES

The subtractive coupling of the UT-3 is not realized mechanically, but by software: The two monochromators No. 1 and No. 2 are not directly coupled. The control software must provide the subtractive coupling. Since the two grating rotation systems are mirrored, they differ in real movement when both are moved a certain number of steps. To be able to define spectral pass bands over a broad wavelength range, an optimization routine was developed to determine the number of steps of mono No. 2 as a function of the number of steps of mono No. 1.

Figure 13 shows two test runs, one before any optimiza-

tion, and one after creating a guessing routine. In these test runs, a white light source is imaged through the smallest possible entrance slit onto the CCD-camera. If the subtractive coupling of mono No. 1 and mono No. 2 is optimal and mono No. 3 is moved the doubled number of steps mono No. 1 has moved, then the highest intensity is found in the middle of the CCD. If the coupling is not optimal, the maximum shifts and decreases in intensity. For the test runs, 500 spectra were acquired, while between two spectra each monochromator was moved 900 steps. In order to move at least half of a pass band between two corresponding pass bands, a guessing routine was established which calculates the number of steps mono No. 2 has to move as a function of the number of steps mono No. 1 is moving. The guessing routine was empirically determined to be:

$$\Delta STS_{No.2} = A \Delta STS_{No.1} + B \sin\left(\frac{2\pi}{C} \cdot \Delta STS_{No.1}\right), \quad (15)$$

where  $\Delta STS_{No.1}$  and  $\Delta STS_{No.2}$  denote the number of steps mono No. 1 and No. 2 are moved. The correction parameters  $A$ ,  $B$ , and  $C$  were found to be optimal with the values of  $A=1.022$ ,  $B=140$ , and  $C=35\,240$ . This function can now be used to define a pass band. As the remaining decoupling effects would still lead to a significant decrease in the quality of the pass band, the optimal synchronization for each pass band must still be determined manually, by using a calibrated white light source. Due to the high repeatability of the monochromator repositioning, it is possible to define interconnected pass bands, which span the wavelength range from 207 to 800 nm. Spectral lines from neon lamps and lasers were used in most of these pass bands to calibrate the wavelengths. The wavelength scales for the pass bands were calculated by identifying the spectral lines from the literature and the gaps filled by interpolation. From this, a function for converting the known position of the spectrograph to a wavelength scale was deduced. One function and fitting parameter set was established for the VIS-grating set, and another for the UV-grating set.

## V. EXPERIMENTAL RESULTS

We will in this section show examples of data obtained with this setup. The needed optical corrections as obtained by spectral ellipsometry for an acquired Raman spectrum are shown in Fig. 14, using GaAs as an example. The sample was an MOCVD deposited film with a thickness of  $\approx 8\ \mu\text{m}$ . The lower regions of the film are most likely slightly strained due to the lattice constant mismatch with the substrate. As substrate, an undoped GaAs wafer was used. Figure 14 depicts the optical parameters and the resulting correction factor over an excitation energy range from 0.5 to 5.5 eV. Figure 14(a) shows the refractive index  $n$  and the absorption coefficient  $k$ , (b) the optical dielectric coefficients  $\epsilon_1$  and  $\epsilon_2$ . These coefficients can be determined using spectral ellipsometry. In this case, a modified SENTECH SE850 ellipsometer was used.<sup>16</sup> The optical constants are used to calculate the reflection coefficient as well as the penetration depth, shown in (c) and (d). Using Eq. (13), Fig. 14(e) was calculated to visualize the correction due to the solid angle. The

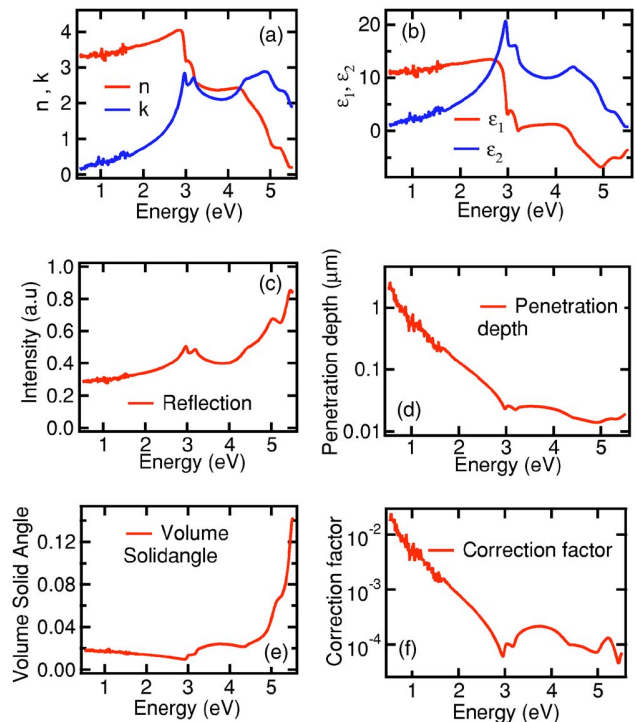


FIG. 14. Optical data obtained by spectral ellipsometry of GaAs at 80 K over an energy range from 0.5 to 5.5 eV; (a) refractive index  $n$  and absorption coefficient  $k$ ; (b) optical dielectric constants  $\epsilon_1$  and  $\epsilon_2$ ; (c) calculated transmission coefficient; (d) penetration depth; (e) solid angle; (f) resulting correction factor.

resulting overall Raman correction factor is depicted in Fig. 14(f), with which the Raman spectra must be divided when performing resonance studies at different excitation energies. Comparing this correction factor with the penetration depth, one can clearly see that the solid angle needs to be included, especially beyond 3 eV. In this energy range, most solids start to show a stronger absorption, as shown by a decreasing penetration depth. At the same time, the solid angle is starting to increase due to the higher values of  $k$ .

An example of resonance Raman study on the GaAs-sample is presented in Fig. 15, showing in the left panel Raman spectra acquired at different energies.

The spectra were corrected for the spectral response of the entire system, then the correction factor corresponding to the excitation wavelength was applied. The right panel shows the resulting resonance behavior of the phonon modes in the photon energy region from 2.5 to 5.2 eV. The intensity is taken from the spectrum and then multiplied by the correction factor, which can be found in Fig. 14(f). Figure 15(a) illustrates resonant Raman scattering measurements on GaAs. The Brillouin zone center longitudinal optic ( $LO_{\Gamma}$ ) phonon ( $\approx 295\ \text{cm}^{-1}$ ) and its overtone ( $\approx 590\ \text{cm}^{-1}$ ) can be seen from the figure. Fig. 15(b) displays the intensity of the ( $LO_{\Gamma}$ ) phonon versus the excitation energy. It can easily be seen, that the resonance curve resembles quite well the behavior of  $\epsilon_2$ , which is also plotted in Fig. 15(b) (solid line). More details can be found in Ref. 17. We also performed a resonance Raman study on  $\text{LaMnO}_3$ , investigating the orbital ordering occurring below 800 K in this compound, through the resonance of the photons with an orbital exciton. There

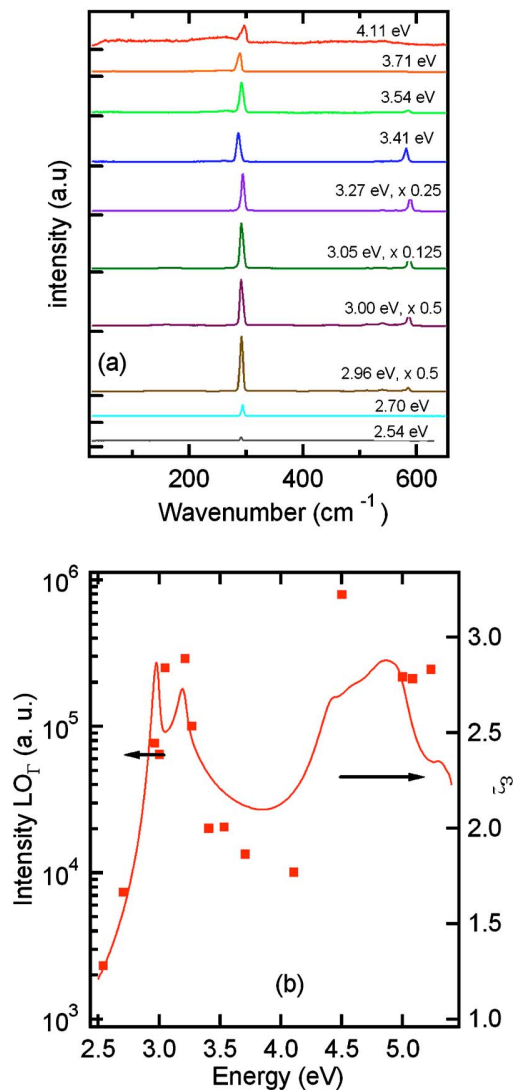


FIG. 15. Experimental results of resonance Raman measurements on GaAs, showing (a) corrected Raman spectra acquired using different excitation energies, and (b) the analysis of the intensity of the LO<sub>Γ</sub> phonon at  $\approx 295$  cm<sup>-1</sup> (square symbols) as a function of incident photon energy together with  $\epsilon_2$  (solid line).

are predictions showing a strong matrix element of the one and especially the two phonon process that are based on the Franck-Condon mechanism.

In Fig. 16 we present inelastic light-scattering spectra for incident photon energies from 1.97 to 4.40 eV, in the one phonon spectral range (a). Figure 16 shows for previously used incident photon energies (1.97 and 2.34 eV) the well-known phonon modes of  $A_g$  and  $B_{2g}$  symmetry originating from the Jahn-Teller distortion. At lower energies between 200 and 400 cm<sup>-1</sup> the spectra show strong signal from the rotational modes  $A_g(2)$ , an in-phase  $y$  rotation at 257 cm<sup>-1</sup>, and an out-of phase  $x$  rotation  $A_g(4)$  at 284 cm<sup>-1</sup>. Both modes show weak signal with visible excitation energies and strong resonance enhancements for deep-UV excitation, clearly supporting their assignment as rotational vibrations. There is the appearance of an additional mode in the deep

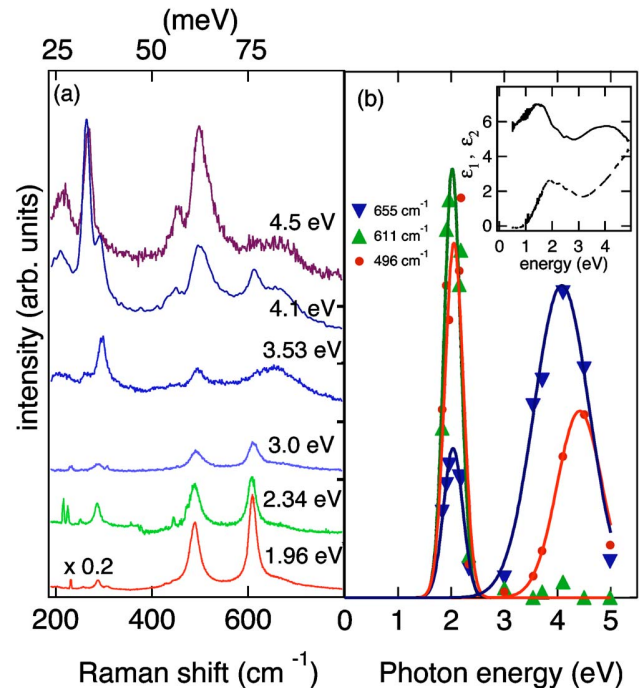


FIG. 16. (a) Experimental spectra showing the oxygen vibrations of the distorted MnO<sub>6</sub> octahedra in the one-phonon region; (b) resonance profiles of the one-phonon excitations. The inset in (b) shows  $\epsilon_1$  (solid line) and  $\epsilon_2$  (dashed line). Reprinted figure with permission from R. Krüger, B. Schulz, S. Naler, R. Rauer, D. Budelmann, J. Bäckström, K.H. Kim, S.-W. Cheong, V. Perebeinos, and M. Rübhausen, Phys. Rev. Lett. 92, 097203 (2004). Copyright 2004 by the American Physical Society.

UV around 450 cm<sup>-1</sup> (4.10 and 4.49 eV) that has not been observed before and that shows an analogous resonance behavior to the rotational modes. The higher-energy oxygen modes are observed between 496 and 655 cm<sup>-1</sup>. Especially, the  $B_{2g}(1)$  mode at 611 cm<sup>-1</sup>, an in-phase stretching mode, shows a single pronounced resonance at around 2 eV as it strongly modulates the Jahn-Teller levels and the orbital ordering. Phonons around 496 and 655 cm<sup>-1</sup> resonate towards 2 and 4.4 eV [see Fig. 16(b)]. This strongly suggests that the 496 cm<sup>-1</sup> phonon is not a pure rotational or bending mode of the oxygen cage but rather related to the  $A_g(1)$  in-phase stretching mode and that the new mode at 450 cm<sup>-1</sup> is most probably the bending  $A_g(3)$  vibration.<sup>18</sup>

Our main findings are: (i) the one- and two-phonon excitation spectrum shows sharp resonances for incident photon energies close to the JT gap at 2 eV and at the charge-transfer gap at 4.4 eV; (ii) the one-phonon spectrum shows resonance profiles that are strongly dependent on the symmetry of the involved phonon modes. It also contains a vibrational oxygen breathing mode at 655 cm<sup>-1</sup> (81 meV) that resonates strongly at the charge-transfer gap. Phonon modes at 611 cm<sup>-1</sup> (76 meV) and at 496 cm<sup>-1</sup> (62 meV) show their strongest resonance at the Jahn-Teller gap; (iii) these three phonon modes at 496, 611, and at 655 cm<sup>-1</sup> with their individual resonance properties yield a complicated two-phonon spectrum between 1100 and 1300 cm<sup>-1</sup>. For more details regarding this results, consult Ref. 9.

**ACKNOWLEDGMENTS**

The authors acknowledge many stimulating discussions with U. Merkt. We are supported by DFG Ru773/2-2, Ru773/2-3, GrK "Physik nanostrukturierter Festkörper."

- <sup>1</sup>M. Rübhausen, C. T. Rieck, N. Dieckmann, K.-O. Subke, A. Bock, and U. Merkt, *Phys. Rev. B* **56**, 14797 (1997).
- <sup>2</sup>M. Rübhausen, P. Guptasarma, D. G. Hinks, and M. V. Klein, *Phys. Rev. B* **58**, 3462 (1998).
- <sup>3</sup>P. Arboleda and G. R. Loppnow, *Anal. Chem.* **72**, 2093 (2000).
- <sup>4</sup>Z. Huang, A. McWilliams, H. Lui, D. I. McLean, S. Lam, and H. Zeng, *Int. J. Cancer* **107**, 1047 (2003).
- <sup>5</sup>W. Schabel, I. Ludwig, and M. Kind, *Drying Technol.* **22**, 285 (2004).
- <sup>6</sup>S. E. J. Bell, D. T. Burns, A. C. Dennis, and J. S. Speers, *Analyst (Cambridge, U.K.)* **125**, 541 (2000).
- <sup>7</sup>A. S. Wilson, H. G. M. Edwards, D. W. Farwell, and R. C. Janaway, *J. Raman Spectrosc.* **30**, 367 (1999).
- <sup>8</sup>S. Yoon, M. Rübhausen, S. L. Cooper, K. H. Kim, and S.-W. Cheong, *Phys. Rev. Lett.* **85**, 3297 (2000).
- <sup>9</sup>R. Krüger, B. Schulz, S. Naler, R. Rauer, D. Budelmann, J. Bäckström, K. H. Kim, S.-W. Cheong, V. Perebeinos, and M. Rübhausen, *Phys. Rev. Lett.* **92**, 097203 (2004).
- <sup>10</sup>A. M. Shvaika, O. Vorobyov, J. K. Freericks, and T. P. Devereaux, *Phys. Rev. Lett.* **93**, 137402 (2004).
- <sup>11</sup>A. Pinczuk and E. Burstein, in *Light Scattering in Solids*, edited by M. Cardona (Springer, Berlin, 1982), Vol. I.
- <sup>12</sup>M. V. Klein, in *Light Scattering in Solids*, edited by M. Cardona and G. Güntherodt (Springer, Berlin, 1982), Vol. III.
- <sup>13</sup>G. D. Mahan, *Many-Particle Physics* (Kluwer Academic, New York, 2000).
- <sup>14</sup>M. V. Klein and T. E. Furtak, *Optics* (Wiley, New York, 1986); *Optik* (Springer, Berlin, 1988).
- <sup>15</sup>S. Ostertun, Ph.D. thesis, University of Hamburg, ISBN 3-8265-8701-4 2001.
- <sup>16</sup>R. Rauer, G. Neuber, J. Kunze, J. Bäckström, and M. Rübhausen, *Rev. Sci. Instrum.* **76**, 023910-1 (2005).
- <sup>17</sup>S. Yoon, J. F. Geisz, S.-H. Han, A. Mascarenhas, M. Rübhausen, and B. Schulz, *Phys. Rev. B* **71**, 155208 (2005).
- <sup>18</sup>M. N. Iliev, M. V. Abrashev, H.-G. Lee, V. N. Popov, Y. Y. Sun, C. Thomsen, R. L. Meng, and C. W. Chu, *Phys. Rev. B* **57**, 2872 (1998).



# Chapter 4

## Experimental results and discussion on $\text{LaMnO}_3$

### 4.1 Dielectric function of $\text{LaMnO}_3$

Fig. 4.1 displays the dielectric function of the  $\text{LaMnO}_3$  sample, which we have determined by spectroscopic ellipsometry. It shows an insulating response with an energy gap of 1.8 eV. As in the dielectric function different absorption levels (3 bumps beginning at  $\sim 2$  eV and an increasing edge at  $\sim 4$  eV) can be observed, we have used different laser excitation energies starting at 676 nm down to 248.3 nm (see colored vertical lines and section 3.7) for all specific absorption levels. This is in contrast to the excitation energy - excitation wavelength respectively - typically used for Raman measurements: 514 nm, which is between two different absorption levels and does not reveal the (Raman) matrix element.

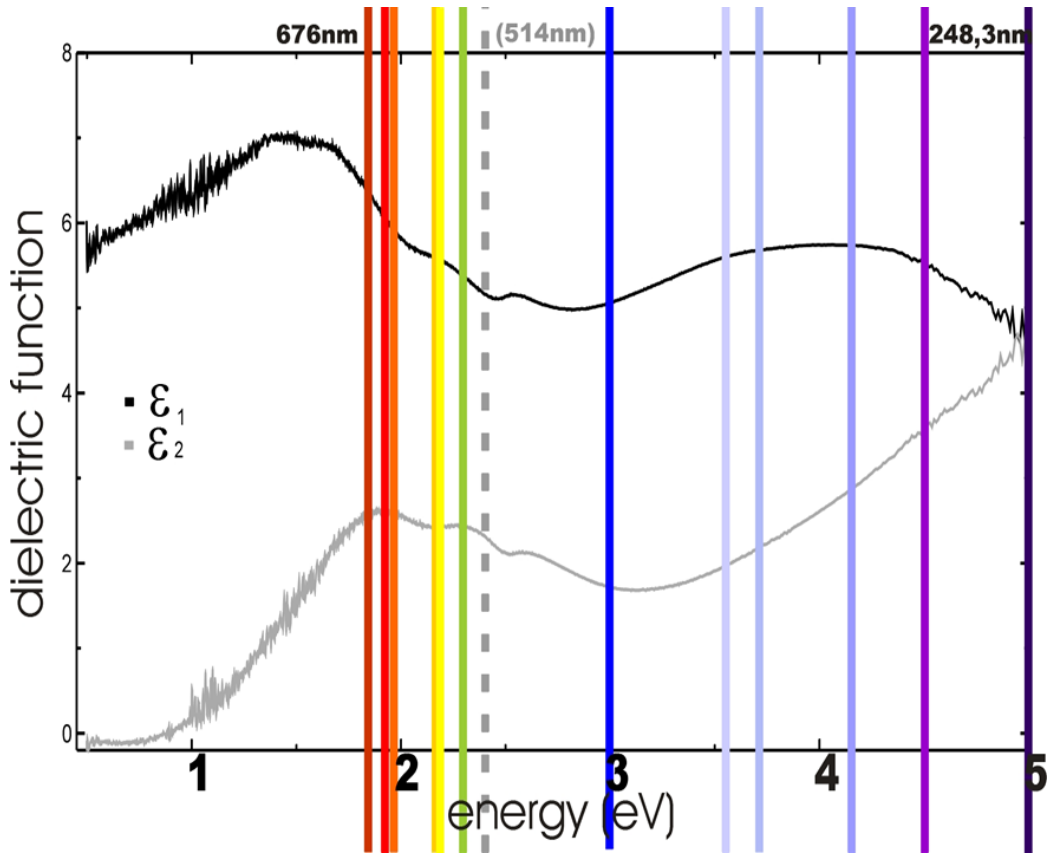


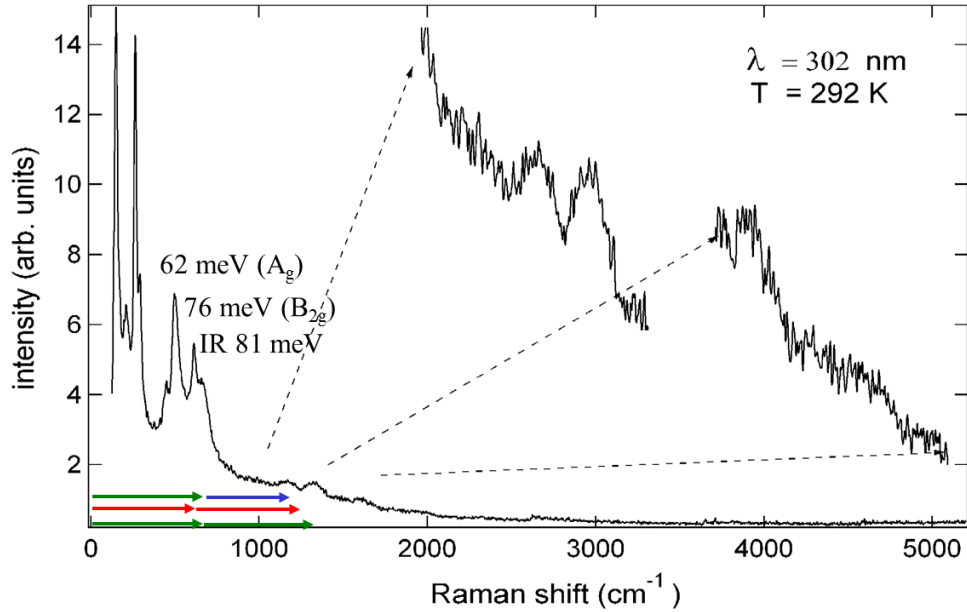
**Figure 4.1:** Dielectric function of  $\text{LaMnO}_3$  measured with spectral ellipsometry. Colored vertical lines indicate the Raman excitation wavelengths we have applied for the resonance Raman scattering study.

## 4.2 Raman spectra of $\text{LaMnO}_3$ and phonon mode assignment

In Fig. 4.2 one Raman spectrum measured at 302 nm excitation wavelength in the UV and at room temperature is depicted exemplarily. We assign the phonon modes related to the oxygen octahedra in the following way:

- 257  $\text{cm}^{-1}$  mode  $\equiv A_g(2)$  in-phase y-rotation
- 284  $\text{cm}^{-1}$  mode  $\equiv A_g(4)$  out-of-phase x-rotation
- 448  $\text{cm}^{-1}$  mode  $\equiv A_g(3)$  out-of-phase bending
- 496  $\text{cm}^{-1}$  mode  $\equiv A_g(1)$  in-phase stretching
- 611  $\text{cm}^{-1}$  mode  $\equiv B_{2g}(1)$  in-phase stretching

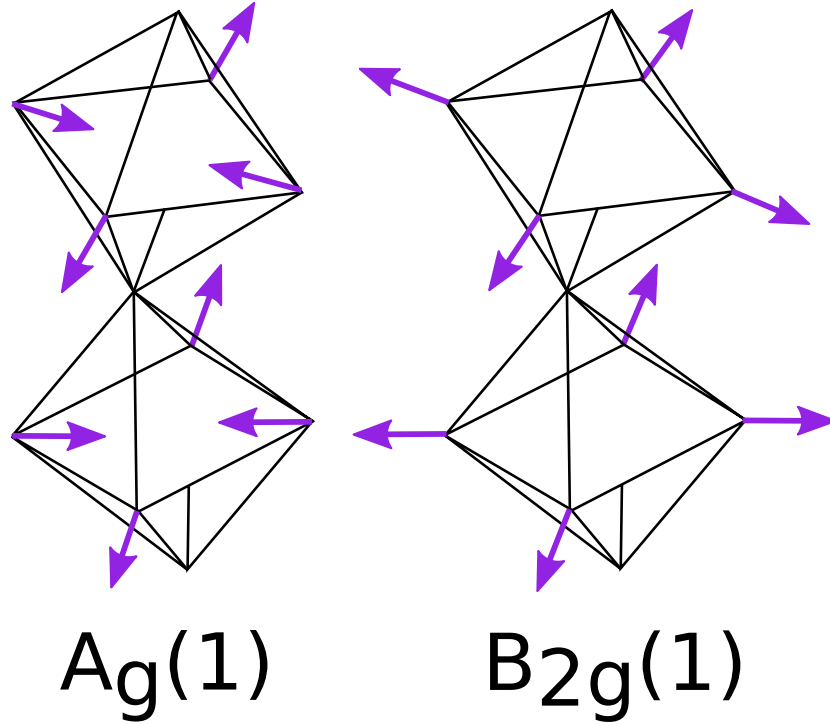
#### 4.2. RAMAN SPECTRA OF LAMNO<sub>3</sub> AND PHONON MODE ASSIGNMENT 89



**Figure 4.2:** LaMnO<sub>3</sub> Raman spectrum measured at 302 nm excitation wavelength and room temperature. Second- and third-order Raman modes are zoomed up for clarity and different mixing combinations of the one-phonon modes are indicated by red (associated with the 76 meV mode), blue (associated with the 62 meV mode) and green (associated with the 81 meV mode) arrows.

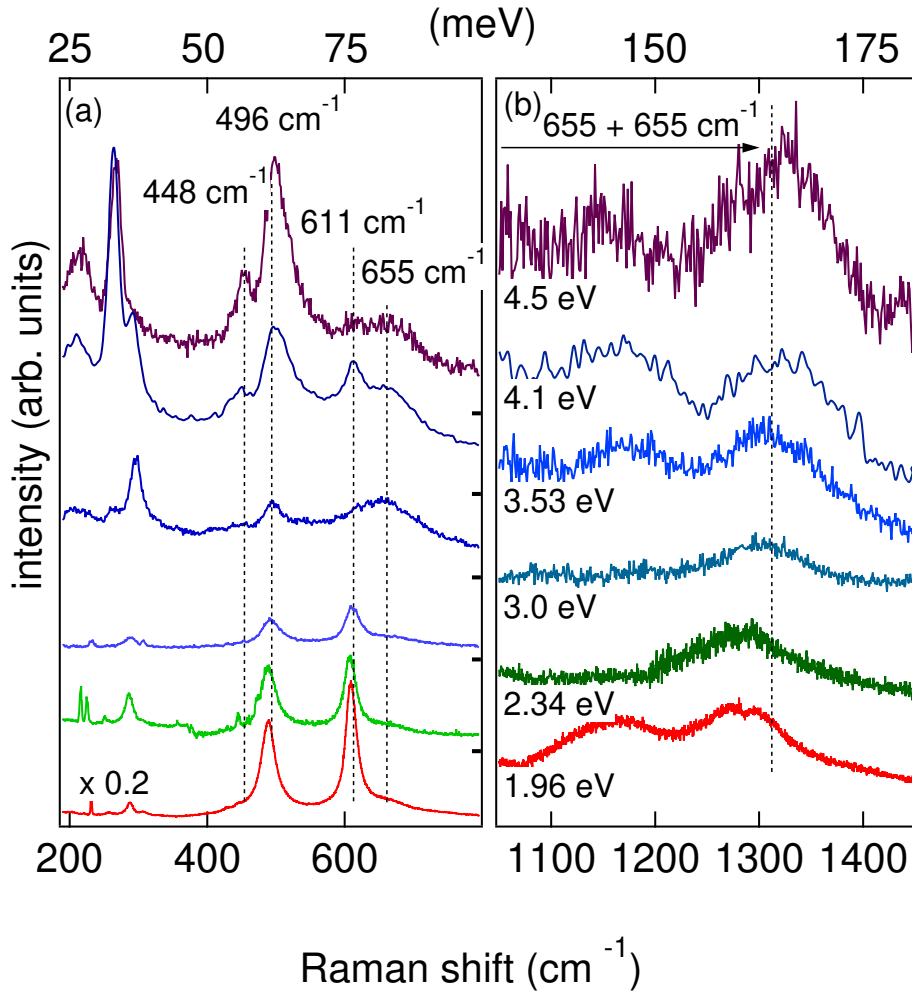
655 cm<sup>-1</sup> mode  $\equiv$  normally IR active vibrational oxygen breathing mode

All modes are consistent with lattice dynamics calculations by Iliev and coworkers [15]. The assignment of the experimentally observed 496 cm<sup>-1</sup> mode, however, differs in our interpretation due to the newly seen 448 cm<sup>-1</sup> mode in the UV. The JT modes e.g., which can be related to the possible JT lattice distortions Q<sub>2</sub> and Q<sub>3</sub> due to their similar oscillation behavior (see figure 4.3), show analog resonances in the Raman spectra. These resonance properties can be helpful in the mode assignment. As the 257 cm<sup>-1</sup> and the 284 cm<sup>-1</sup> rotational modes show weak signal with visible excitation energies (see figure 4.4) and strong resonance enhancements for deep-UV excitation, they reflect the resonance behavior of the new 448 cm<sup>-1</sup> mode. The B<sub>2g</sub>(1) in-phase stretching mode at 611 cm<sup>-1</sup>, however, resonates exclusively at around 2 eV as it strongly modulates the Jahn-Teller levels resulting in the conclusion that the 448 cm<sup>-1</sup> mode is no JT mode but most probably the A<sub>g</sub>(3) out-of-phase bending mode, which was previously associated with the 496 cm<sup>-1</sup> mode. This 496 cm<sup>-1</sup> mode on the other hand resonates also



**Figure 4.3:** Phonons of different symmetry found in  $\text{LaMnO}_3$ :  $A_g(1)$  in-phase stretching phonon mode (adapted from: [15]) associated with the  $Q_2$ -distortion and  $B_{2g}(1)$  in-phase stretching phonon mode (adapted from: [15]) associated with the  $Q_3$ -distortion. Arrows indicate the oscillations of the oxygen atoms of the octahedra.

at 2 eV, suggesting its assignment to a JT  $A_g(1)$  in-phase stretching mode. We pay the main attention in our analyzes to the normally infrared active, but in this case disorder induced 655 wavenumbers mode (81 meV) as well as to the JT modes at  $496 \text{ cm}^{-1}$  (62 meV) and  $611 \text{ cm}^{-1}$  (76 meV). We are also able to see higher order phonon modes that correspond to the energy range between  $1100$  and  $1300 \text{ cm}^{-1}$  (see figures 4.2 and 4.4). Second- and third-order phonons are shown in Fig. 4.2 - zoomed up for clarity. The multiphonon peaks can be achieved by different combinations of the one-phonon peaks. A possible two-phonon peak resulting from two  $611 \text{ cm}^{-1}$  (76 meV) phonons could arise at the second red arrow, while a mixing of the  $496 \text{ cm}^{-1}$  (62 meV) and the  $655 \text{ cm}^{-1}$  (81 meV) mode may lead to a two-phonon peak at the end of the combined green and blue arrow (at about  $1150 \text{ cm}^{-1}$ ). The peak at about  $1310 \text{ cm}^{-1}$  affirms that the disorder induced  $655 \text{ cm}^{-1}$  mode cannot be neglected as it might be a combination of two of these modes.

4.3 Resonances of  $\text{LaMnO}_3$ 

**Figure 4.4:**  $\text{LaMnO}_3$  Raman spectra in dependence of the incident photon energy (depicted by different colors): (a) First-order phonon modes. (b) Second-order phonon modes (zoomed up 10 times).

Raman spectra of each excitation energy range measured at  $\text{LaMnO}_3$  are depicted in figure 4.4. They are corrected for the wavelength dependent penetration depth and reflection coefficient as determined by the dielectric function. Fig. 4.4a shows the first-order phonon mode region and figure 4.4b the second-order phonon mode region zoomed up 10 times for clarity. Each spectrum is measured with a different excitation wavelength between 1.96 eV (red) and 4.5 eV (deep UV). Some resonances of the already before discussed modes can be observed: The 496  $\text{cm}^{-1}$  mode, for example, resonates in the

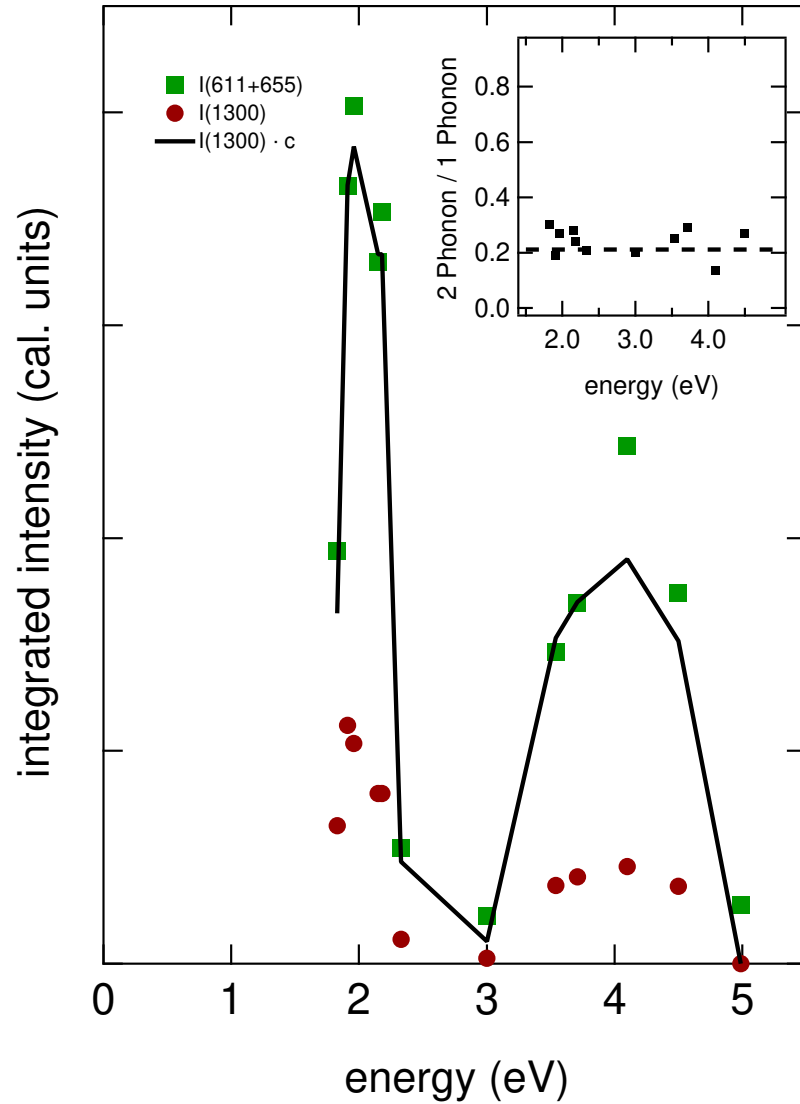
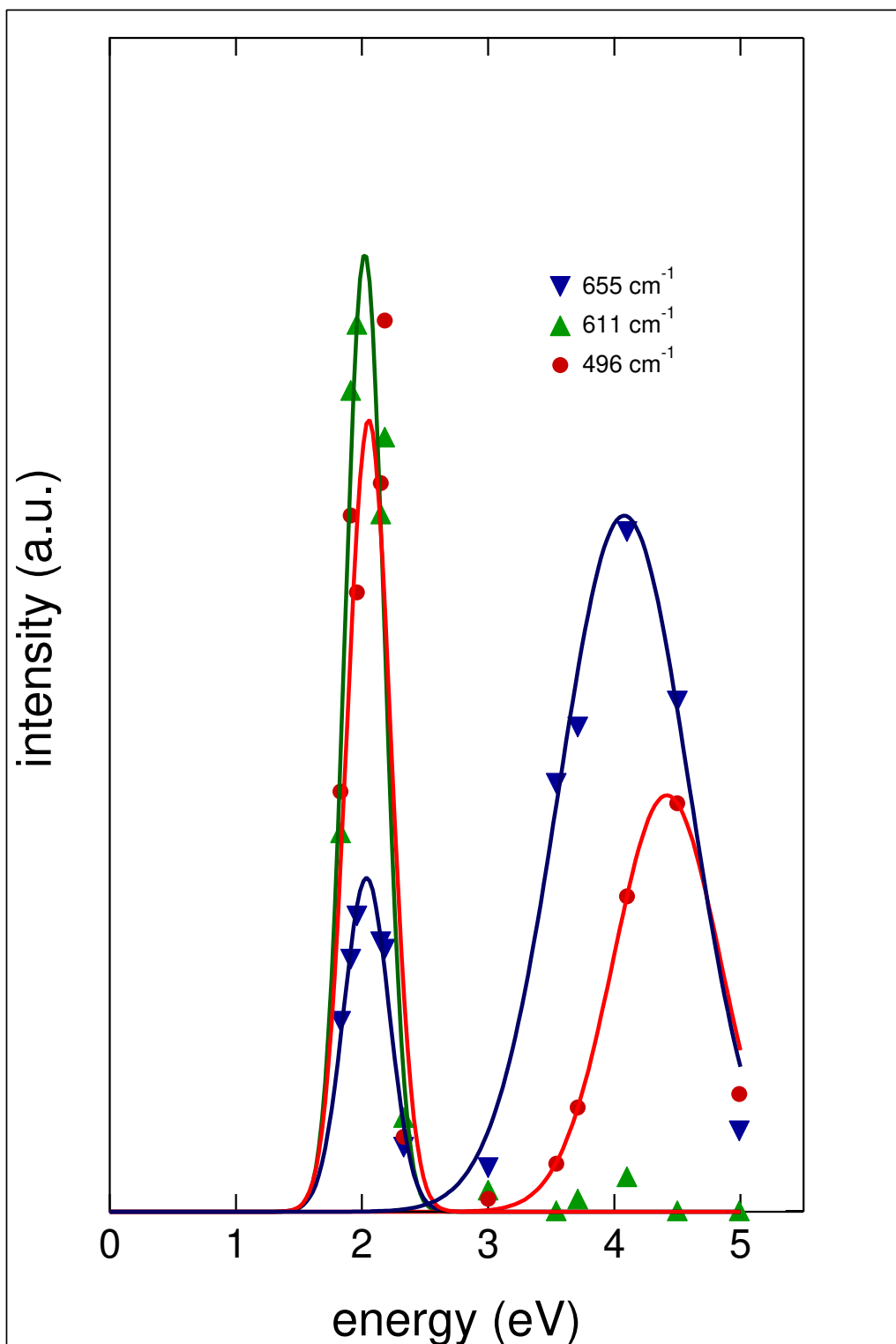


**Figure 4.5:** One- and two-phonon excitation profiles (integrated intensities over the laser excitation energy) of the combined  $611\text{ cm}^{-1}$  and  $655\text{ cm}^{-1}$  first-order phonon modes (green squares) and the peak at  $1300\text{ cm}^{-1}$  in the two-phonon region (red circles). The black curve depicts the excitation profile of the two-phonon region multiplied by a factor of 4.166. The nearly constant relation between the two- and one-phonon intensities in dependence of the excitation energy is shown in the inset.

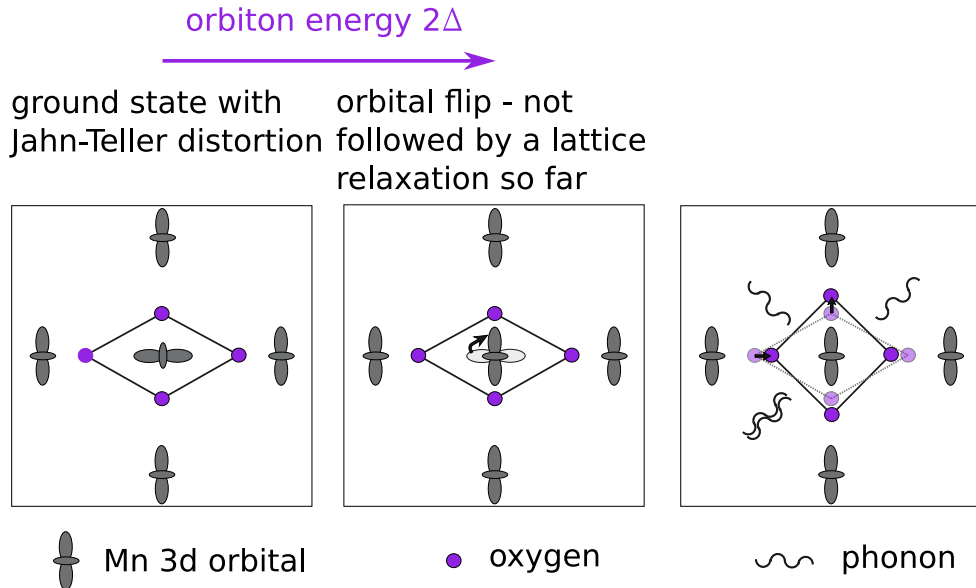
red excitation region but also in the deep UV, and the  $611\text{ cm}^{-1}$  mode shows a clear resonance in the red. The disorder induced  $655\text{ cm}^{-1}$  mode exhibits resonant behavior towards the UV. There equally is a resonance behavior in the second-order phonon region (see figure 4.4b). The dashed line is positioned at the doubled energy of the  $655\text{ cm}^{-1}$  mode. The peak occurring there might be a mixing of the  $611\text{ cm}^{-1}$  and  $655\text{ cm}^{-1}$  modes. This assumption is strengthened by the resonance behavior already discussed for the first-order phonon modes. A shifting of the maximum peak position of this second order peak can be observed towards higher energies (Raman shifts) in the deep UV (excitation energy range) and towards lower energies in the red, reflecting the behavior of the first-order phonon modes. This resonance behavior gives a further hint that an orbiton assignment of the  $1310\text{ cm}^{-1}$  peak might not hold as a mixing of the  $611\text{ cm}^{-1}$  and the  $655\text{ cm}^{-1}$  modes is also indicated. The resulting one- and two-phonon excitation profiles are depicted in figure 4.5. All phonons have been fitted with a gaussian shape. Their integrated intensities are displayed in dependence of the incident laser energy. The added intensities of the two highest energy oxygen modes - the  $611\text{ cm}^{-1}$  and  $655\text{ cm}^{-1}$  modes - are shown as green squares. These are compared to the intensities of the mode at  $\sim 1300\text{ cm}^{-1}$ , displayed as red circles. Both intensities (combined first-order phonon intensities and the intensity of the peak at  $\sim 1300\text{ cm}^{-1}$ ) have the same characteristics, so that the  $1300\text{ cm}^{-1}$  peak intensities have been multiplied with a constant factor of 4.166 resulting in a convincing match of the one- and scaled two-phonon intensities. The black curve in comparison with the green squares demonstrates this as well as the inset of figure 4.5. The relation between the  $1300\text{ cm}^{-1}$  and the combined one-phonon intensities displayed there is constant in terms of the incident energy. In comparison to the results of Cardona and his group (see section 3.4) [48], this can be seen as a direct evidence that the  $1300\text{ cm}^{-1}$  peak is a two-phonon mode due to the Raman activity of the symmetry-broken IR mode at  $655$  wavenumbers and no orbiton.

In figure 4.6 the resonance profiles (phonon intensities in dependence of the excitation energy of the laser) of the three different previously discussed phonons (at  $496$ ,  $611$  and  $655$  wavenumbers) are depicted. Two characteristic resonance levels at  $2.05\text{ eV}$  and  $4.2\text{ eV}$  are evident. This matches quite well the dielectric function we have measured before. Compared to the absorption levels we have found there, we see that the phonons couple only with two of them. One is at around  $2\text{ eV}$  and the other one is lying in the increasing area of the dielectric function around  $4\text{ eV}$ . All three one-phonon modes resonate at the same energy of  $2.05\text{ eV}$  with FWHM of  $0.65\text{ eV}$ , derived from a fit of a gaussian profile. At the second level also the  $496\text{ cm}^{-1}$  and the  $655\text{ cm}^{-1}$

modes resonate with slightly shifted energies, but with the same width of resonance of 1.32 eV. This shift could be due to symmetry-dependent effects of the matrix elements or due to the presence of additional CT processes such as a combination of O p to Mn d (crystal field splitting) and Mn d to nearest neighbor Mn d transitions (correlations). The  $655 \text{ cm}^{-1}$  mode resonates more strongly to the 4.2 eV level, which we relate to the charge-transfer energy. As all Jahn-Teller modes resonate at around the 2 eV gap, we assign this energy to the Jahn-Teller splitting. For this reason, we expect an orbiton excitation connected to this 2 eV gap.



**Figure 4.6:** One-phonon excitation profiles displaying the magnitude of coupling of the  $496 \text{ cm}^{-1}$ ,  $611 \text{ cm}^{-1}$  and the  $655 \text{ cm}^{-1}$  mode to the specific excitonic states of  $\text{LaMnO}_3$  ( $2.05 \text{ eV}$  and  $\sim 4 \text{ eV}$ ).

4.4 Franck-Condon mechanism in  $\text{LaMnO}_3$ 

**Figure 4.7:** Flip of the  $\text{LaMnO}_3$  3d orbital from the orbitally ordered and JT distorted ground state, excited with the orbiton energy of  $2\Delta$ . This process is followed by a lattice relaxation later.

The exclusion of the  $1300\text{ cm}^{-1}$  peak as an orbiton is followed by the question where else orbitons can be expected. Within the theory [3, 47] that the orbiton is a flipping of the orbital as it is shown in figure 4.7 from the Jahn-Teller distorted ground state to the orbiton state (orbital exciton), the orbiton should have an energy of  $2\Delta$ , the Jahn-Teller splitting energy, as it restores the degeneracy of the  $e_g$  state. This can be understood looking at the oxygen displacements: from the orbitally ordered and JT distorted ground state the orbital flips (after an excitation of energy  $2\Delta$ ), which is not followed by a lattice relaxation so far in the intermediate step. Later the oxygen octahedron relaxes automatically involving enhanced one- or multi-phonon excitations.

Based on the Franck-Condon mechanism (see section 2.3), Vasili Perebeinos and Philip Allen have developed a theory for the orbiton [47]. In the orbitally

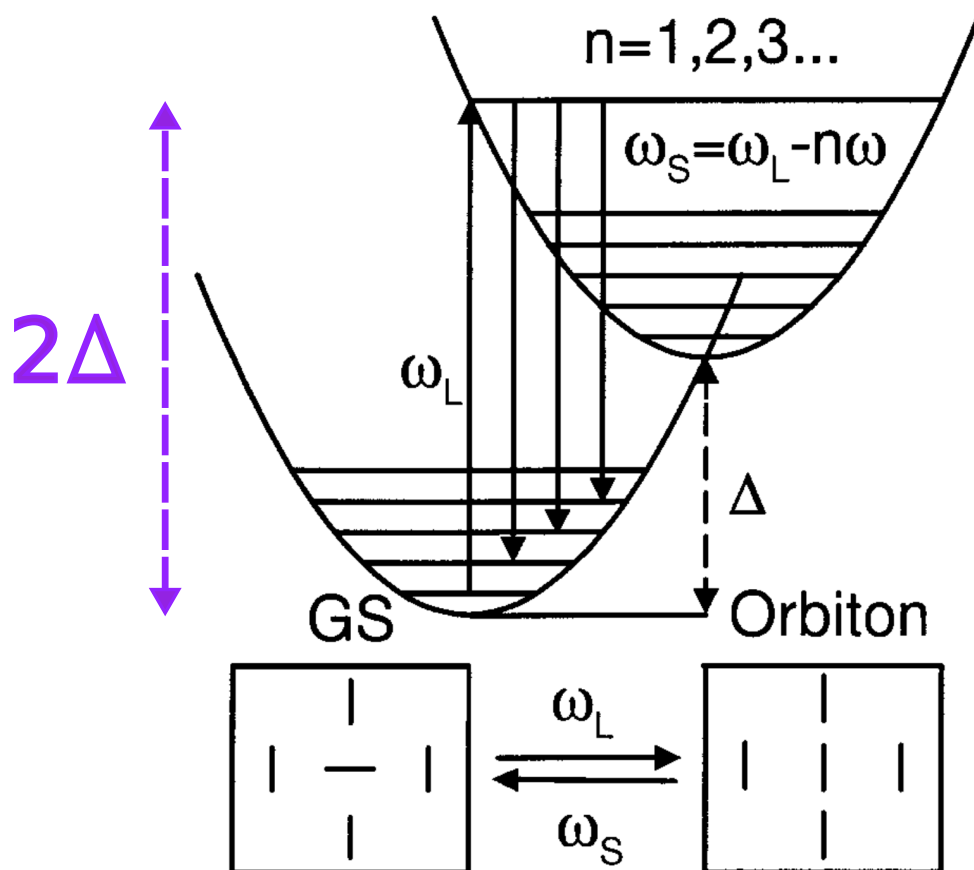


**Figure 4.8:** Shifted oscillator potentials allow for enhanced one- and multiphonon excitations within the Franck-Condon mechanism with an excitation energy of  $2\Delta$ . An orbital flip (orbiton excitation) is depicted in the lower row (adapted from [47]).

ordered ground state, the oscillator potentials of the ground and excited state of the 3d orbital of the manganese atom are displaced relatively to each other in dependence of a (strong) electron-phonon coupling. Diagram 4.8 illustrates that only one electron excitation process into one vibronic state of the upper oscillator potential with an energy difference of  $2\Delta$  due to the JT splitting is needed to excite multiphonon processes automatically. Therefore, the Raman scattering process is only proportional to one  $g$  (the electron-phonon coupling constant) instead of  $g^{2n}$  in the conventional process and allows for enhanced one- and multiphonon scattering simultaneously. The amplitude for ending in a vibrationally excited state (in the upper - or lower oscillator potential after decaying back into the orbital ground state) is for this

reason mainly determined by displaced oscillator overlap integrals. Different phononic or other excitations can be created this way and by this definition also an orbiton as it is depicted in Fig. 4.8 again as a flip of an orbital in the orbitally ordered state. As the oxygen octahedron rearranges after this orbital flip, a Frenkel exciton that is selftrapped is produced. Selftrapping is a requirement for the FC mechanism in solid states as in contrast to small molecules, electronic excited states in solids are often delocalized, eliminating multiphonon sidebands due to the FC effect [3].

## 4.5 Franck-Condon mechanism in LaMnO<sub>3</sub> - model calculations

Furthermore, a detailed quantitative derivation of the resonant multiphonon Raman cross section in the orbitally ordered ground state with a cooperative  $Q_2$ -type oxygen distortion has been given by Perebeinos and Allen [47] [private communication with Vasili Perebeinos, 2003] with a net result:

$$\frac{\partial^2 R_{\alpha\beta}^n}{\partial\omega_R\partial\Omega} = \sigma_0(\gamma_\alpha p_\alpha \gamma_\beta p_\beta)^2 S_{\alpha\beta}^n \delta(\omega_R - n\omega) \quad (4.1)$$

$$S_{\alpha\beta}^n = \frac{\omega_S^2}{\omega_L^2} \left| \sum_{m=0}^{\infty} \frac{\hbar\omega A_{\alpha\beta}^n(m)}{\Delta + m\hbar\omega - \hbar\omega_L + i\gamma_m} + \text{NRT} \right|^2 \quad (4.2)$$

$$A_{\alpha\beta}^n(m) = \sum_{\{m'\}} \delta(m - N\{m'\}) \langle n|u_\alpha + u_{-\alpha}|m'\rangle \langle m'|u_\beta + u_{-\beta}|0\rangle, \quad (4.3)$$

where  $\sigma_0 = r_e^2$  is the Compton cross section ( $r_e = e^2/m_e c^2$ ). The summation goes over all electronic states  $i$  and all the corresponding vibrational quanta  $\{m\}$ .  $N\{m\} = m_x + m_y + m_z + m_{-x} + m_{-y} + m_{-z}$  is the total number of vibrational quanta of the six neighboring oxygens.  $NRT$  describes the nonresonant term. To model the damping term  $\gamma_m$  of vibrational level  $m$ , the expression  $\gamma_m = \gamma_0 \sqrt{m+1}$ , as in a sequence of convolved Gaussians, intended to mimic the local densities of phonon states on oxygen atoms was used. The induced dipole matrix elements  $\gamma p$  and displacements  $u$  are measured in units of  $(m_e M \omega^2)^{1/2}$  and  $\sqrt{\hbar/M\omega}$  respectively. The ground state couples to excited electronic states by the electron-radiation Hamiltonian ( $\hat{p} \cdot \vec{A}$ ) responsible for resonant Raman scattering. It has been suggested [3, 47] that this transition becomes allowed because of asymmetric oxygen fluctuations. Another possibility for these d-d transitions to become activated is by static disorder of the oxygen octahedra or a quasi-elastic contribution. The electronic contribution to the dipole matrix element is described by the phenomenological parameter  $\gamma_\alpha p_\alpha$  (considering an orbital mixing with p character to allow the otherwise forbidden d-d transition [47]), and phonons contribute to the vibrational overlaps  $A_{\alpha\beta}^n$  (see equation 4.3). In their previous work [47], the symmetry of the excited phonon in the final state was not taken into account. Here they allow the final state  $|0, n\rangle$  to have an electronic ground state plus  $n$  vibrational ( $A_g$ )  $Q_2$  phonons suitable for the estimated ground state distortion:

$$|0, n\rangle = \frac{(\hat{Q}_2^\dagger)^n}{\sqrt{n!}} |0, 0\rangle, \quad \hat{Q}_2^\dagger = \frac{1}{2} (a_x^\dagger - a_{-x}^\dagger - a_y^\dagger + a_{-y}^\dagger) \quad (4.4)$$

In order to evaluate vibrational overlap integrals  $A_{\alpha,\beta}^n(m)$ , one needs the expressions for overlap integrals of displaced harmonic oscillators [27, 47]. There are only diagonal contributions to the one- and two-phonon Raman cross sections:

$$\begin{aligned} A_{\alpha\beta}^1(m) &= \delta_{\alpha,\beta} \frac{e^{-\Delta} \Delta^m}{m!} \frac{m}{\Delta^{3/2}} (\Delta - m + 1) \\ A_{\alpha\beta}^2(m) &= \delta_{\alpha,\beta} \frac{e^{-\Delta} \Delta^m}{m!} \frac{m}{\sqrt{2} \Delta^2} (\Delta^2 - 2\Delta(m - 1) + (m - 1)(m - 2)) \end{aligned} \quad (4.5)$$

The calculations of the resonant Raman scattering of the  $Q_3$ -type phonon:

$$\hat{Q}_3^\dagger = \frac{1}{2\sqrt{3}} \left( 2a_z^\dagger - 2a_{-z}^\dagger - a_x^\dagger + a_{-x}^\dagger - a_y^\dagger + a_{-y}^\dagger \right) \quad (4.6)$$

gives zero intensity for the first- and second-order Raman processes in the  $Q_2$ -type distorted ground state ( $\Theta = 90^\circ$ ).

The resonance of the matrix element is shown in Fig. 4.9 for  $\gamma_0 = 120 \text{ cm}^{-1}$ . A pronounced resonant behavior is predicted when the laser frequency  $\omega_L$  approaches the orbiton energy  $2\Delta$ . The resonance position is fixed by the dielectric function shown in Fig. 4.1 at 2 eV. Within the FC mechanism the width of the resonance is given by  $\Delta$  and is 1 eV. The resonance profiles received from the experimental one- and two-phonon peaks ( $611 \text{ cm}^{-1}$  and  $1300 \text{ cm}^{-1}$  respectively) for one of the JT modes (for comparison depicted as well in figure 4.9) show a convincing agreement between experiment and theory, given the fact that none of the theoretical parameters is fixed by a fit to the experimental phonon resonances. The ratio between the one- and two-phonon scattering cross sections as well as their peak positions agree with the theoretical expectations. The most obvious difference is related to the much sharper experimental resonance data and could be resolved by considering a second contribution to the gap, maybe due to the additional crystal field splitting of the  $e_g$  orbitals by strain and electronic correlations neglected in the calculations. Furthermore, coupling to higher electronic states is not taken into account within this model possibly leading to an underestimation of the first-order Raman peak intensity [47].

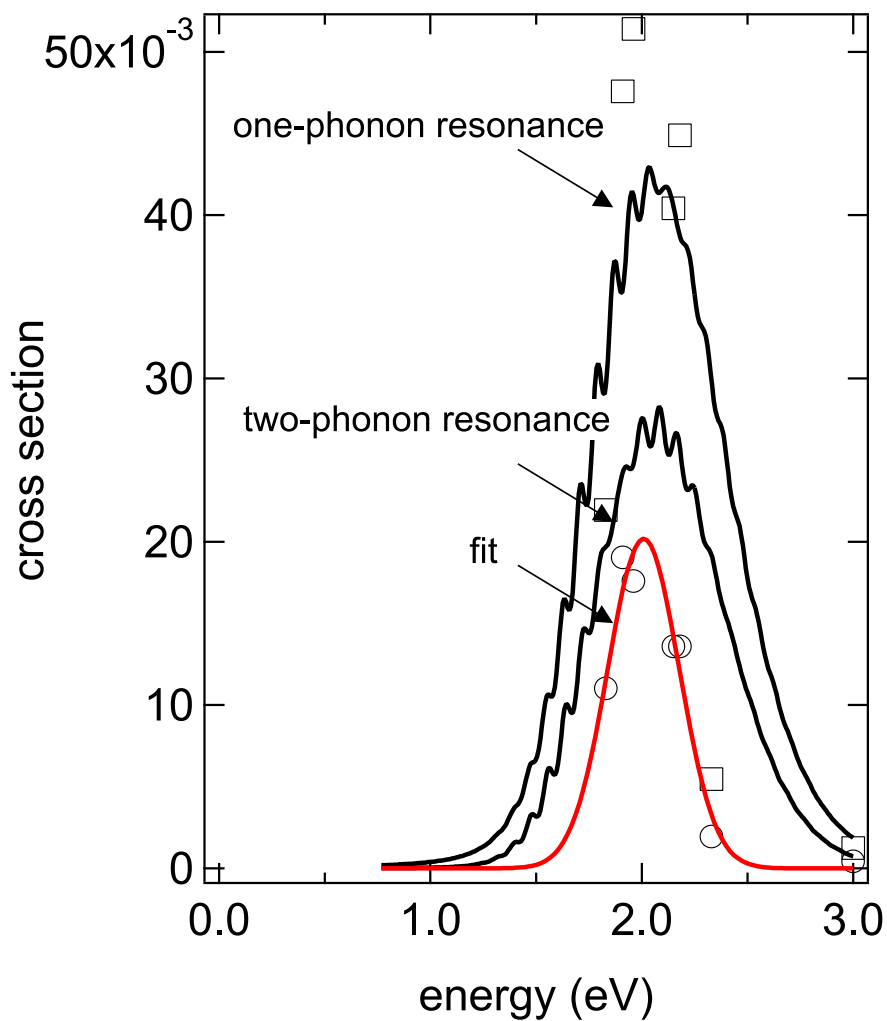


**Figure 4.9:** Comparison of the within the FC mechanism calculated (black curves) and experimentally (squares ( $611 \text{ cm}^{-1}$ ) and circles ( $1300 \text{ cm}^{-1}$ )) obtained one-phonon and two-phonon resonances (resonance profiles).

The enhanced ratio of the two-phonon scattering cross section over the one-phonon scattering cross section as well as the distinct coupling of the JT phonons to this 2 eV gap justifies the above model and confirms that the orbital ordering is to a large extent driven by the electron-phonon interaction although the relative phonon intensities associated with the different Q<sub>2</sub>- and Q<sub>3</sub>-type distorted ground states conflict with the model. From the fact that the resonances of the 611 cm<sup>-1</sup> mode (B<sub>2g</sub>-mode associated with the Q<sub>3</sub>-type distorted ground state) and the 496 cm<sup>-1</sup> mode (A<sub>g</sub>-mode associated with the Q<sub>2</sub>-type distorted ground state) are comparable in strength (see Fig. 4.6) we can conclude that the angle  $\Theta$  is much different from the estimated ground state distortion of 90°.

The absolute value of the Raman cross section (in units of  $\sigma_0$ ) according to equation (4.1) is a product of the resonant function  $S^n$  and the dipole matrix elements  $\gamma p$  measured in units of  $(m_e M \omega^2)^{1/2}$ . The dipole matrix element  $\gamma p$  is unknown (and might give a further explanation for the sharper experimental resonance than the theoretically calculated, due to its distinct resonance behavior). The absolute values of the dipole matrix elements can be taken from the optical conductivity oscillator strength  $f$  or calculated using Density Functional Theory (DFT). The optical conductivity oscillator strength  $f$  defined as  $\int d\omega \sigma_{\alpha\alpha}(\omega) = (\pi N e^2 / 2 m_e \Omega) f_{\alpha\alpha}$  can be described within the above deduced model as  $f_{\alpha\alpha} = 2((\gamma_{\alpha} p_{\alpha})^2 / m_e M \omega^2) / (2\Delta / \hbar \omega + 1)$  [3, 47]. Here  $N/\Omega$  is the Mn atom concentration. Measured spectral weights of the lowest broad line centered at 2 eV correspond to  $f_{\text{exp}} = 0.113$  [20],  $f_{\text{exp}} = 0.16$  [19] and  $f_{\text{exp}} = 0.22$  [58], which is in a good agreement with the DFT result  $f_{\text{DFT}} = 0.26$  [47]. The calculations of the anisotropy factor in the model of Perebeinos and Allen give

$$(\gamma_x p_x / \gamma_z p_z)^2 \equiv \sigma_{xx} / \sigma_{zz} = 0.5(2 + \cos(2\Theta)) / (1 - \cos(2\Theta)). \quad (4.7)$$

The corresponding relation of the oscillator strengths  $f_{xx} = 0.25$  and  $f_{zz} = 0.15$  experimentally received by Tobe et al [58] by integrated spectral weights result in the value 0.6, which corresponds to a  $\Theta$  of 36° - likewise to our measured phonon intensity relation not confirming a 90° distorted ground state. A  $\Theta$  of 90° inserted into the 90° distorted ground state model would account for a value of 0.25 of the relation calculated in 4.7 [47]. As mentioned by Perebeinos and Allen [47], diverse effects have been left out in the model (e.g. additional orbital splitting caused by superexchange interactions or the rotational distortions).

In addition, Tobe et al assign the 2 eV gap to an admixture of a p-d and a

d-d transition as their p-d model does not reflect the measured data and a d-d transition should be strongly affected by the spin ordering because of the large Hund's rule coupling in case of a nearest neighboring Mn<sup>3+</sup> transition. However, taking a spin independent FC intra-atomic d-d transition into account might reduce the necessity to involve a larger part of a p-d transition in the gap assignment to reflect the measured data.

Paper II

Orbital ordering in  $\text{LaMnO}_3$   
Investigated by Resonance  
Raman Spectroscopy

Reprinted article with permission from:  
R. Krüger, B. Schulz, S. Naler, R. Rauer, D.  
Budelmann, J. Bäckström, K. H. Kim, S-W. Cheong,  
V. Perebeinos, and M. Rübhausen

PHYSICAL REVIEW LETTERS, VOLUME 92,  
NUMBER 9, 097203, 2004

<https://doi.org/10.1103/PhysRevLett.92.097203>

Copyright 2019 by the American Physical Society.

## Orbital ordering in LaMnO<sub>3</sub> Investigated by Resonance Raman Spectroscopy

R. Krüger,<sup>1</sup> B. Schulz,<sup>1</sup> S. Naler,<sup>1</sup> R. Rauer,<sup>1</sup> D. Budelmann,<sup>1</sup> J. Bäckström,<sup>1</sup> K. H. Kim,<sup>2</sup> S-W. Cheong,<sup>3</sup> V. Perebeinos,<sup>4</sup> and M. Rübhausen<sup>1</sup>

<sup>1</sup>*Institut für Angewandte Physik, Universität Hamburg, Jungiusstraße 9, D-20355 Hamburg, Germany*

<sup>2</sup>*National High Magnetic Field Laboratory, MS-E536 LANL, Los Alamos, New Mexico 87545, USA*

<sup>3</sup>*Department of Physics and Astronomy, Rutgers University, Piscataway, New Jersey 08854, USA*

<sup>4</sup>*Brookhaven National Laboratory, Upton, New York 11973, USA*

(Received 15 June 2003; published 3 March 2004)

Orbital ordering leads to an unconventional excitation spectrum that we investigate by resonance Raman scattering using incident photon energies between 1.7 and 5.0 eV. We use spectral ellipsometry to determine the corresponding dielectric function. Our results show resonant behavior of the phonon Raman cross section when the laser frequency is close to the orbiton-excitation energy of 2 eV in LaMnO<sub>3</sub>. We show an excellent agreement between theoretical calculations based on the Franck-Condon mechanism activating multiphonon Raman scattering in first order of the electron-phonon coupling and the experimental data of phonons with different symmetries.

DOI: 10.1103/PhysRevLett.92.097203

PACS numbers: 75.47.Lx, 63.20.Ls, 71.27.+a, 78.30.-j

Signatures of orbital ordering have been unambiguously identified by elastic x-ray techniques [1]. However, much debate has been recently ignited about the dominant energy scale driving the formation of an orbital-ordered state and its corresponding excitation spectrum [2–4]. Two fundamentally different concepts lead to energy scales that differ by 1 order of magnitude. In one scenario the electron-phonon coupling drives the orbital ordering leading to a typical energy scale of the orbiton mode given by the strength of the electron-phonon (e-ph) coupling,  $\sim 1.5$  eV [3,5,6], whereas the second scenario predicts smaller energies  $\sim 0.16$  eV due to renormalization related to the strength of the Coulomb on-site repulsion [5–7]. Inelastic resonant scattering of visible and soft x-ray photons are currently strongly involved in tracking down the orbiton mode yielding also two fundamentally different assignments that differ by 1 order of magnitude in energy.

Here we present a resonant inelastic light-scattering study with excitation energies ranging from near IR (1.7 eV) to deep UV (5 eV) in order to investigate the matrix elements related to two important energies at around 2 and 4.4 eV, representing the Jahn-Teller (JT) and charge-transfer (CT) gaps, respectively [8,9]. Our experimental results are complemented by a symmetry-dependent calculation of the one- and two-phonon scattering cross sections within the Franck-Condon (FC) mechanism allowing for enhanced multiphonon scattering in the orbitally ordered state. Our main findings are (i) the one- and two-phonon excitation spectrum shows sharp resonances for incident photon energies close to the JT gap at 2 eV and at the CT gap at 4.4 eV; (ii) the one-phonon spectrum shows resonance profiles that strongly depend on the symmetry of the phonon modes. The vibrational oxygen breathing mode at  $655\text{ cm}^{-1}$  (81 meV) resonates strongly at the CT gap. Phonon modes

at  $611\text{ cm}^{-1}$  (76 meV) and at  $496\text{ cm}^{-1}$  (62 meV) show their strongest resonance at the JT gap; (iii) these three phonon modes with their individual resonance properties yield a complicated two-phonon spectrum between 1100 and  $1300\text{ cm}^{-1}$ ; (iv) we find good agreement between the symmetry-dependent resonance properties of the three main oxygen phonon modes and theoretical calculations based on the FC mechanism in the orbitally ordered state. This is indicative of an orbital-ordered state that is formed to a large extent by the e-ph interaction. The FC mechanism predicts the correct resonance energies of the JT modes at 2 eV and the correct one- to two-phonon ratios.

Previous Raman scattering studies have been performed with visible incident photon energies showing an excellent agreement with the assignment of Iliev *et al.* in the one-phonon spectrum between 80 and  $640\text{ cm}^{-1}$  [10]. More controversial is the assignment of modes in the two-phonon spectral range between 1100 and  $1300\text{ cm}^{-1}$  with a claim that a mode at 160 meV is not related to a two-phonon peak but to an orbital wave or orbiton [7]. This claim has been challenged by Grüninger *et al.*, who identify the  $1300\text{ cm}^{-1}$  mode as an overtone of the highest energy one-phonon peak in the IR spectrum. However, due to possible symmetry breaking, the parity argument discriminating Raman and IR data might not hold and the situation remains unclear [11]. Our resonance study reveals the inelastic light-scattering matrix elements and shows that the resonances of the one-phonon modes are also visible in the two-phonon spectra, strongly suggesting a phononic origin of the peaks between 1100 and  $1300\text{ cm}^{-1}$ .

The inelastic light-scattering experiments have been performed on a novel Raman spectrometer (McPherson) equipped with a UV-sensitive charge-coupled device and with a reflecting objective in a Cassegrain design. The

primary mirror is an on-axis parabola with a numerical aperture of 0.5 [12]. The incident light is generated by  $\text{Ar}^+$  and  $\text{Kr}^+$  lasers with an intracavity frequency doubler for wavelengths below 275 nm. The incident light passes optical elements (premonochromator, scrambler, spatial filter, and polarizer) and is focused by the reflecting objective that also couples the scattered light into the spectrometer. Because of the diffraction limited imaging we determine the size of the spot by the size of the pinhole in the spatial filter. We have used a  $30\ \mu\text{m}$  spot and 8 mW of power on the sample in order to avoid any significant heating. The Raman spectrometer has been calibrated by two double Ulbricht sphere systems for visible and ultraviolet wavelengths (gigahertz). Measurements have been performed on single crystals at room temperature in a temperature ( $22 \pm 0.3\ \text{C}$ ) and humidity ( $45\% \pm 3\%$ ) controlled clean room (class 100) and in backscattering configuration with parallel polarization for the incident and scattered light along the in-plane crystal axis probing phonons of  $A_g$  and  $B_{2g}$  symmetry. The spectra are corrected for integration time, incident power, the wavelength dependent penetration depth, and reflection coefficient as determined by the dielectric function measured by spectroscopic ellipsometry (Sentech Instruments). The largest error of the experiment is given by the chromatic aberrations in the spatial filter with a change of the incident photon energy. By repeated measurements of Si-reference spectra across our full spectral range we estimate a maximum error in the UV of less than 10%. Other error sources such as the uncertainty of the dielectric function or the stability of the laser yield errors of the order of less than 1%.

In Fig. 1 we present Raman spectra for incident photon energies from 1.96 to 4.5 eV, in the one- (a) and two-phonon (b) spectral ranges. For previously used incident photon energies (1.96 and 2.34 eV) we see the well-known phonon modes of  $A_g$  and  $B_{2g}$  symmetry. Between 200 and  $400\ \text{cm}^{-1}$  the spectra show strong signals from the in-phase  $y$  rotation  $A_g(2)$  at  $257\ \text{cm}^{-1}$ , and the out-of-phase  $x$  rotation  $A_g(4)$  at  $284\ \text{cm}^{-1}$ . Both modes show a weak signal with visible excitation energies and strong resonance enhancements for deep-UV excitation, clearly supporting their assignment as rotational vibrations that are not coupling strongly to the JT  $e_g$  levels. There is the appearance of an additional mode in the deep UV around  $448\ \text{cm}^{-1}$  (4.1 and 4.5 eV) that has not been observed before, showing an analogous resonance behavior to the rotational modes. The higher-energy oxygen modes are observed between  $496$  and  $655\ \text{cm}^{-1}$ . Especially, the in-phase stretching  $B_{2g}(1)$  mode at  $611\ \text{cm}^{-1}$  shows a single pronounced resonance at around 2 eV as it strongly modulates the JT levels. Phonons around  $496$  and  $655\ \text{cm}^{-1}$  resonate towards 2 and 4.4 eV. This strongly suggests that the  $496\ \text{cm}^{-1}$  phonon is not a pure rotational or bending mode of the oxygen cage but rather related to the  $A_g(1)$  in-phase stretching mode and

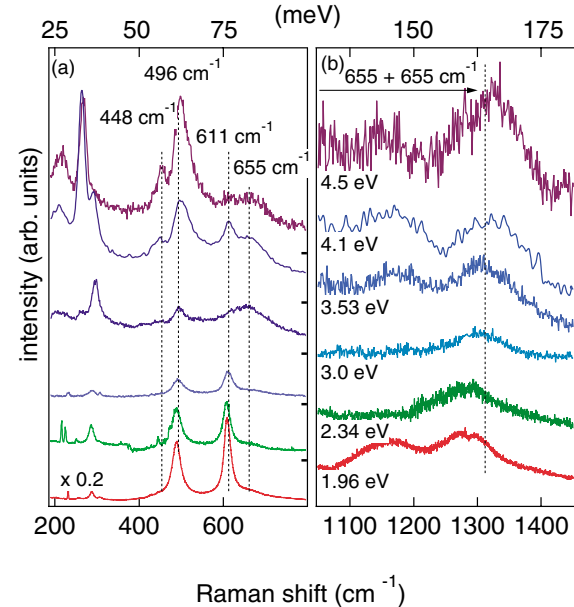


FIG. 1 (color online). Experimental spectra showing the oxygen vibrations of the distorted  $\text{MnO}_6$  octahedra in the one- (a) and two-phonon (b) regions.

that the new mode at  $448\ \text{cm}^{-1}$  is most probably the bending  $A_g(3)$  vibration [10].

Figure 1(b) displays the two-phonon region for the same incident photon energies as Fig. 1(a). Overall we find two-phonon features that correspond to the energy range between  $1100$  and  $1300\ \text{cm}^{-1}$ , i.e., about twice  $611$  and  $655\ \text{cm}^{-1}$ . The more complicated two-phonon spectrum typical for the visible spectral range simplifies when the  $611\ \text{cm}^{-1}$  mode disappears in the deep UV, leaving alone a single peak at  $1300\ \text{cm}^{-1}$ . This two-phonon peak exhibits the same matrix elements as the  $655\ \text{cm}^{-1}$  phonon resonating towards the charge-transfer gap at 4.4 eV.

The details of the observed resonances for the three JT related phonons, as well as the resonances of the two-phonon peak around  $1300\ \text{cm}^{-1}$ , are shown in Figs. 2(a) and 2(b), respectively. The most important observations in Fig. 2(a) are that all three one-phonon modes resonate at the same energy of 2.05 eV with a FWHM of 0.65 eV, as derived from a fit of a Gaussian profile (solid line) to the data points. The second resonance around the charge-transfer energy is visible in the  $655\ \text{cm}^{-1}$  and in the  $496\ \text{cm}^{-1}$  phonon with slightly shifted energies (4.1 to 4.4 eV), but with the same width of the resonances of 1.32 eV. The dielectric function shows that the first resonance corresponds to the JT gap and that absorption levels at 2.2 and 2.5 eV are not involved in the resonance process. Moreover, we find the strong resonance of the CT level buried in a monotonically increasing absorption band. The shift in resonance energy of the  $496$  and  $655\ \text{cm}^{-1}$  phonons could be due to a symmetry-dependent renormalization of the matrix elements or due to the presence of additional CT processes such as a combination of O  $p$

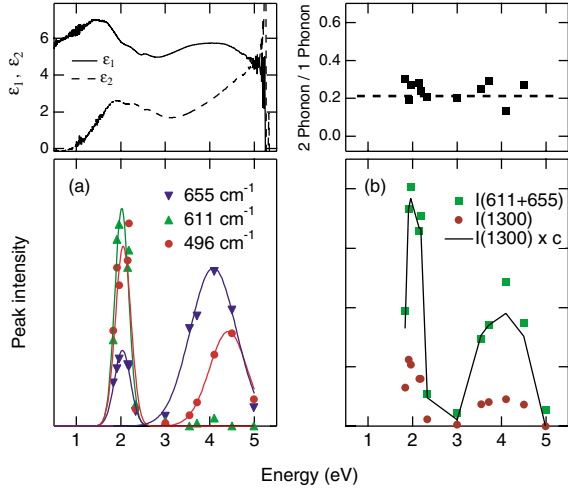


FIG. 2 (color online). Resonance profiles of the one-phonon excitations (a) and the comparison between the resonance profiles of the one- and two-phonon excitations (b). The inset in (a) shows  $\epsilon_1$  (solid line) and  $\epsilon_2$  (dashed line) of the dielectric function and in (b) the ratio of the one- to two-phonon intensities.

to Mn  $d$  (crystal-field splitting) and Mn  $d$  to nearest neighbor Mn  $d$  transitions (correlations).

Figure 2(b) shows the integrated intensity of the two one-phonon peaks at 611 and 655  $\text{cm}^{-1}$  as well as that of the two-phonon peak. The solid line is the two-phonon peak intensity multiplied by a factor of 4.166. The inset shows the constant ratio of the one- to two-phonon peak intensities between 1.8 and 5 eV. This indicates that the feature at 1300  $\text{cm}^{-1}$  is indeed a two-phonon peak as such a behavior of one- to two-phonon resonances is also typical for, e.g., Si [13].

In the conventional Raman scattering process of phonons, where electronically excited states do not alter atomic positions, the intensity of the  $n$ -phonon peak is proportional to  $g^{2n}$ , where  $g$  is the e-ph interaction and is a small number of  $\approx 10^{-1}$ – $10^{-2}$ . When the oscillator potential curves of ground and excited states are displaced, vibrational Raman scattering is activated by a FC mechanism. In the first step of the FC Raman process, the incident photon creates an orbital defect in the ordered JT ground state. This Frenkel exciton, or orbiton, is self-trapped by an oxygen rearrangement from the JT state [6]. The FC principle has the oxygen positions undistorted during optical excitation, producing a vibrationally excited state of the orbiton. In the second step of the Raman process, this virtual excitation decays back to the orbital, but not necessarily to the vibrational, ground state. The amplitude for ending in a vibrationally excited state is determined by displaced-oscillator overlap integrals allowing  $n$ -phonon resonant Raman scattering with intensities proportional to  $g^n$  [14].

Perrebeinos and Allen gave a derivation of the resonant multiphonon Raman cross section [15] with a net result:

$$\frac{\partial^2 R_{\alpha\beta}^n}{\partial \omega_R \partial \Omega} = S \left| \sum_{m=0}^{\infty} \frac{\hbar \omega A_{\alpha\beta}^n(m)}{\Delta + m\hbar\omega - \hbar\omega_L + i\gamma_m} \right|^2 \times \delta(\omega_R - n\omega), \quad (1)$$

$$A_{\alpha\beta}^n(m) = \sum_{\{m'\}} \delta(m - N\{m'\}) \langle n | u_{\alpha} + u_{-\alpha} | m' \rangle \times \langle m' | u_{\beta} + u_{-\beta} | 0 \rangle,$$

where  $S = (\sigma_0 \omega_S)^2 / \omega_L^2$  and  $\sigma_0 = r_e^2 = e^2 / m_e c^2$  is the Compton cross section. The summation goes over all electronic states and corresponding vibrational quanta  $\{m\}$ .  $N\{m\} = m_x + m_y + m_z + m_{-x} + m_{-y} + m_{-z}$  is the total number of vibrational quanta of the six neighboring oxygens. To model the damping term  $\gamma_m$  of the vibrational level  $m$ , we use the expression  $\gamma_m = \gamma_0 \sqrt{m+1}$ , as in a sequence of convolved Gaussians, intended to mimic the local densities of phonon states on oxygen atoms. The induced dipole matrix elements and displacements are measured in units of  $(m_e M \omega^2)^{1/2}$  and  $\sqrt{\hbar / M \omega}$ , respectively. The ground state couples to excited electronic states by the electron-radiation Hamiltonian ( $\hat{p} \cdot \vec{A}$ ) responsible for resonant Raman scattering. It has been suggested [6,15] that this transition becomes allowed because of asymmetric oxygen fluctuations [16].

In the previous work [15], the symmetry of the excited phonon in the final state was not taken into account. Here we allow the final state  $|0, n\rangle$  to have an electronic ground state plus  $n$  vibrational  $A_g$  ( $Q_2$ ) phonons:

$$|0, n\rangle = \frac{[\frac{1}{2}(a_x^\dagger - a_{-x}^\dagger - a_y^\dagger + a_{-y}^\dagger)]^n}{\sqrt{n!}} |0, 0\rangle. \quad (2)$$

To evaluate vibrational integrals  $A_{\alpha\beta}^n(m)$  one needs the expressions for overlap integrals of displaced harmonic oscillators [14,15]. There are only diagonal contributions to the one- and two-phonon Raman cross sections:

$$A_{\alpha\beta}^1(m) = \delta_{\alpha\beta} \frac{e^{-\Delta} \Delta^m}{m!} \frac{m}{\Delta^{3/2}} (\Delta - m + 1),$$

$$A_{\alpha\beta}^2(m) = \delta_{\alpha\beta} \frac{e^{-\Delta} \Delta^m}{m!} \frac{m}{\sqrt{2} \Delta^2} \times [\Delta^2 - 2\Delta(m-1) + (m-1)(m-2)]. \quad (3)$$

The resonance of the matrix element is shown in Fig. 3 for  $\gamma_0 = 120 \text{ cm}^{-1}$ . A pronounced resonant behavior is predicted when the laser frequency  $\omega_L$  approaches the orbiton energy  $2\Delta$ . The resonance position is fixed by the dielectric function (Fig. 2) at 2 eV. Within the FC mechanism the width of the resonance is given by  $\Delta$  and is 1 eV. The experimental results of the resonance profiles of the one- and two-phonon peaks show a remarkable agreement between experiment and theory given the fact that none of the theoretical parameters is fixed by a fit to the experimental phonon resonances. The ratio between the one- and two-phonon scattering cross sections as well as their

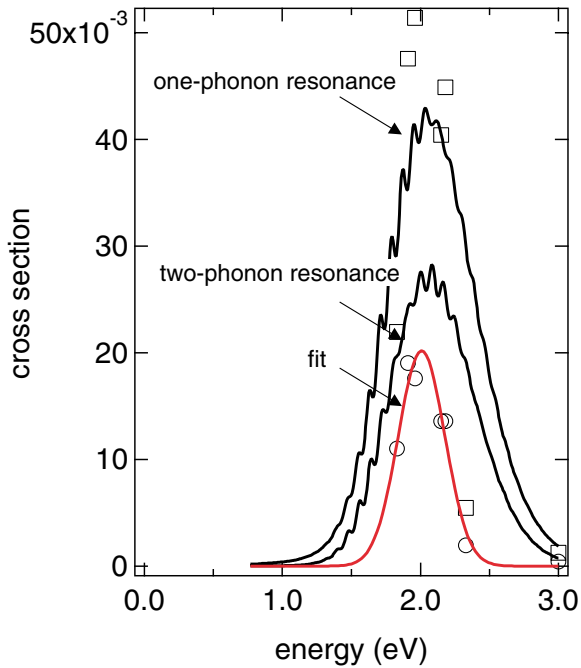


FIG. 3 (color online). Solid lines show the resonance profiles at orbitor energy of the one- and two-phonon peaks according to the Franck-Condon mechanism. Markers represent experimental data for the  $611\text{ cm}^{-1}$  one-phonon (squares) and the  $1300\text{ cm}^{-1}$  two-phonon (circles) resonance.

peak positions agree with the theoretical expectations. The most obvious difference is the much sharper experimental resonance data and could be resolved by considering a second gap contribution maybe due to the additional crystal-field splitting of the  $e_g$  orbitals by strain and electronic correlations neglected in our calculations [17].

The absolute value of the Raman cross section (in units of  $\sigma_0$ ) according to Eq. (1) is a product of the resonant function  $S^n$  and the dipole matrix elements measured in units of  $(m_e M \omega^2)^{1/2}$ . The model Hamiltonian [2,5] predicts a minimum at amplitude  $Q = \sqrt{A_g^2 + B_{2g}^2}$  of the cooperative oxygen distortions. The minimum  $(B_{2g}, A_g) = Q(\cos\Theta, \sin\Theta)$ , however, is degenerate with respect to angle  $\Theta$ .

The results for the vibrational overlap integrals  $A_{\alpha,\beta}^n$  Eq. (3) and resonances in Fig. 3 are reported for a purely  $B_{2g}$ -type distorted ground state ( $\Theta = 90^\circ$ ). The absolute value of the dipole matrix elements can be taken from the optical conductivity oscillator strength or density functional theory (DFT) calculations. The measured spectral weight of the lowest broad line centered at 2 eV corresponds to  $f_{\text{exp}} = 0.113$  [8],  $f_{\text{exp}} = 0.16$  [9], and  $f_{\text{exp}} = 0.22$  [18], which agrees with the DFT result  $f_{\text{DFT}} = 0.26$  [15]. The calculations of the resonant Raman scattering of the  $A_g$ -type phonons gives zero intensity for the first and second order Raman processes in the  $B_{2g}$ -type distorted

ground state ( $\Theta = 90^\circ$ ). From the fact that the resonances of the  $611$  and  $496\text{ cm}^{-1}$  modes are comparable in strength (see Fig. 2) we can confirm that the angle  $\Theta$  is much different from  $90^\circ$  in agreement with the prediction for the anisotropy of the optical conductivity  $\sigma_{xx}/\sigma_{zz} = 0.5[2 + \cos(2\Theta)]/[1 - \cos(2\Theta)]$  and results from Tobe *et al.* [18] suggesting  $\Theta \approx 36^\circ$ .

In summary, we have shown the efficiency of inelastic light scattering to study the interplay between electronic structure and orbital ordering in  $\text{LaMnO}_3$ . We find that the orbital ordering is to a large extent driven by the electron-phonon interaction with some additional electronic contribution. We find a remarkably good agreement between the experimental results and a theory based on the Franck-Condon mechanism.

We acknowledge many stimulating discussions with M.V. Klein, S. L. Cooper, U. Merkt, M.V. Abrashev, and P. Allen. We thank McPherson (Erik Schoeffel and Art Mayhill) for the excellent collaboration. We are supported by DFG Ru773/2-2, by Ru773/2-3, by GrK "Physik nanostrukturierter Festkörper," by NSF-DMR-0080008 (S-W. C.), and by U.S. DOE DE-AC02-98CH10886 (V. P.). K. H. K. is partially supported by CSCMR through the KOSEF.

- [1] Y. Murakami *et al.*, Phys. Rev. Lett. **81**, 582 (1998).
- [2] A. J. Millis, Phys. Rev. B **53**, 8434 (1996).
- [3] A. J. Millis, B. I. Shraiman, and R. Mueller, Phys. Rev. Lett. **77**, 175 (1996).
- [4] E. Dagotto, T. Hotta, and A. Moreo, Phys. Rep. **344**, 1 (2001).
- [5] P. B. Allen and V. Perebeinos, Phys. Rev. B **60**, 10747 (1999).
- [6] P. B. Allen and V. Perebeinos, Phys. Rev. Lett. **83**, 4828 (1999).
- [7] E. Saitoh *et al.*, Nature (London) **410**, 180 (2001).
- [8] J. H. Jung *et al.*, Phys. Rev. B **57**, 11043 (1998).
- [9] J. H. Jung *et al.*, Phys. Rev. B **55**, 15489 (1997).
- [10] M. N. Iliev *et al.*, Phys. Rev. B **57**, 2872 (1998).
- [11] M. Grüninger *et al.*, Nature (London) **418**, 39 (2002).
- [12] On the entrance objective, see, e.g., Photonics Spectra 159 (October 2002).
- [13] J. R. Renucci, R. N. Tyte, and M. Cardona, Phys. Rev. B **11**, 3885 (1975).
- [14] L. L. Kruschinskii and P. P. Shorygin, Opt. Spectrosc. (USSR) **11**, 12 (1961); **11**, 80 (1961).
- [15] V. Perebeinos and P. B. Allen, Phys. Rev. B **64**, 085118 (2001).
- [16] Alternatively,  $d-d$  transitions could be also activated by static disorder of the oxygen octahedra or a quasielastic contribution.
- [17] J. van den Brink, Peter Horsch, and Andrzej M. Oles, Phys. Rev. Lett. **85**, 5174 (2000).
- [18] K. Tobe *et al.*, Phys. Rev. B **64**, 184421 (2001).

# Chapter 5

## Summary and outlook

The optical measurements (resonance Raman scattering complemented by spectroscopic ellipsometry) received within this thesis supported solving the controversial discussion of the energy scale and the mechanism driving the orbital ordering and the related orbiton excitation energy scale in  $\text{LaMnO}_3$ . We exclude the superexchange mechanism as the dominating effect in  $\text{LaMnO}_3$  leading to orbital ordering by assigning the excitations observed in the corresponding energy region around  $1300 \text{ cm}^{-1}$  (0.16 eV respectively) to a multiphonon origin. In addition, the resonance behavior of phonon modes related to the Jahn-Teller effect indicate that the 2 eV gap can be assigned to the JT splitting and the gap around 4 eV results from charge-transfer processes. Enhanced multiphonon excitations support the theory of Philip Allen and Vasili Perebeinos [3, 47] of an orbital ordering driven by the JT effect and a strong electron-phonon coupling. An orbital flip in the orbitally ordered and JT distorted ground state (orbital exciton) followed by a rearrangement of the oxygen octahedron can be interpreted as a selftrapped Frenkel-exciton or as an orbiton. Perebeinos and Allen calculated the expected two- and one-phonon resonance profiles within the Franck-Condon mechanism, which show a remarkable match with our data. Deviating from their estimation of a  $Q_2$ -distorted ground state allowing only  $Q_2$ -distortion related phonons, we find phonon intensities of a  $Q_3$ -distortion related phonon of similar strength. Future model calculations taking a mixed distortion into account could help finding the correct distortion angle. Likewise, it might be reasonable to integrate rotational and tilting distortions and possibly anharmonicity effects. In summary we relate the 2 eV resonance (in contrast to interpretations as charge-transfer gap or d-d transitions on neighboring sites) mainly to an intra-atomic d-d transition via the FC mechanism, which can likewise be

assigned to the orbiton energy. To observe the orbital exciton as a direct Raman excitation, experimental conditions providing large Raman shifts are necessary and would be informative to illuminate the nature of the orbiton. Furthermore, extending the excitation energy towards higher energies would give information about new excitations coupling to the charge-transfer transition or higher electronic gaps. Concluding, we have shown the efficiency of inelastic light scattering to study the interplay between the electronic structure, the lattice degrees of freedom and the orbital ordering in  $\text{LaMnO}_3$ .

# Chapter 6

## Acknowledgments

I would like to thank

- Prof. Dr. Michael Rübhausen for letting me participate in his forward-looking scientific vision by offering excellent experimental conditions, guiding and explaining a lot but also for giving the opportunity to work in my own way. Thank you for your patience!
- Prof. Dr. Arwen Pearson for taking over the evaluation of this thesis.
- Prof. Dr. Nils Huse for being referee of the defense of this thesis.
- Prof. Dr. Vasili Perebeinos for model calculations within the Franck-Condon mechanism.
- Prof. Dr. Clemens Ulrich for helpful explanations and literature suggestions.
- for financial support by GrK "Physik nanostrukturierter Festkörper".
  
- my colleagues of the first days for being great labmates and their friendly support in so many ways: Dr. Ilka Mahns, Dr. Marta Swiebodzinski, Dr. Stephan Binder and not to forget in addition
- Dr. Benjamin Schulz for his introduction to the UT-3 and answering many questions patiently.
- Dr. Stefan Naler for taking over some Raman measurements of this study and together with

- Dr. Danny Chan for several very nice coffee breaks including controversial discussions. I like listening to your view of the world, but you still haven't convinced me...
- Dr. Ralf Rauer for cooperatively working on  $\text{LaMnO}_3$  and the ellipsometric data.
- Dr. Jörg Kunze for inspiring discussions about manganites and life in general.

I would also like to acknowledge all today's and former members of the (APOG) optics group of Prof. Dr. Rübhausen and office mates as colleagues creating a friendly and cooperative atmosphere and beyond that I thank

- Dr. Benjamin Grimm-Lebsaft for solving so many computer problems, and for providing freshly prepared delicious "food on foot" during my final writing months - to mention only two points on a long list. To make it short - thanks a lot for all your versatile support and being a good friend! I'm glad, that I had the opportunity to get to know you.
- Dr. Gerd Neuber for his conscientious feedback to this work and sharing his rich knowledge of ellipsometry. I enjoyed our friendly discussions and all the impulses you gave.
- Dieter Rukser for several conversations about physics and life. I value your open-minded nature always looking behind what is obvious.
- Dr. Mykola Biednov for ensuring the supply of light and fresh air as well as a good mood in our shared interior office.
- Dr. Maria Naumova for always offering a helping hand.

...and last but not least:

- Dirk Schäfer for the correction of the punctuation and some helpful advice concerning my English. Thank you for straightforwardly taking over the final reading!
- Dr. Jörn Hoyer for learning together for so many years and company at all important stages of life!
- Kathrin von der Weth for giving a sympathetic ear as well as honest and encouraging words through all decades of my life and this thesis :-). I admire your willpower and really appreciate our close friendship!

- Thomas Maeser for taking over childcare during the last period of writing and financial support. I wouldn't have managed to finish this work without your help!
- Wilma Krüger and Herbert Krüger for offering and giving help in all circumstances as parents and grandparents and always being just one phone call away when needed! Thank you for everything you enabled me!
- Romina Maeser and Silas Maeser - main reasons for the interruption and greatest motivation to complete this work at the same time. I know you suffered the most. I thank you for being there and that fantastic as you are!

Finally, I would like to express my sincerest gratitude to all my friends and my family not mentioned here by name for never losing the endurance to inquire about the progress of this work. Thanks a lot for all your understanding, encouragement and support!



# Appendix A

## Error estimation of the solid angle correction

To correct the effective sample volume  $V_S(\omega_i)$ , in equation 3.42 the formula for the solid angle  $\Omega = \frac{A}{r^2}$  with  $A$  a surface area of a spherical cap (without the area of the base) and  $r$  the radius of a sphere is approximated by  $\tan^2 \theta_{sam}$ . In the following, an estimation of the error of this substitution is given taking different  $\theta_{sam}$  into account. Figure A.1a) shows a spherical cap. The base of the spherical cap is indicated in gray with  $a$ , the radius of the base. The radius of the sphere is  $r$  and the height of the cap  $h$ . The surface area of the spherical cap (without the area of the base) is

$$A = 2\pi r h. \quad (\text{A.1})$$

With

$$r^2 = (r - h)^2 + a^2 = r^2 + h^2 - 2rh + a^2 \quad (\text{A.2})$$

follows:

$$r = \frac{a^2 + h^2}{2h} \quad (\text{A.3})$$

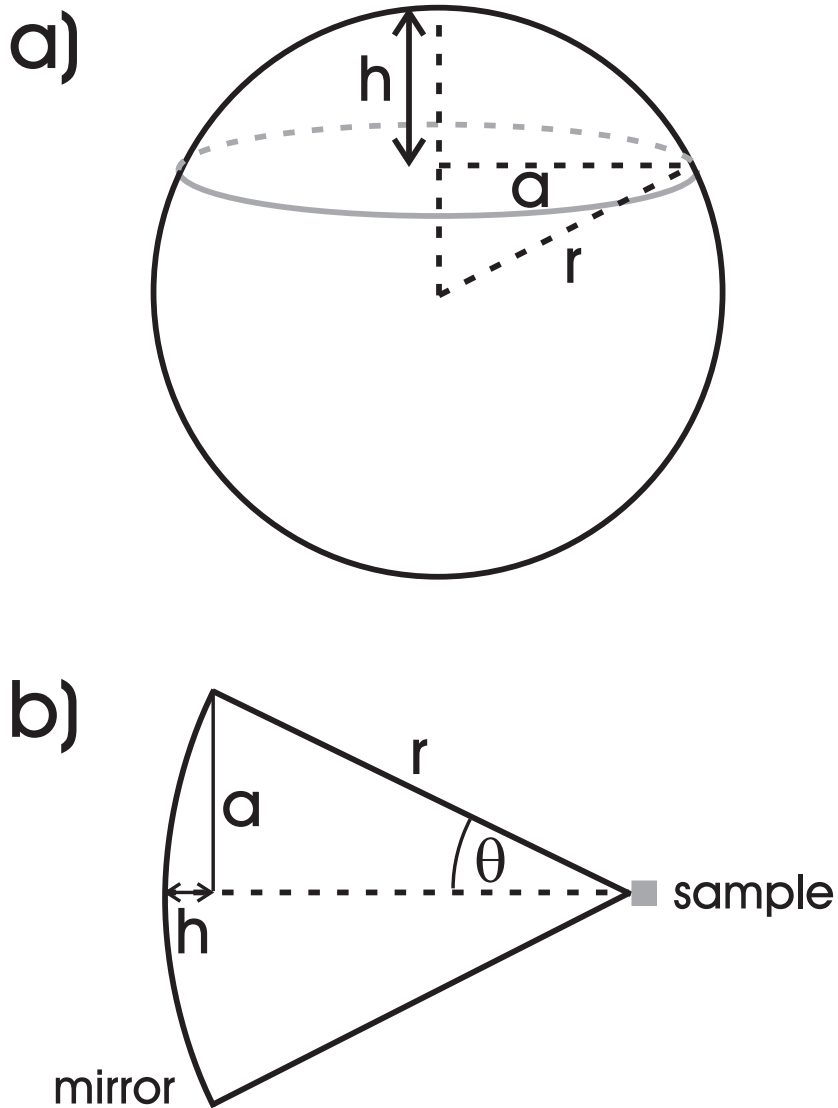


**Figure A.1:** a) shows a spherical cap with  $a$  the radius of its base and  $h$  the height of the cap and  $r$  the radius of the sphere. A cross section of a spherical cap is depicted in b). In case of no absorption and  $n = n' = 1$  (same refractive index inside and outside of the sample), the cone in b) represents the solid angle (depicted in cross section) inside and outside the sample similarly (though  $\theta$  is named  $\theta_{sam}$  inside the sample). In opposition to this representation, the corresponding mirror M1 in the UT-3 experiment is parabolic. As it does not influence the calculations above, it is not graphically shown here.

and

$$h = r - \sqrt{(r^2 - a^2)} \quad (\text{A.4})$$

and consequently another formulation for equation A.1 is

$$A = \pi(a^2 + h^2). \quad (\text{A.5})$$

In this case the definition for the solid angle  $\Omega$  results in

$$\Omega = \frac{A}{r^2} = \frac{\pi(a^2 + h^2)}{r^2} \quad (\text{A.6})$$

and for  $\tan^2 \theta$  in

$$\tan^2 \theta = \frac{a^2}{(r - h)^2} \quad (\text{A.7})$$

with  $\theta$ , the limiting angle of the light cone (in cross section) (see figure A.1b)). Figure A.1b) visualizes a cross section of the incoming light cone with  $\theta$  the limiting incident angle -  $\theta_{sam}$ , the angle inside the sample, is not depicted. Here and in the following calculations only the special case of no absorption is considered. With the additional assumption that the refractive index inside ( $n'$ ) and outside ( $n$ ) of the sample is identical ( $n = n' = 1$ ), figure A.1b) illustrates the solid angle (in cross section) inside and outside the sample similarly (though  $\theta$  is named  $\theta_{sam}$  inside the sample).

The relation between the solid angle  $\Omega$  and  $\tan^2 \theta_{sam}$  without the factor  $\pi(w.\pi)$  in the numerator is given by

$$\frac{\Omega(w.\pi)}{\tan^2 \theta_{sam}} = \frac{(a^2 - h^2)^2}{(a^2 + h^2) \cdot a^2} \quad (\text{A.8})$$

With F-number 1 (i.e.  $\frac{f}{D}$  with  $f$ , the focal length and  $D$ , the diameter) of the UT-3 mirror M1 and  $D = 250$  mm the focal length results in  $f = r-h = 250$  mm and  $a = 125$  mm and  $h \approx 29.51$  mm (with equations A.2 - A.4). Then (in case of  $n = n' = 1$  and no absorption)

$$\frac{\Omega(w.\pi)}{\tan^2 \theta_{sam}} \approx 0.845. \quad (\text{A.9})$$

This is the relation for a maximum value of  $\theta_{sam} = 26.56^\circ$  corresponding to the absolute correction factor  $\tan^2(26.56^\circ) \approx 0.250$ .

Exemplarily for further refractive indices  $n'$  of the sample and the corresponding  $\theta_{sam}$  the relation  $\frac{\Omega(w,\pi)}{\tan^2 \theta_{sam}}$  and the absolute correction factor  $\tan^2 \theta_{sam}$  are calculated. With the aid of Snell's law

$$n \sin \theta = n' \sin \theta_{sam} \quad (\text{A.10})$$

(valid in case of no absorption) and  $n = 1$  the following  $\theta_{sam}$  are obtained:

With  $n' = 1.5 \Rightarrow \theta_{sam} \approx 17.34^\circ$ ,

with  $n' = 2.0 \Rightarrow \theta_{sam} \approx 12.92^\circ$ ,

with  $n' = 2.5 \Rightarrow \theta_{sam} \approx 10.30^\circ$ .

For  $\theta_{sam} = 17.34^\circ$  :

With  $\tan \theta_{sam} = \frac{a}{r-h}$ , equations A.2 + A.4 and an arbitrary value of  $a$

$$\frac{\Omega(w,\pi)}{\tan^2(17.34^\circ)} \approx 0.932 \text{ and } \tan^2(17.34^\circ) \approx 0.098.$$

Analogously:

for  $\theta_{sam} = 12.92^\circ$  :

$$\frac{\Omega(w,\pi)}{\tan^2(12.92^\circ)} \approx 0.962 \text{ and } \tan^2(12.92^\circ) \approx 0.053$$

and

for  $\theta_{sam} = 10.30^\circ$  :

$$\frac{\Omega(w,\pi)}{\tan^2(10.30^\circ)} \approx 0.976 \text{ and } \tan^2(10.30^\circ) \approx 0.033.$$

From this follows that the error resulting from the slightly changing relation of  $\frac{\Omega(w,\pi)}{\tan^2 \theta_{sam}}$  in dependence of  $\theta_{sam}$  is negligible in relation to the change of the absolute correction factor  $\tan^2 \theta_{sam}$  in dependence of  $\theta_{sam}$  in case of the UT-3.

# Bibliography

- [1] P. B. Allen and V. Perebeinos. Condensed-matter physics - First glimpse of the orbiton. *Nature*, 410(6825):155–158, 2001.
- [2] Philip B. Allen and Vasili Perebeinos. Anti-Jahn-Teller polaron in LaMnO<sub>3</sub>. *Physical Review B*, 60(15):10747–10753, 1999.
- [3] Philip B. Allen and Vasili Perebeinos. Self-Trapped Exciton and Franck-Condon Spectra Predicted in LaMnO<sub>3</sub>. *Physical Review Letters*, 83:4828–4831, 1999.
- [4] J. A. Alonso, M. J. Martinez-Lope, M. T. Casais, and M. T. Fernandez-Diaz. Evolution of the Jahn-Teller Distortion of MnO<sub>6</sub> Octahedra in RMnO<sub>3</sub> Perovskites (R = Pr, Nd, Dy, Tb, Ho, Er, Y): A Neutron Diffraction Study. *Inorg. Chem.*, 39:917–923, 2000.
- [5] T. Arima, Y. Tokura, and J. B. Torrance. Variation of optical gaps in perovskite-type 3d transition-metal oxides. *Physical Review B*, 48(23):17006–17009, 1993. doi:10.1103/PhysRevB.48.17006.
- [6] Joakim Bäckström. *Raman Scattering and Neutron Diffraction Studies of Manganites and Cuprates*. PhD thesis, Chalmers Göteborg University, Göteborg, 2001.
- [7] N. M. Bashara and R. M. A. Azzam. *Ellipsometry and Polarized Light*. North-Holland, 1987.
- [8] D. Chan. *Optical investigations of bioorganic systems by spectrally resolved ellipsometry*. PhD thesis, University of Hamburg, Göttingen, 2005.
- [9] Tapan Chatterji, editor. *Colossal Magnetoresistive Manganites*. Kluwer Academic Publishers, 2004.

- [10] E. Dagotto. *Nanoscale Phase Separation and Colossal Magnetoresistance: The Physics of Manganites and Related Compounds*. Berlin: Springer-Verlag, 2003.
- [11] Peter Fulde. *Correlated Electrons in Quantum Matter*. World Scientific Publishing Co. Pte. Ltd., 2012.
- [12] John B. Goodenough. Theory of the Role of Covalence in the Perovskite-Type Manganites  $[La, M(II)]MnO_3$ . *Physical Review*, 100(2):564–573, 1955.
- [13] M. Grüninger, R. Rückamp, M. Windt, P. Reutler, C. Zobel, T. Lorenz, A. Freimuth, and A. Revcolevschi. Experimental quest for orbital waves. *Nature*, 418:39–40, 2002.
- [14] M. Hecht. *Optik*. Oldenbourg Verlag, München, 2001.
- [15] M. N. Iliev, M. V. Abrashev, H.-G. Lee, V. N. Popov, Y. Y. Sun, C. Thomsen, R. L. Meng, and C. W. Chu. Raman spectroscopy of orthorhombic perovskitelike  $YMnO_3$  and  $LaMnO_3$ . *Physical Review B*, 57(5):2872–2877, feb 1998. URL: <https://link.aps.org/doi/10.1103/PhysRevB.57.2872>, doi:10.1103/PhysRevB.57.2872.
- [16] Masatoshi Imada, Atsushi Fujimori, and Yoshinori Tokura. Metal-insulator transitions. *Reviews of Modern Physics*, 70(4):1039–1263, 1998. URL: <https://link.aps.org/doi/10.1103/RevModPhys.70.1039>, doi:10.1103/RevModPhys.70.1039.
- [17] S. Jin, T. H. Tiefel, M. McCormack, R. A. Fastnacht, R. Ramesh, and L. H. Chen. Thousandfold Change in Resistivity in La-Ca-Mn-O Films. *Science*, 264(April):413, 1994.
- [18] G. H. Jonker and J. H. van Santen. Ferromagnetic compounds of manganese with perovskite structure. *Physica*, 16(3):337–349, 1950.
- [19] J. H. Jung, K. H. Kim, D. J. Eom, T. W. Noh, E. J. Choi, Jaejun Yu, Y. S. Kwon, and Y. Chung. Determination of electronic band structures of  $CaMnO_3$  and  $LaMnO_3$  using optical-conductivity analyses. *Phys. Rev. B*, 55(23):15489–15493, 1997. URL: <http://link.aps.org/doi/10.1103/PhysRevB.55.15489>, doi:10.1103/PhysRevB.55.15489.
- [20] J. H. Jung, K. H. Kim, T. W. Noh, E. J. Choi, and Jaejun Yu. Midgap states of  $La_{1-x}Ca_xMnO_3$ : Doping-dependent optical-conductivity studies. *Physical Review B*, 57(18):11043–11046, 1998.

- [21] Arisato Kawabata. Theory of Raman Scattering by Magnetic Excitations in Ferromagnetic Transition Metals. *Journal of the Physical Society of Japan*, 29(4):890–901, 1970. URL: <http://journals.jps.jp/doi/10.1143/JPSJ.29.890>, doi:10.1143/JPSJ.29.890.
- [22] Arisato Kawabata. Green Function Theory of Raman Scattering. *Journal of the Physical Society of Japan*, 30(1):68–85, jan 1971. URL: <http://journals.jps.jp/doi/10.1143/JPSJ.30.68>, doi:10.1143/JPSJ.30.68.
- [23] Bernhard Keimer. Raman Scattering. URL: [https://www.fkf.mpg.de/5471793/07\\_Raman-Scattering.pdf](https://www.fkf.mpg.de/5471793/07_Raman-Scattering.pdf).
- [24] Daniel I. Khomskii. *Transition Metal Compounds*. Cambridge University Press, Cambridge, 2014.
- [25] Charles Kittel. *Einführung in die Festkörperphysik*. Oldenbourg Verlag, 13. edition, 2002.
- [26] N. N. Kovaleva, A. V. Boris, C. Bernhard, A. Kulakov, A. Pimenov, A. M. Balbashov, G. Khaliullin, and B. Keimer. Spin-Controlled Mott-Hubbard Bands in LaMnO<sub>3</sub> Probed by Optical Ellipsometry. *Physical Review Letters*, 93(14):147204–1–147204–4, 2004. doi:10.1103/PhysRevLett.93.147204.
- [27] L. L. Krushinskii and P. P. Shorygin. The Theory of Line Intensities in the Spectrum of Scattered Light. I. The Quantum Model (Condon Approximation). *Optics and Spectroscopy*, 11:12, 80, 1961.
- [28] K. I. Kugel and Daniel I. Khomskii. Superexchange Ordering of Degenerate Orbitals and Magnetic Structure of Dielectrics with Jahn-Teller Ions. *Jetp Letters-JETP LETT-ENGL TR*, 15, 1972.
- [29] K. I. Kugel and D. I. Khomskii. Crystal structure and magnetic properties of substances with orbital degeneracy. *Sov. Phys. - JETP*, 37(4):725, 1973.
- [30] H. Kuzmany. *Festkörperspektroskopie*. Springer Verlag, Berlin, 1990.
- [31] M. Fox. *Optical properties of solids. Oxford master series in condensed matter physics*. Oxford University Press, 2001.
- [32] T. E. Furtak and M. V. Klein. *Optik*. Springer Verlag, Berlin, 1988.
- [33] Neil Mathur and Peter Littlewood. Mesoscopic Texture in Manganites. *Physics Today*, 56(1):25–30, jan 2003. URL: <http://physicstoday.scitation.org/doi/10.1063/1.1554133>, doi:10.1063/1.1554133.

- [34] A. J. Millis. Cooperative Jahn-Teller effect and electron-phonon coupling in  $\text{La}_{1-x}\text{A}_x\text{MnO}_3$ . *Physical Review B*, 53(13):8434–8441, 1996. URL: <https://link.aps.org/doi/10.1103/PhysRevB.53.8434>, doi: [10.1103/PhysRevB.53.8434](https://doi.org/10.1103/PhysRevB.53.8434).
- [35] A. J. Millis. Lattice effects in magnetoresistive manganese perovskites. *Nature*, 392(March):147–150, 1998.
- [36] A. J. Millis, Boris I. Shraiman, R. Mueller, T. Bell Laboratories, Mountain Avenue, and Murray Hill. Dynamic Jahn-Teller Effect and Colossal Magnetoresistance in  $\text{La}_{1-x}\text{Sr}_x\text{MnO}_3$ . *Physical Review Letters*, 77:175–178, 1996.
- [37] A. J. Millis, P. B. Littlewood, and B. I. Shraiman. Double Exchange Alone Does Not Explain the Resistivity of  $\text{La}_{1-x}\text{Sr}_x\text{MnO}_3$ . *Physical Review Letters*, 74(25):5144–5147, 1995.
- [38] N. F. Mott. The Basis of the Electron Theory of Metals, with Special Reference to the Transition Metals. *Proc. Phys. Soc. London*, A(62):416–422, 1949.
- [39] N. F. Mott. ON THE TRANSITION TO METALLIC CONDUCTION IN SEMICONDUCTORS. *Can. J. Phys.*, 34(12A):1356–1368, 1956.
- [40] N. F. Mott. The transition to the metallic state. *Philos Mag*, 6:287–309, 1961.
- [41] Y. Murakami, J. P. Hill, D. Gibbs, M. Blume, I. Koyama, M. Tanaka, H. Kawata, T. Arima, Y. Tokura, K. Hirota, and Y. Endoh. Resonant X-Ray Scattering from Orbital Ordering in  $\text{LaMnO}_3$ . *Physical Review Letters*, 81:582, 1998.
- [42] Stefan Naler. *Optical Studies of Ordering Phenomena in Manganese Oxides*. PhD thesis, University of Hamburg, Göttingen, 2005.
- [43] Matthias Opel. Magnetism, 2004. URL: <https://www.wmi.badw.de/teaching/Lecturenotes/magnetismus/Kapitel-6.pdf>.
- [44] J. Orenstein and A. J. Millis. Advances in the Physics of High-Temperature Superconductivity. *Science*, 288(April):468–475, 2000.
- [45] Sönke Ostertun. *Electronic and Phononic Excitations in  $\text{R}\text{Ba}_2\text{Cu}_3\text{O}_7$  ( $R=Y, Y_{1-x}\text{Pr}_x, Y_{1-x}\text{Ca}_x, \text{Yb}, \text{Er}, \text{Sm}, \text{Nd}$ )*. PhD thesis, University of Hamburg, Aachen, 2001.
- [46] Eva Pavarini and Erik Koch. Origin of Jahn-Teller Distortion and Orbital Order in  $\text{LaMnO}_3$ . *Physical Review Letters*,

- 086402(FEBRUARY):104–107, 2010. doi:[10.1103/PhysRevLett.104.086402](https://doi.org/10.1103/PhysRevLett.104.086402).
- [47] Vasili Perebeinos and Philip B. Allen. Multiphonon resonant Raman scattering predicted in  $\text{LaMnO}_3$  from the Franck-Condon process via self-trapped excitons. *Physical Review B - Condensed Matter and Materials Physics*, 64(8):1–6, 2001. doi:[10.1103/PhysRevB.64.085118](https://doi.org/10.1103/PhysRevB.64.085118).
- [48] J. B. Renucci, R. N. Tyte, and M. Cardona. Resonant Raman scattering in silicon. *Physical Review B*, 11(10):3885–3895, 1975. URL: <https://link.aps.org/doi/10.1103/PhysRevB.11.3885>, doi:[10.1103/PhysRevB.11.3885](https://doi.org/10.1103/PhysRevB.11.3885).
- [49] Pablo Rivero, Vincent Meunier, and William Shelton. Electronic, structural, and magnetic properties of  $\text{LaMnO}_3$  phase transition at high temperature. *Physical Review B*, 024111:1–10, 2016. doi:[10.1103/PhysRevB.93.024111](https://doi.org/10.1103/PhysRevB.93.024111).
- [50] J. Rodriguez-Carvajal, M. Hennion, F. Moussa, A. H. Moudden, L. Pinsard, and A. Revcolevschi. Neutron-diffraction study of the Jahn-Teller transition in stoichiometric  $\text{LaMnO}_3$ . *Phys. Rev. B*, 57(6):R3189–R3192, 1998.
- [51] Michael A. Rübhausen. *Electronic Correlations in Cuprate Superconductors*. PhD thesis, Institute for Applied Physics, University of Hamburg, Germany, Aachen, 1998.
- [52] E. Saitoh, S. Okamoto, K. T. Takahashi, K. Tobe, K. Yamamoto, T. Kimura, S. Ishihara, S. Maekawa, and Y. Tokura. Observation of orbital waves as elementary excitations in a solid. *letters to nature*, 410(March):180–183, 2001.
- [53] Majdi Salman. *Mott-Hubbard Optical Bands in  $\text{LaMnO}_3$  Investigated by Spectral Ellipsometry*. PhD thesis, Cardiff University, 2009.
- [54] P. Schiffer, A. P. Ramirez, W. Bao, and S.-W. Cheong. Low temperature magnetoresistance and the magnetic phase diagram of  $\text{La}_{1-x}\text{Ca}_x\text{MnO}_3$ . *Physical Review Letters*, 75(18):3336–3339, 1995. doi:[10.1103/PhysRevLett.75.3336](https://doi.org/10.1103/PhysRevLett.75.3336).
- [55] B. Schulz, J. Bäckström, D. Budelmann, R. Maeser, M. Rübhausen, M. V. Klein, E. Schoeffel, A. Mihill, and S. Yoon. Fully reflective deep ultraviolet to near infrared spectrometer and entrance optics for resonance Raman spectroscopy. *Review of Scientific Instruments*, 76(7):73107, 2005. doi:[10.1063/1.1946985](https://doi.org/10.1063/1.1946985).

- [56] Benjamin Schulz. *Investigation of bio-organic systems by means of optical techniques*. PhD thesis, Institute of Applied Physics, University of Hamburg, Germany, Cuvillier Verlag Göttingen, 2004.
- [57] Stefan G. Singer. *Electronic Structure and Optical Spectroscopy of Strongly Correlated Manganites and Heusler Alloys*. PhD thesis, Universität Hamburg, Verlag Dr. Hut, 2009.
- [58] K. Tobe and T. Kimura. Anisotropic optical spectra in a detwinned  $\text{LaMnO}_3$  crystal. *Phys. Rev. B*, 64:184421–1–184421–5, 2001. doi:10.1103/PhysRevB.64.184421.
- [59] A. Trokiner, S. Verkhovskii, A. Gerashenko, Z. Volkova, O. Anikeenok, K. Mikhalev, M. Eremin, and L. Pinsard-Gaudart. Melting of the orbital order in  $\text{LaMnO}_3$  probed by NMR. *Physical Review B*, 87:125142, 2013.
- [60] A. Urushibara, Y. Moritomo, T. Arima, A. Asamitsu, G. Kido, and Y. Tokura. Insulator-metal transition and giant magnetoresistance in  $\text{La}_{1-x}\text{Sr}_x\text{MnO}_3$ . *Physical Review B*, 51(20):14103–14109, 1995. doi:10.1103/PhysRevB.51.14103.
- [61] Jeroen Van Den Brink. Orbital-only models: Ordering and excitations. *New Journal of Physics*, 6:1–16, 2004.
- [62] J. H. van Santen and G. H. Jonker. Electrical conductivity of ferromagnetic compounds of manganese with perovskite structure. *Physica*, 16(7-8):599–600, 1950.
- [63] S. Wall, D. Prabhakaran, A. T. Boothroyd, and A. Cavalleri. Ultrafast Coupling between Light, Coherent Lattice Vibrations, and the Magnetic Structure of Semicovalent  $\text{LaMnO}_3$ . *Physical Review Letters*, 103:097402–1–097402–4, 2009. doi:10.1103/PhysRevLett.103.097402.
- [64] Wikipedia. Ellipsometrie. URL: <https://fr.wikipedia.org/wiki/Ellipsometrie>.
- [65] Shaun Williams. Transition Metals and Coordination Chemistry. URL: <http://shaunmwilliams.com/GenChem/chapter21.html#{#}slide-49>.
- [66] D. L. Rousseau and P. F. Williams. Resonance Raman scattering of light from a diatomic molecule. *The Journal of Chemical Physics*, 64(9):3519–3537, 1976. doi:10.1063/1.432720.

- [67] E. O. Wollan and W. C. Koehler. Neutron diffraction study of the magnetic properties of the series of perovskite-type compounds  $[(1-x)\text{La},x\text{Ca}]\text{MnO}_3$ . *Physical Review*, 100(2):545–563, 1955. doi:[10.1103/PhysRev.100.545](https://doi.org/10.1103/PhysRev.100.545).